

SPECIAL ISSUE



TECHNICAL, SCIENTIFIC
AND
RESEARCH REPORTS

VOL.9 (2017)

Prostate cancer Radiomics
using multiparametric MR imaging

Prostate cancer Radiomics using multiparametric MR imaging

**Andrea Barucci^(1,*), Michela Baccini⁽⁴⁾, Roberto Carpi⁽²⁾, Ambra Giannetti⁽¹⁾,
Maristella Olmastroni⁽²⁾, Roberto Pini⁽¹⁾, Sonia Pujol⁽³⁾,
Fulvio Ratto⁽¹⁾, Giovanna Zatelli⁽²⁾, Marco Esposito⁽²⁾**

⁽¹⁾ "Nello Carrara" Institute of Applied Physics, CNR Florence Research Area, Via Madonna del Piano 10, 50019 Sesto Fiorentino (FI), Italy

⁽²⁾ Azienda USL Toscana Centro, Piazza Santa Maria Nuova 1, Firenze, Italy

⁽³⁾ Surgical Planning Laboratory, Department of Radiology, Brigham and Women's Hospital, Harvard Medical School, Boston, MA, USA

⁽⁴⁾ Department of Statistics, Informatics and Applications "G. Parenti", University of Florence, Florence, Italy

(*) A.Barucci@ifac.cnr.it

Index

1. Introduction
2. An introduction to Radiomics
 - 2.1 Radiomics pipeline
 - 2.1.1 *First step: multiparametric imaging*
 - 2.1.2 *Second step: Volume segmentation and ROIs selection*
 - 2.1.3 *Third step: extraction of Radiomic features*
 - 2.1.4 *Fourth step: statistical analysis and data mining*
- Some details about using Machine learning for building Radiomics classifiers
 - 2.2 Radiogenomics: the convergence of Radiomics and Genomics
3. Prostate Cancer: mpMRI and Radiomics
 - 3.1 *An introduction to the Prostate Cancer*
 - 3.2 *The role of Multiparametric MRI in the theranostic of Prostate cancer*
 - 3.3 *Application of Radiomics to Prostate Cancer: a short review*
4. Our study on the application of Radiomics to Prostate Cancer
 - 4.1 *Database*
 - 4.2 *Multiparametric MRI image acquisition*
 - 4.3 *mpMRI data elaboration*
 - 4.4 *Segmentation*
 - 4.5 *Radiomic features extraction*
5. A critical review on the promise and challenges of Radiomics
 - 5.1 *Repeatability, Reproducibility and Robustness*
 - 5.2 *Sample size and statistical power: Big Data and Radiomics*
 - 5.3 *Standardization and benchmarking*
 - 5.4 *Limitations and pitfalls*
 - 5.5 *Future directions in the Radiomics research field*
- Radiomics in the study of other diseases
6. Conclusions
7. Acknowledgements
 - Appendix 1. First steps in automatic prostate segmentation*
 - Appendix 2. Two examples of ADC and DCE data radiomic analysis*
 - Appendix 3. MpMRI phantoms for repeatability, reproducibility and robustness*
 - Appendix 4. Radiomics applications in ultrasound and photoacoustic imaging*
 - Appendix 5. MpMRI phantoms for the IRINA project*

References

1 - Introduction

The aim of this report is to describe and explore the potential of Radiomics in the framework of the activities developed at the “Nello Carrara” Institute of Applied Physics (IFAC), which is part of the National Research Council (CNR), in collaboration with USL Toscana Centro.

The possibility of a more quantitative study of imaging data emerged during the work of specialization thesis in medical physics of one of the authors [1, 2]. The thesis subsequently led to the IRINA project (“Imaging molecolare di risonanza magnetica della biodistribuzione di nanoparticelle e vettori cellulari per applicazioni teranostiche” – Biodistribution of nanoparticles and cellular vehicles using biomolecular magnetic resonance imaging for theranostics applications) [2, Appendix 5] on the use of nanoparticles as a new theranostics agents in the context of multiparametric magnetic resonance imaging (MRI).

During the thesis work, we developed novel quantitative imaging methodologies [131], with a focus on clinical applications of MRI spectroscopy [1]. In the IRINA project we have extended the MRI techniques involved, studying different diffusion models, new algorithms for spectroscopy data analysis, techniques for data and image analysis, applications of these techniques to database of patients beginning to face the problem of Big Data in medicine, coming at the end to the concept of Radiomics.

Radiomics can be described as a process designed to extract a large number of quantitative features from digital images, place these data in shared databases, and subsequently mine the data for hypothesis generation, testing, or both. Radiomics is designed to develop decision support tools, therefore requiring the combination of radiomic data with other patient characteristics in order to increase the power of the decision support models [80].

All the activities have been divided between basic, clinical research, and clinical practice, and focused on quantitative MRI data using a translational approach.

This report provides a general introduction to Radiomics, introduces an example application on multiparametric Magnetic Resonance Imaging (mpMRI) for Prostate Cancer (PCa), and presents the workflow that we implemented in our projects.

In this report we describe Radiomics, reviewing its applications in general, but focusing on the case of Prostate Cancer (PCa) studied with the multiparametric Magnetic Resonance Imaging (mpMRI). Then we will describe the implementation of the radiomic workflow in the framework of our projects.

Prostate cancer was selected as a target of our study, following our first work on quantitative imaging [1, 2], but especially thanks to the collaboration with the Diagnostic Department of Santa Maria Nuova Hospital, which is a regional reference center for this disease [128, 129, 130].

In our study we have two objectives related to precision medicine: first the implementation of the radiomic workflow in clinical practice as a reproducible and robust clinical tool, and second, a study of the correlation of Radiomics with clinical and genomics data.

The discipline connecting tumor morphology described by Radiomics and its genome described by genomic data is called “Radiogenomics”, and it has the potential to derive the “radio phenotypes” that both correlate to and complement existing validated genomic risk stratification biomarkers [17, 18, 66, 80].

A robust clinical implementation of Radiogenomics could allow an effective personalization of the therapy (precision medicine) thanks to a better patient’s stratification.

2 - An introduction to Radiomics

Molecular characterization using genomics, proteomics, and metabolomics information has been the main focus of personalized therapy. However, spatial and temporal intra-tumoral heterogeneity that arises from regional variations in metabolism, vasculature, oxygenation, and gene expression is a common feature of malignant tumors [47].

Currently it is known that solid tumors are not homogeneous entity, but rather are composed of multiple clonal sub-populations of cancer cells, exhibiting considerable spatial and temporal variability that could potentially yield valuable information about tumor aggressiveness.

Needle biopsy is the preferred approach for molecular characterization of tumor tissue. However, the procedure is invasive and fails to accurately represent the range of potential biological variations within a tumor.

MRI data acquisitions enable non-invasive sample of the whole tumor, and tumor characteristics at the cellular and genetic levels could be reflected in the phenotypic patterns obtained with medical images.

However, despite the promise of medical imaging to assess tumor heterogeneity, imaging features are often assessed visually and described qualitatively by radiologists or nuclear medicine physicians, giving rise to a subjective descriptions of tumor imaging phenotypes. These visual assessments show a large intra and inter-observer variability [47]. Therefore, there is a need for an objective and reproducible quantifications of various imaging features.

Radiomics tries to solve this issue, using advanced quantitative features to objectively and quantitatively describe tumor phenotypes. These features can be extracted from medical images using advanced mathematical algorithms to discover tumor characteristics that may not be appreciated by the naked eye.

Radiomics features can provide richer information about intensity, shape, size or volume, and texture of tumor phenotype that is distinct or complementary to that provided by clinical reports, laboratory test results, and genomic or proteomic assays.

Radiomics may thus provide great potential to capture important phenotypic information, such as intra-tumor heterogeneity, subsequently providing valuable information for personalized therapy. More details can be found in References [18, 20, 31, 47, 67].

While the concept of extracting quantitative features from medical imaging data is not new, this task is not trivial, and the radiomic workflow is currently under investigation and development by many research groups. This renewed interest is mainly driven by the increased digitalization in the hospital, with an easier access to large amounts of informations through the hospital picture archiving and communication systems (PACs) combined with the increased computational and communicational power.

From an historical point of view, Radiomics, combining quantitative analysis of radiological images and machine learning methods has its root in CAD, and can be considered as a new application of established techniques (in particular from the field of computer vision) [20]. However some aspects of Radiomics are new, for example the number of image features involved, which in CAD are usually 8–20, whereas in Radiomics it is increased to a few hundred or thousands. Furthermore the domain of investigation of Radiomics consists of association of features extracted from large-scale radiological image analysis with biological or clinical endpoints, resulting in both prognostic and predictive models.

Different imaging modalities (e.g., MRI, CT, PET, ultrasound) can be used as the basis for extracting radiomic features. The complete set of imaging features obtained for a patient using the available images is called the “radiome”. A collection of features which holds prognostic and/or predictive value is often called “radiomic signature”. The fundamental hypothesis of Radiomics is that quantitative analysis of tumor through a large amount of radiomic features can provide valuable diagnostic, prognostic or predictive information. For tumors, heterogeneity assessed through imaging could be the expression of genomic heterogeneity, which would indicate worse prognosis, as tumors with more genomic heterogeneity are more likely to develop a resistance to treatment and to metastasize.

The aim of Radiomics is to explore and exploit these sources of information to develop diagnostic, predictive, or prognostic radiomic model to support personalized clinical decisions and improve individualized treatment selection.

Radiomics models have been built with power to predict tumor characteristics as histology, genetic footprint, as well as response to therapy in terms of pathological response from primary tumor and lymph nodes, response to chemotherapy or chemo-radiotherapy, recurrence, occurrence of lymph nodes or distant metastases and survival, for a variety of pathologies. A good review of all these results can be found in [20, 80].

Radiomic tools can help in daily clinical work, and radiologists can play a pivotal role in continuously building the databases that are to be used for future decision support.

The term “Radiomics” derives from the combination of word “radiology” and the suffix “omics”. It is a new extension of omics methods applied to quantitative radiology.

The suffix -omics is a term that originated in molecular biology disciplines to describe the detailed characterization of biologic molecules such as DNA (genomics), RNA (transcriptomics), proteins (proteomics), and metabolites (metabolomics). One desirable characteristic of -omics data is that these data are mineable and, as such, can be used for exploration and hypothesis generation. The -omics concept readily applies to quantitative tomographic imaging.

2.1 Radiomics pipeline

The process of building a radiomic signature of prognostic value can be divided in four stages [18, 80]: the first step involves images acquisition, followed by automated or manual segmentation of ROI. Then image

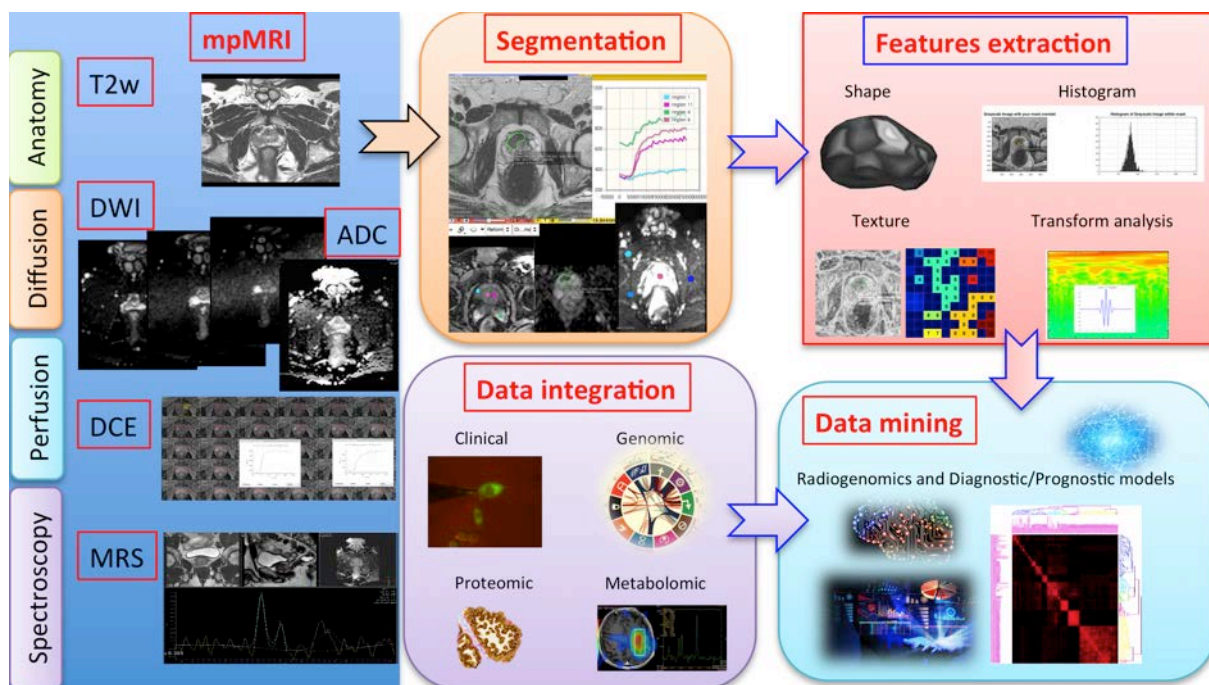


Fig. 1 - Scheme of radiomics process for prostate mpMRI. First step - mpMRI acquisition: a typical mpMRI exam of the prostate consists of: T2weighted (T2w); diffusion weighted imaging (DWI) and the calculated apparent diffusion coefficient (ADC) maps; dynamic contrast enhanced (DCE). Second step: Features extraction: identification of volumes of interest and segmentation. Third step: quantitative imaging radiomic features are extracted related to volume/shape, intensity volume histogram (first order features); texture features (second order features) and transform analysis features; Last step: radiomic data is integrated with clinical, genomic, proteomic and metabolomic data. The integrated dataset is mined to develop diagnostic, predictive, or prognostic models.

features are extracted, and radiomic data is integrated with clinical, genomic, proteomic and metabolomic data. Finally, the integrated dataset is mined to develop diagnostic, predictive, or prognostic models. These steps, in the case of the radiomic process for analysis of prostate mpMRI, are shown in Fig. 1 as reported in Ref. [18].

2.1.1 First step: multiparametric imaging

The first step in the radiomic workflow is the acquisition of a dataset of images from the target organ. In the field of oncology, the most widely used modalities include ultrasound, CT, positron emission tomography (PET) and MRI. These medical images are regularly acquired for standard clinical diagnostics, (radiotherapy) treatment planning and follow-up purposes, and represents a source of informations for radiomic analyses. Many radiomics studies are relying on retrospective data sets, in which individual image acquisition parameters can be different. These different settings can have an influence on the quality and reliability of the extracted radiomic features, as will be discussed below in detail [22].

2.1.2 Second step: Volume segmentation and ROIs selection

This step involves the segmentation of the organ volume, eventually defining some regions of interest (ROIs). Segmentation is among the most critical and challenging components of the radiomic workflow [80]. It is critical because the subsequent feature data are generated from the segmented volumes. It is challenging because many tumors lack clear margins. In addition, there is a lack of consensus on the definition of ground truth and the reliability of manual and automatic segmentation. However, a current trend is that computer-aided edge detection followed by manual supervision provide optimal outcomes. Still, it is well recognized that inter-operator variability of manually contoured tumors is high.

As a matter of fact tumor delineation remain challenging both for automatic or manual methods because tumors may have indistinct borders [66, 80].

The dimension of ROIs must be careful evaluated because many features could not have sense when tumors are too small [53, 92]. There are no consistent guidelines on the smallest ROI that can be assessed,

although some authors have suggested 5 cc as a suitable cutoff. Obviously the cutoff value depends on the imaging modality and may also vary depending on the site or tumor under investigation. Smaller ROIs can either give meaningless Radiomics features values because there are not enough pixels for a true evaluation or the smaller the ROI, the more related the results may be to tumor volume [53].

The segmentation can be of the entire tumor volume or only of some sub-regions of interest. Some researchers for example have segmented the axial slice where the tumor is largest [53]. Segmenting a single slice or fixed-size ROI significantly improves efficiency when manual segmentation is used. However, the extracted ROI may not represent the entire tumor. The effect of segmenting a single slice or fixed-size ROI on the extracted Radiomics image features varies widely, depending on the image feature, but can be significant [53, 92].

2.1.3 Third step: extraction of Radiomic features

A “feature” is a descriptor of an image such as image intensity, texture, shape, etc. [20, 66, 67, 80, 92]. These features can be extracted from the entire segmented volume and/or from some ROIs (e.g. of tumor or normal tissue regions). There are different categories of Radiomics features, generally divided in 4 subcategories as reported in Table 1 [18]. The first category (C1) summarizes features descriptive of the volume size, shape, etc.; the second (C2), third (C3) and fourth (C4) category can be described as first-, second- and higher order statistical outputs. First-order statistic features are related to the intensity histogram of a given volume: mean, median, standard deviation, minimum, maximum, quartiles, kurtosis, skewness, etc. The second-order statistics are related to texture analysis features, also known as Haralick texture descriptors. On the grey level co-occurrence matrix (GLCM), various statistics can be computed: energy, entropy, correlation, homogeneity, contrast, etc. GLCM captures the frequency of co-occurrence of similar intensity levels over the region, which describes the texture of the region of interest. Another technique in this category is fractal-based texture analysis, which examines the difference between pixels at different length scales (offset differences). And lastly, the higher-order methods extract repetitive or non-repetitive patterns using kernel functional transformation. Some popularly used texture descriptors are Wavelets, Laplace, Fourier transforms, Gabor filters, Minkowski functionals, etc. More details about the different kind of Radiomics features can be found in [20, 22, 31 – 44, 66, 67, 73, 79, 80, 85 – 89, 92].

There are many software commercially available to evaluate Radiomics Features from medical imaging and in particular from mpMRI images and maps. A good review can be found in Ref. [53].

As numerous radiomic features can be extracted from medical images, it is very important to identify only a subset of independent features (Fig. 2) and can be relevant to the underlying tumor biology and genetics.

Considering the very large dimensionality of the feature space, especially when dealing with multimodal imaging, advanced algorithms that rank features by their importance for a given disease outcome are often essential to reduce over fitting, increase reliability, and address the curse of dimensionality [66, 71, 80, 90]. The latter, which refers to a crucial aspect in radiogenomic data analysis, can be roughly summarized as the requirement of higher sample sizes as the number of the features increase [66].

Tab. 1 - Broad radiomics feature categories for mpMRI of the prostate [18].

| Category | Name | Description | Image Modality | Volumes |
|-----------|--|--|----------------|------------------------|
| C1 | Region size/shape/location | Volume descriptors/roundness/circularity descriptors | T2w | Prostate, PZ, TZ, ROIs |
| C2 | Histogram of volume intensity | Mean, median, standard deviation, kurtosis, skewness, quartiles, min, max | T2w, DWI, DCE | ROIs, NAT-PZ, NAT-TZ |
| C3 | Texture analysis: gray level co-occurrence matrix and fractal analysis | Contrast, energy, entropy, correlation, inertia, cluster prominence, cluster shade, etc. | T2w, DWI | ROIs, NAT-PZ, NAT-TZ |
| C4 | Transform analysis | Wavelets, Gabor, Kirsch, Fourier | T2w, DWI | ROIs, NAT-PZ, NAT-TZ |

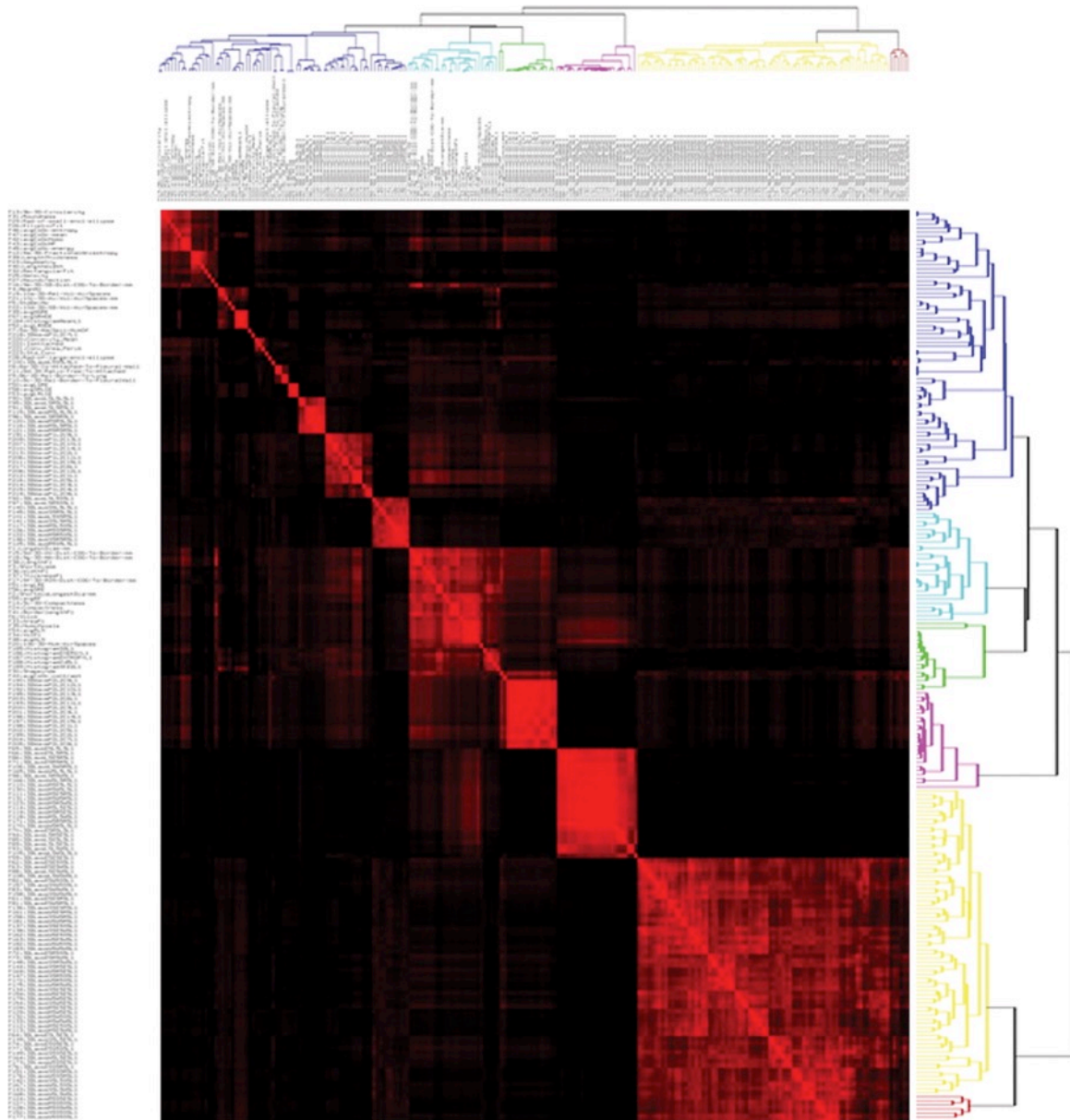


Fig. 2 - Covariance matrix of radiomic features. A total of 219 features were extracted from each non-small cell lung cancer tumor in 235 patients. Across all tumors, each feature was individually compared with all other features by using regression analysis, thereby generating correlation coefficients (R-square). Individual features were then clustered and plotted along both axes, and R-square is shown as a heat map, with areas of high correlation (R-square 0.95) shown in red. Thus, each of the red squares along the diagonal contains a group of features that are highly correlated with one another and are thus redundant. For data analysis, one feature was chosen to be representative of each of these groups. The representative feature chosen was the one that had the highest natural biologic range (interpatient variability) across the entire patient data set, with the explicit assumption that features that show the highest interpatient variability will be the most informative. (Image courtesy of Y. Balagurunathan, Ref. [71])

However, how the tumor patho-physiological processes give rise to imaging phenotypes that can be quantified by radiomic features remain unclear. Future studies would need to investigate these associations to further elucidate the biological meaning of the radiomic features [47, 66 – 75, 80].

2.1.4 Fourth step: statistical analysis and data mining

Radiomics analyses epitomize the pursuit of precision medicine, in which molecular and other biomarkers are used to predict the right treatment for the right patient at the right time. The availability of robust and validated biomarkers is essential to move precision medicine forward. This is exactly the meaning of

the last step in the radiomic workflow, mining the data looking for statistical correlation.

Radiomic features can then be used for different analyses [51 - 53, 67, 76 - 78, 80, 92, 155], the most common being to incorporate them into models to improve patient risk stratification (overall survival, freedom from metastasis, etc.). Descriptive and predictive models can be built relating image features to outcome, as well as gene-protein signatures. Resultant models may include imaging, molecular, and clinical data, and provide valuable diagnostic, prognostic or predictive information.

However there is need of a deeper understanding if radiomic features add value to clinical data, that is if image features are linked to tumor histology, tumor grade, and/or gene signatures.

An interesting correlation to be investigated would be with the texture descriptors incorporated in the modern complex diagnostic imaging reporting and data systems [80, 106], such as the Breast Imaging Reporting and Data System (BI-RADS) [83], the Prostate Imaging Reporting and Data System (PI-RADS) (Fig. 3) [81, 82], and the Lung Imaging Reporting and Data System (Lung-RADS) [84].

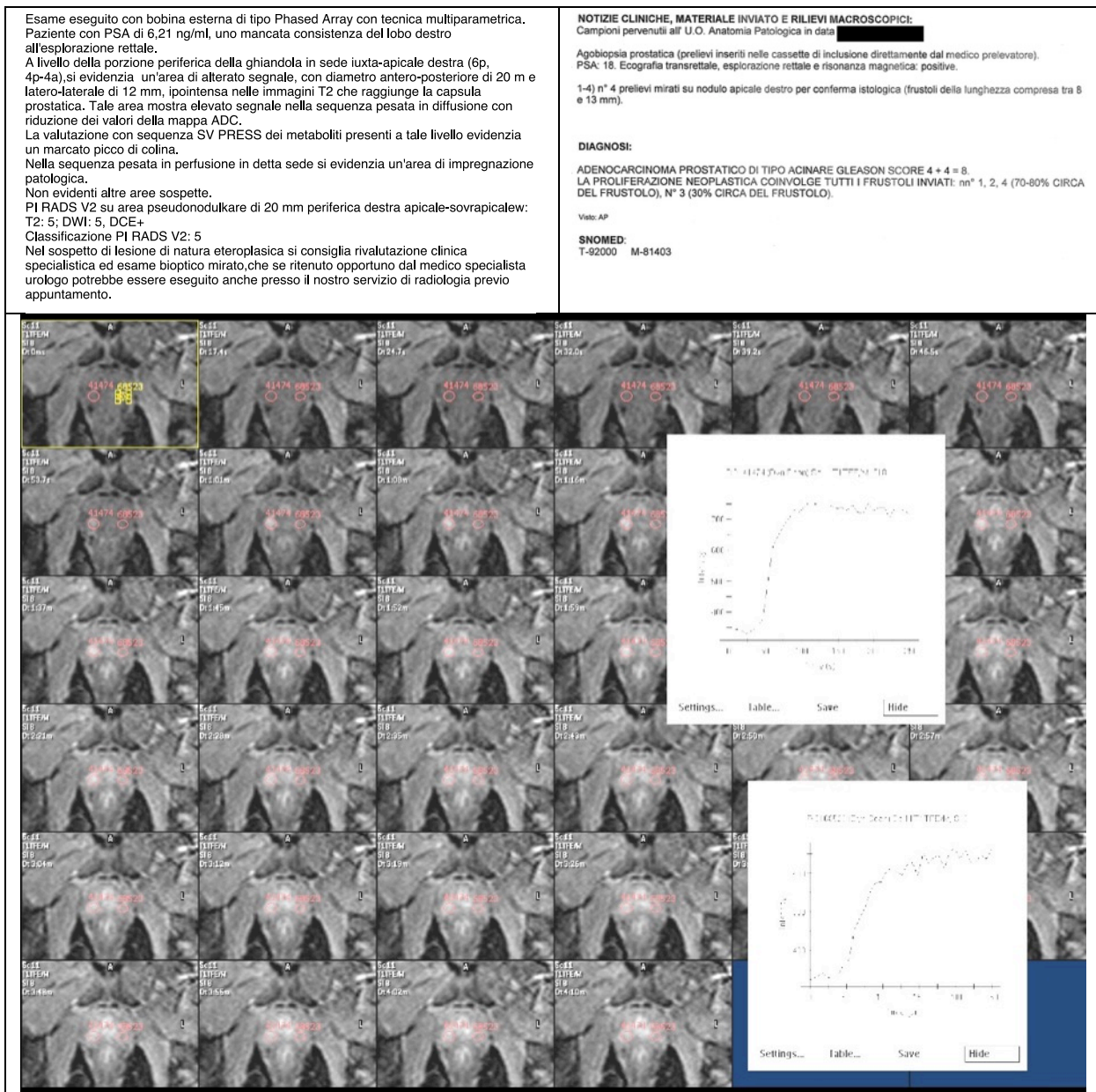


Fig. 3 - Example of prostate examination report with mpMRI using PI-RADS (left) and biopsy report (right), both in Italian language. Images on the bottom panel shows DCE images series from the same patient and results from 2 ROIs in the tumor region and in the symmetrical in healthy tissue.

Model development is then a very important component of the radiomic workflow and has many potential pitfalls [54, 80]. A partial list of software packages available for modeling/statistical analysis can be found in [53].

Some details about using Machine learning for building Radiomics classifiers

The goal of Radiomics is to develop a function or mathematical model to classify patients according to their predicted outcome by means of radiomic features. In the language of pattern recognition machine-learning, this task is equivalent to building a “classifier”, which is an algorithm analyzing training data and inferring a hypothesis (the function), to predict the labels of unseen observations, e.g. patient outcome or tumor phenotype [147].

Despite a large number of features can be extracted from each patient images, typically in the range of a few hundred to thousands, not all of the features would be useful for a classifier to distinguish between patients of different classification, because some of them might be highly correlated with each other or redundant and some of them may not be strongly associated with the given classification task. By feature selection we intend an algorithm used to select “effective” features for a given task, i.e. those features who are relevant to explain a given output as a function of a group of features [52, 67, 76 – 78, 80].

2.2 Radiogenomics: the convergence of Radiomics and Genomics

The integration of Radiomics with genomic signatures is commonly known as Radiogenomics. The underlying hypothesis is that radiomic features can be used to derive “radiophenotypes” that both correlate to and complement existing validated clinical and genomic risk stratification biomarkers.

Many studies have shown that this correlation can be found [31, 47, 66, 79, 80], for example in CT imaging has been found that radiomic features related to shape and wavelet features describing the heterogeneous phenotype of lung tumors [148] can be associated with cell cycle pathway, suggesting that highly proliferative tumors demonstrate complex imaging patterns [79]. Moreover, various biological mechanisms may be described by different radiomic features as the features were found to be related with different biological gene sets, including DNA recombination and regulation of DNA metabolic processes [31, 66].

The general workflow for a radiogenomic study is shown in Fig. 4.

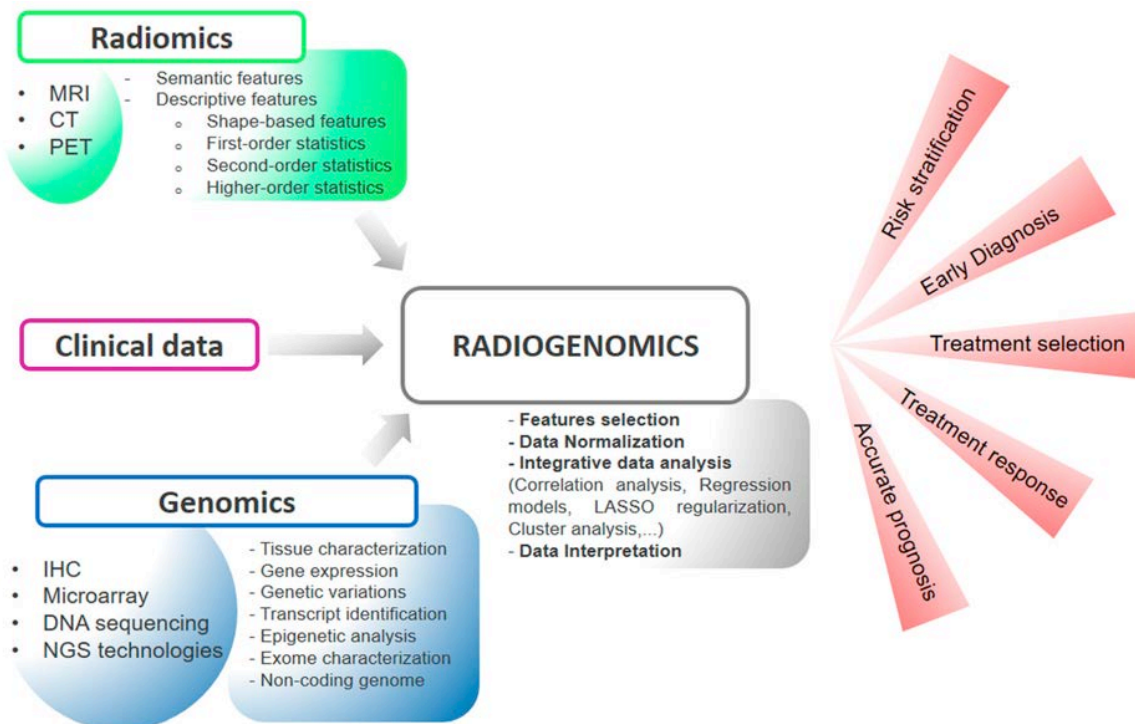


Fig. 4 - The figure shows a general workflow for radiogenomic study. The first step includes data acquisition (clinical information, imaging and genomic data). Subsequently, data are normalized and underwent an integrative analysis to characterize each radiomic feature and identify specific underlying molecular functions. The overall flow, here schematically depicted, could represent a novel integrated approach for cancer diagnosis and prognosis. Reprinted from [66].

Radiogenomics studies must combine a large number of quantitative imaging features with a massive genomic signature using computer algorithms. In addition, both Radiomics and genomics are needful for the clinical decision making and neither one can replace the other, but their potential can be increased through the interpretation of the two methods to improve the management of cancer patients. Furthermore, the study of mutual relationships between imaging and genomics can provide novel insights for the understanding of neoplastic transformation [31, 46, 66, 72, 80, 87].

Indeed a subset of the radiomic data can be used to suggest gene expression or mutation status that potentially warrants further testing. This is important because the radiomic data are derived from the entire tumor rather than from just a sample. Thus, Radiomics can provide important information regarding the sample genomics and can be used for cross-validation. Moreover, a subset of radiomic features is not significantly related to gene expression or mutational data and, hence, has the potential to provide additional, independent information. The combination of this subset of radiomic features with genomic data may increase diagnostic, prognostic, and predictive power.

3 - Prostate Cancer: mpMRI and Radiomics

3.1. *An introduction to the Prostate Cancer*

Prostate cancer exhibits intra-tumoral heterogeneity, which usually is a confounding factor contributing to the underperformance of the current diagnostics and therapeutics approaches. These limitations show the importance to develop better computational tools to stratify patients, e.g. identifying men with low risk of prostate cancer versus others that may be at risk for developing metastatic cancer. A better patients stratification will directly translate to improvements in the patients therapies.

Treatment recommendations for prostate cancer patients are currently based on risk stratification using PSA, Gleason score (GS) and T-category [17], however the overtreatment of men with prostate cancer is a well-recognized problem and active surveillance has rapidly become a standard recommendation for many men with low risk disease [17].

Stratification risk and management based on genomics analysis and gene expression signatures [17, 66], such as Decipher (GenomeDx, San Diego, California), Prolaris Cell Cycle Progression (CCP) (Myriad Genetics, Salt Lake City, Utah), Genomic Prostate Score (GPS) (Genomic Health, Redwood City, CA) have great potential. Prostate cancer, however, exhibits spatial heterogeneity that can confound current pretreatment clinical-pathological and genomic assessment [137].

A promising solution for patients stratification is then mining Radiomics, Genomics and all the clinical data available thanks to statistical prognostic model based on database continuously updated.

3.2. *The role of Multiparametric MRI in the theranostic of Prostate cancer*

In this context multiparametric MRI provides the ideal platform to investigate tumor heterogeneity by mapping the individual tumor habitats [1, 2, 17].

By combining anatomical and metabolic information, mpMRI is becoming the preferred imaging modality in terms of sensitivity and specificity for the diagnostic and treatment of prostate cancer [1, 2, 17, 48, 49, 50, 66].

mpMRI enables the acquisition of clinically relevant information that include perfusion with dynamic contrast enhanced MRI (DCE-MRI), diffusion with diffusion weighted imaging (DWI), anatomy with T2-weighted [T2w] MRI and molecular fingerprint of metabolic processes with magnetic resonance spectroscopy (MRS).

DCE characterizes the concentration of an injected contrast agent over time, enabling the visual differentiation of lesions from normal tissue owing to the increased vascularity and capillary permeability. By exploiting enhancement kinetics, the time course of the signal intensity within the lesion can be used in the interpretation of lesions to determine the likelihood of malignancy.

DCE then allows the evaluation of the enhancement pattern of tumor, which is considered to be related to tumor angiogenesis.

Prostate cancer shows early and more pronounced enhancement than surrounding normal prostate tissue on DCE. Furthermore, DCE can also help to monitor treatment effects as well as cancer detection, because tumors are evidently associated with neo-angiogenesis that induces an increase in the blood volume and transvascular permeability. Tracing the dynamic flow of the contrast agent with DCE, PCa shows strong and rapid contrast enhancement. However, DCE is non-specific, because angiogenesis can also be seen in prostatitis in the peripheral zone and in highly vascularized BPH nodules in the transition zone.

T2w is used for PCa detection, localization and staging, providing the best depiction of the prostatic zonal anatomy and capsule [48]. However there are various conditions (e.g. prostatitis, hemorrhage, atrophy and

post-treatment changes) that can mimic cancer on this kind of images. So T2w is sensitive, but not specific for PCa detection, and must be correlated with the other functional techniques as said previously.

DWI is a powerful functional technique, enabling qualitative and quantitative assessment of PCa aggressiveness thanks to the possibility to calculate maps of Apparent Diffusion Coefficient (ADC) of water molecules and other parameters (e.g. Kurtosis) strictly connected to the cellular and subcellular structure and packaging.

Diffusion maps, characterizing changes in the cellular architecture of the tissue based on local differences in movement of water protons, has been hypothesized to indicate cell death after therapy. PCa shows higher signal intensity on DWI, and a lower ADC values when compared with normal prostatic tissue. Furthermore a considerable number of studies reported the correlation between ADC and Gleason scores, allowing a quantitative assessment of the disease.

Magnetic Resonance Spectroscopy provides informations about some specific metabolites within the prostatic tissue. The levels of citrate, choline and creatine can be evaluated and compared with benign tissue, however spatial resolution is usually poor in respect to the other functional techniques.

However the automated analysis and interpretation of mpMRI is quite challenging, as each exam results in thousands of images and in general there is lack of consensus of how to optimally extract the relevant information.

3.3. Application of Radiomics to Prostate Cancer: a short review

The evaluation of Radiomics features from mpMRI is a field rapidly growing, although it has not been investigated as extensively as on CT and PET scans.

In the case of mpMRI of PCa DWI and DCE can provides quantitative maps, which along with the T2w images can be used for radiomic features extraction.

The potential of this application is shown for instance in [17, 28, 29, 49 67], both showing that textural features of prostate MRI may differentiate non-cancerous and cancerous prostate tissues and may correlate with biochemical recurrence and Gleason score. In the case of application of Radiomics analysis to PCa there is a great effort in the community for addressing the clinical issues about detection and segmentation of the suspicious lesion, and about the assessment of the aggressiveness of prostate cancer. The goal of the latter is in particular to identify patients who can be spared biopsies and/or patients at high risk for metastatic disease, while the aim of the former is to diagnose cancerous versus non-cancerous tissue, providing targets for biopsies or radiation boost [49].

For example in study [28] has been shown that using a sample of 147 men with biopsy-proven prostate cancer, Haralick texture analysis has the potential to enable differentiation of cancerous from noncancerous prostate tissue on both T2-weighted MR images and apparent diffusion coefficient maps derived from diffusion-weighted MR images. In the peripheral zone of the prostate, all five features assessed (entropy, inertia, energy, correlation, and homogeneity) differed significantly between benign and cancerous tissue on both types of images; however, in the transition zone, significant differences were found for all five features on ADC maps and for two features (inertia and correlation) on T2-weighted images. In a follow-up study, these features were used to automatically compute Gleason grade and were found to enable discrimination between cancers with a Gleason score of 6 (3+3) and those with a Gleason score of 7 or more with 93% accuracy. Furthermore, these analyses could be used to distinguish between two different forms of Gleason score 7 disease (4+3 vs 3+4) with 92% accuracy [67, 80, 91].

Recently, in Ref. [80, 92] a thorough prospective radiomic analysis of diffusion- and T2-weighted MR imaging examinations in 49 patients with prostate cancer was performed. Agnostic features extracted from T2-weighted images and ADC maps were compared with more traditional ADC cutoff metrics to test the hypothesis that textures could help differentiate between men with a pathologic Gleason score of 6 and those with a pathologic Gleason score of 7 or higher. This is an important cut-off, as men with a pathologic Gleason score of 6 may be candidates for active surveillance. Although this study may have been underpowered, it shows the potential value of quantitative analysis of tumor heterogeneity in assessing tumor aggressiveness and informing major clinical decisions, such as whether to treat the cancer at all. Of note, other investigators have also found entropy determined from ADC maps (Fig. 5) to be significantly associated with the pathologic Gleason score, even after controlling for the median ADC [28, 80, 91].

From studies shown above we can conclude that mpMRI can provides images and/or maps characterizing qualitatively and quantitatively trough Radiomics the tumor habitat.

Radiomics is then perfectly suited to extract and provide an engine for effective sifting through the multiple series of prostate mpMRI images and/or maps, extracting features from the regions of interest.

However understanding the relationship between quantitative mpMRI and gene expression in prostate cancer is a key point. E.g. in [17] has been shown that both tumor and surrounding prostate tissue contribute

significantly to radiogenomic features associated with tumor molecular characteristics related to aggressive behavior.

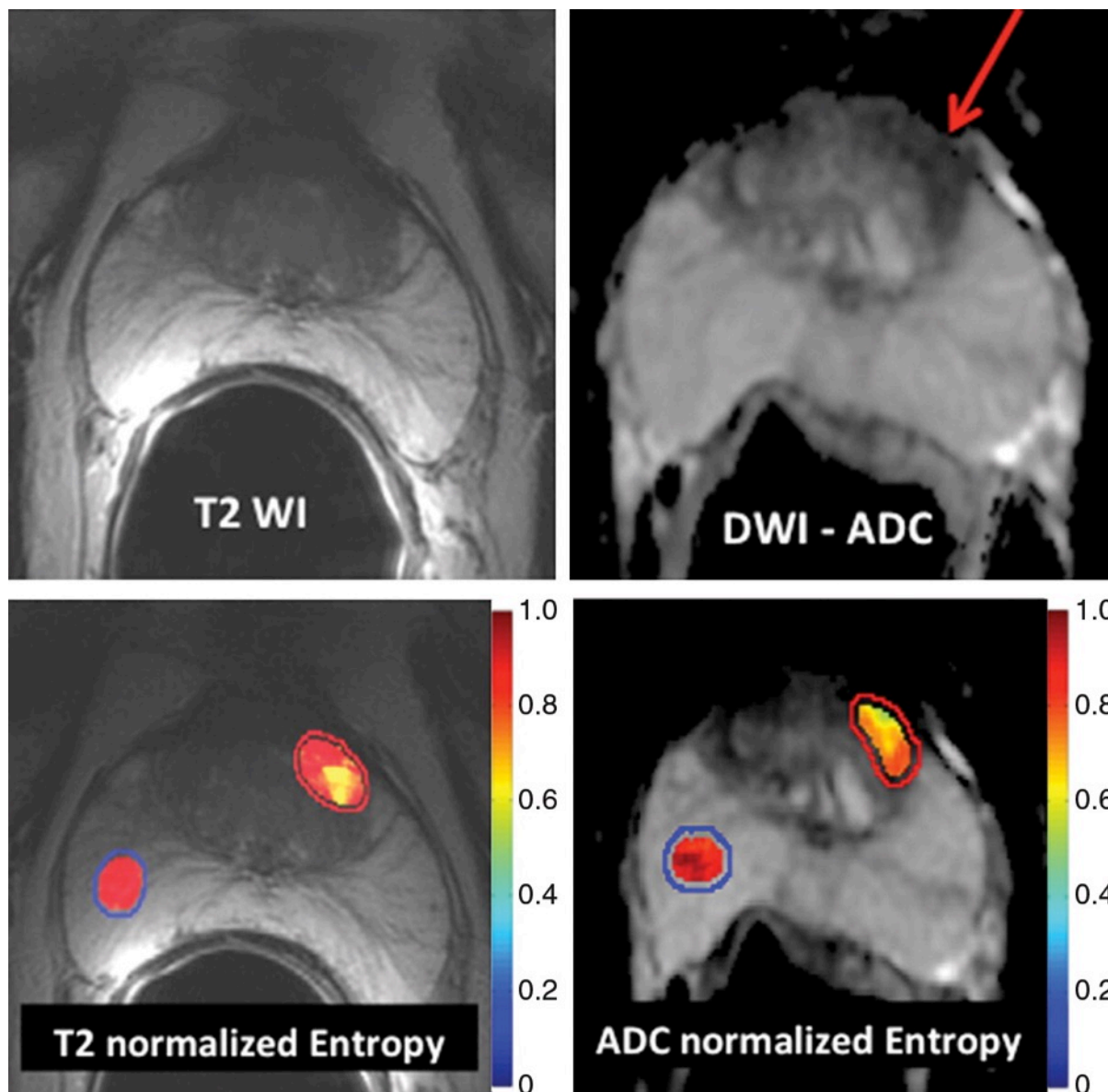


Fig. 5 - Application of texture analysis to T2-weighted MR images and ADC maps of prostate cancer. A lesion in the transition zone is barely discernible on the T2-weighted image (top left) and has higher conspicuity on the ADC map (top right). Texture features were computed on a per-voxel basis (using a $5 \times 5 \times 1$ pixel window) from manually segmented regions of interest identifying the normal peripheral zone (outlined in blue) and cancer (outlined in red). From the computed texture features, a machine learning method was applied to distinguish between normal and cancerous structures and to stratify the Gleason patterns. Heat map images show clear differences between healthy tissue and cancer and depict intra-tumoral heterogeneity that may be useful in assessing tumor aggressiveness and informing fused MR imaging–ultrasonography biopsy. Reprinted with permission from Ref. [80]

4 Our study on the application of Radiomics to Prostate Cancer

The purpose of our study was to show the potential of the radiomic workflow as a diagnostic tool in the context of mpMRI of Prostate Cancer. The workflow described herein has been implemented for research purposes.

4.1 Database

We used an anonymized retrospective database of mpMRI data from clinical patients with or suspected prostate cancer to test the radiomic workflow. Different patients were selected on the basis of tumor characteristics (e.g. single nodule or multifocal nodules) and on the availability of mpMRI and clinical data. For each patient, series of images from the PACs relative to the following kind of examinations were exported to a secondary console for data analysis: T2 weighted imaging (T2w), Diffusion Weighted imaging (DWI), Dynamic contrast Enhancement, Magnetic Resonance Spectroscopy (MRS).

Different kind of patients can then be found in our database: patients with mpMRI visible PCa, patients with suspected PCa due to clinical evaluations (e.g. serum prostate-specific antigen - PSA) but invisible to mpMRI clinical standard examinations, patients coming from screening programs without PCa, patients with data before, during and after different therapies (surgery, radio, chemotherapy, etc.).

All these data have been used with the aim to improve our knowledge about Radiomics algorithms and workflow, testing reproducibility and robustness.

Thanks to the know-how in the developing phantoms for quantitative imaging development protocols in mpMRI, we have had the possibility to use these data to test the Radiomics features in simpler cases [See Appendix 3].

4.2 Multiparametric MRI image acquisition

Most imaging data were acquired on 1.5T MRI scanners (Philips Achieva, Philips Medical Systems, Best, Netherlands). However because the images database were built using data from different hospitals in Tuscany, images may be acquired with different scanners (GE Healthcare, Siemens, etc.) and then different sequences, resolutions, etc. This kind of heterogeneity in acquisition can be a source of problems in the interpretation of the results. It will be analyzed in detail in a specific part of this report. DWI images were usually acquired with 4 or 5 b-values, allowing to evaluate more complex diffusion maps in respect to the mono-exponential model. In Fig. 6a-c examples of images acquired on a patient using mpMRI are shown. Fig. 7 shows the data as displayed and explored using the 3D slicer software.

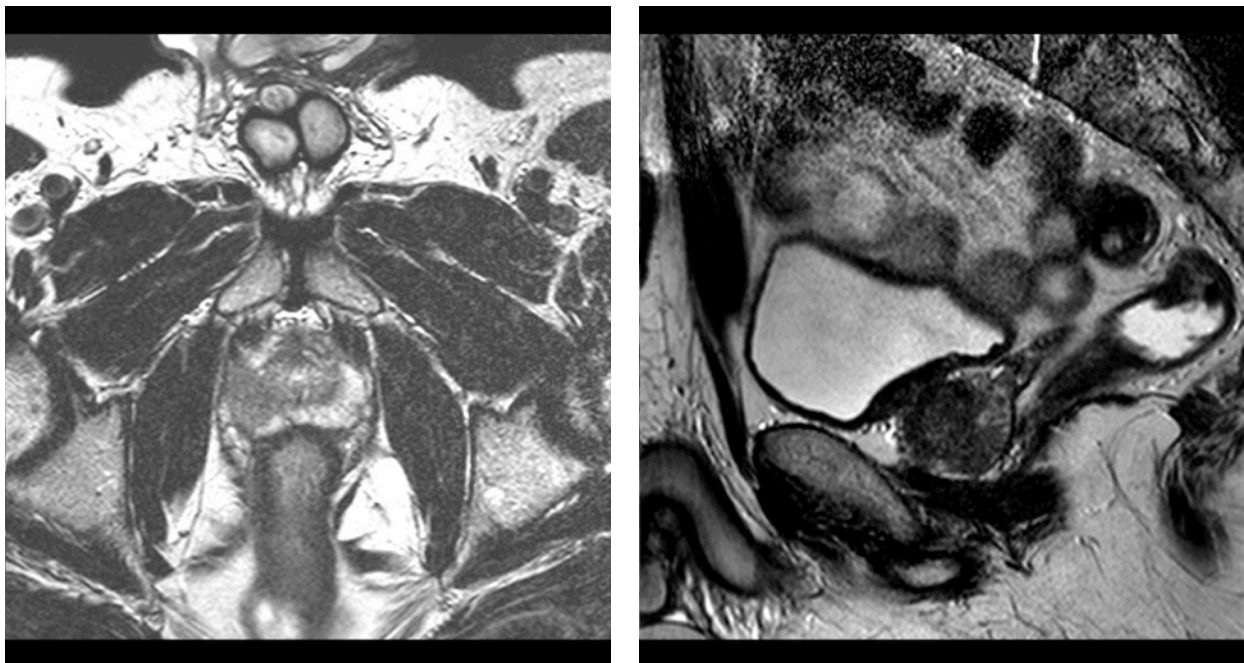


Fig. 6a - Examples of mpMRI acquisitions on patient: T2w images in two planes

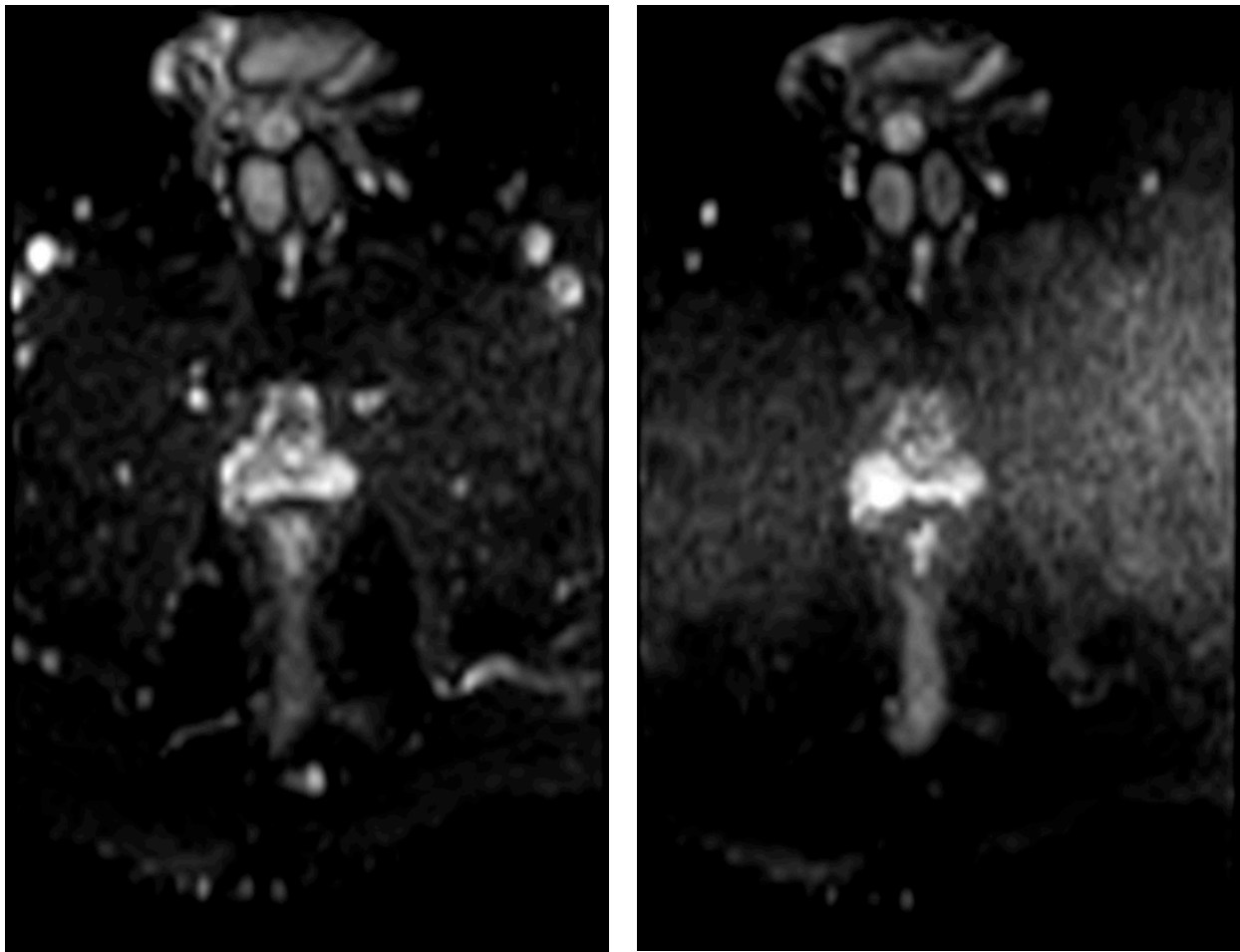


Fig. 6b - Examples of mpMRI acquisitions on patient: DWI images, b0 (left), b 500 (right).

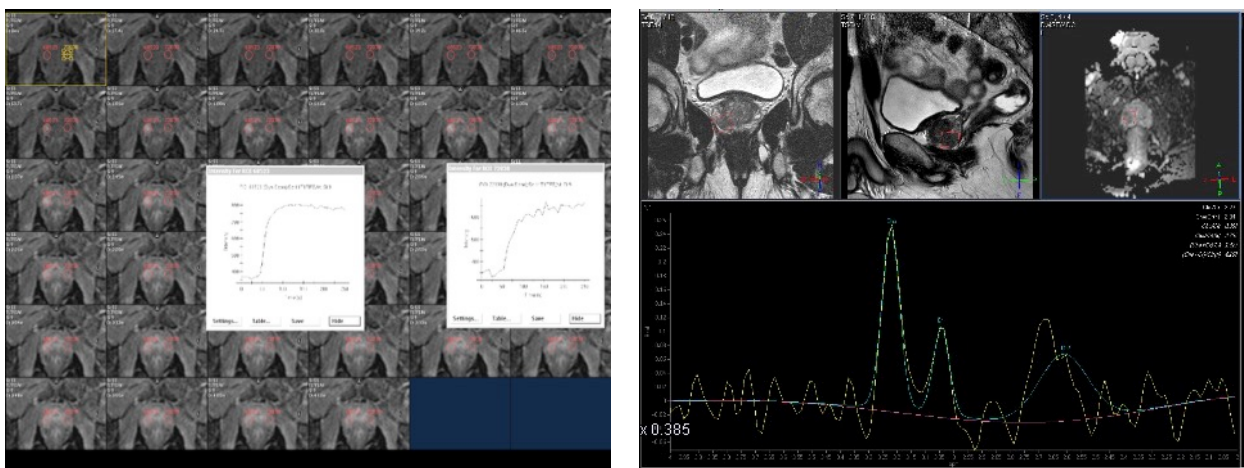


Fig. 6c - Examples of mpMRI acquisitions on patient: DCE (left) and single voxel Spectroscopy (right). In this case data elaboration for DCE and spectroscopy were performed using the Philips software.

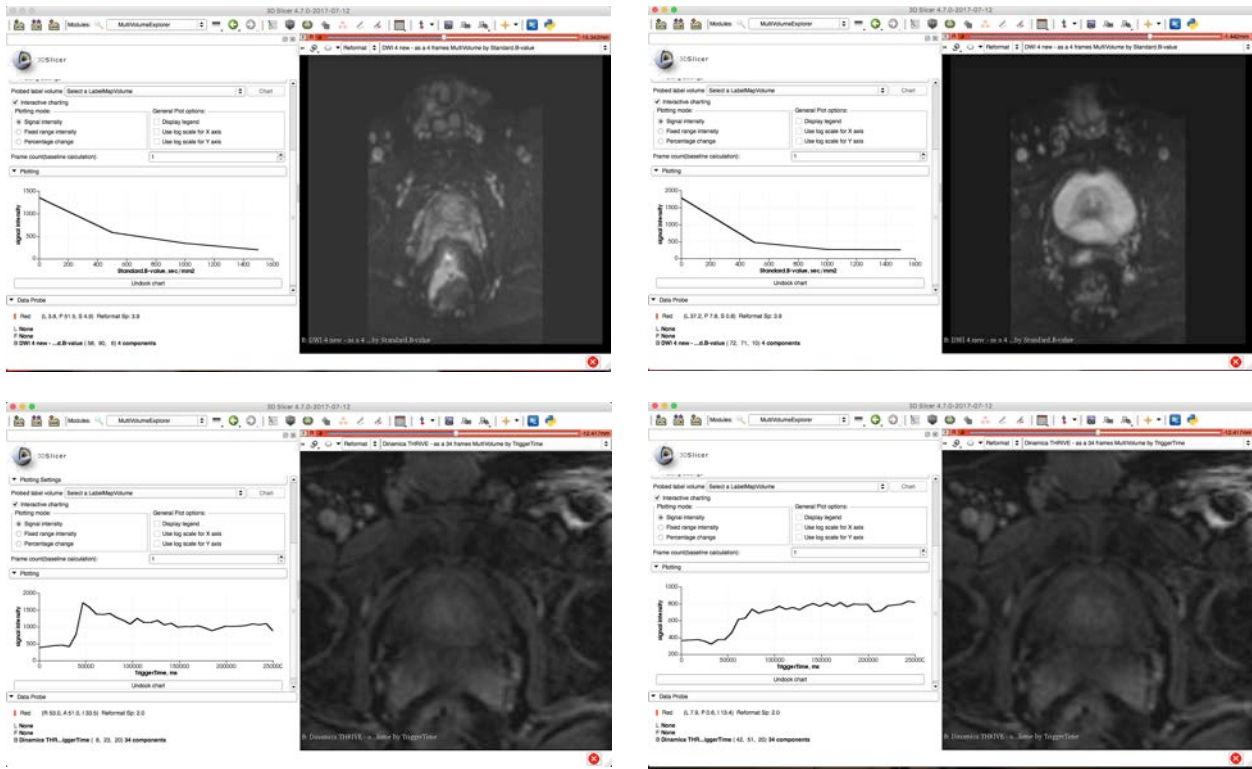


Fig. 7 - mpMRI data visualization using the software 3D Slicer. Top panels: examples of diffusion data in two different points in DWI images. The plots in the right part of images show the behavior of signal intensity versus b-values. Bottom panels: examples of DCE data in two different points in the same image, showing the uptake of the contrast medium in the tissues.

4.3 mpMRI data elaboration

As discussed in detail above mpMRI exam of the prostate usually includes acquisition of T2w, DWI, DCE [17, 20, 92] and Spectroscopy data. ADC maps, DCE parameters and spectroscopy can be calculated on the MRI scanner’s console, however in our case the acquired images have been transferred to an image processing station. There is a variety of medical image computing platforms, both commercial and open source. In our work we used 3D Slicer software [3 - 16] to analyze T2w, DWI and DCE data, extracting Diffusion and DCE maps and parameters, and radiomic features.

In particular DWModeling and PkModeling modules allow respectively to analyze DWI and DCE data, generating maps of diffusion and DCE parameters (e.g Ktrans, the volume transfer coefficient that measures capillary permeability) which can be used to segment tumor or identify ROIs, and then elaborated in order to extract radiomic features.

Maps from DWI and DCE data generated in 3D slicer were confronted using in-house software developed in MATLAB [1, 2] (Fig. 8 and Fig. 10), always with the aim to have an independent and flexible platform.

Spectroscopy data have been elaborated using the scanner vendor software and the independent jMRUI software [1, 3, 19] developed for research. jMRUI has been chosen thanks to a more flexibility in data elaboration [1, 2] (Fig. 9).

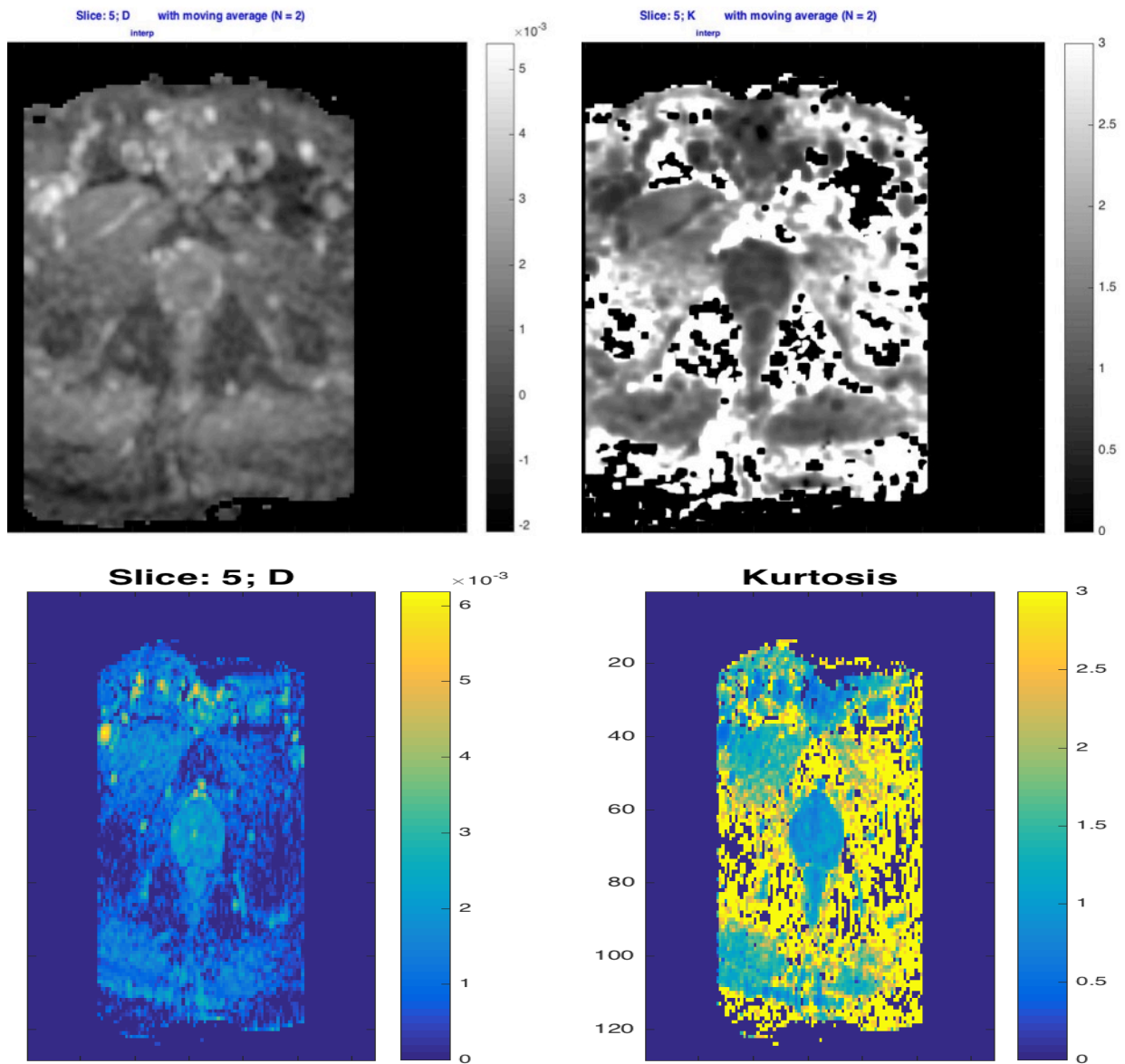


Fig. 8 - Examples of DWI images analysis using an home-made MATLAB software. In this example a diffusion model using the Kurtosis term has been used. Top panels: ADC and Kurtosis maps using a moving average over 2 pixels, and visualized in a gray scale. Bottom panel. Bottom panels: ADC and Kurtosis maps without moving average, and visualized in a color scale.

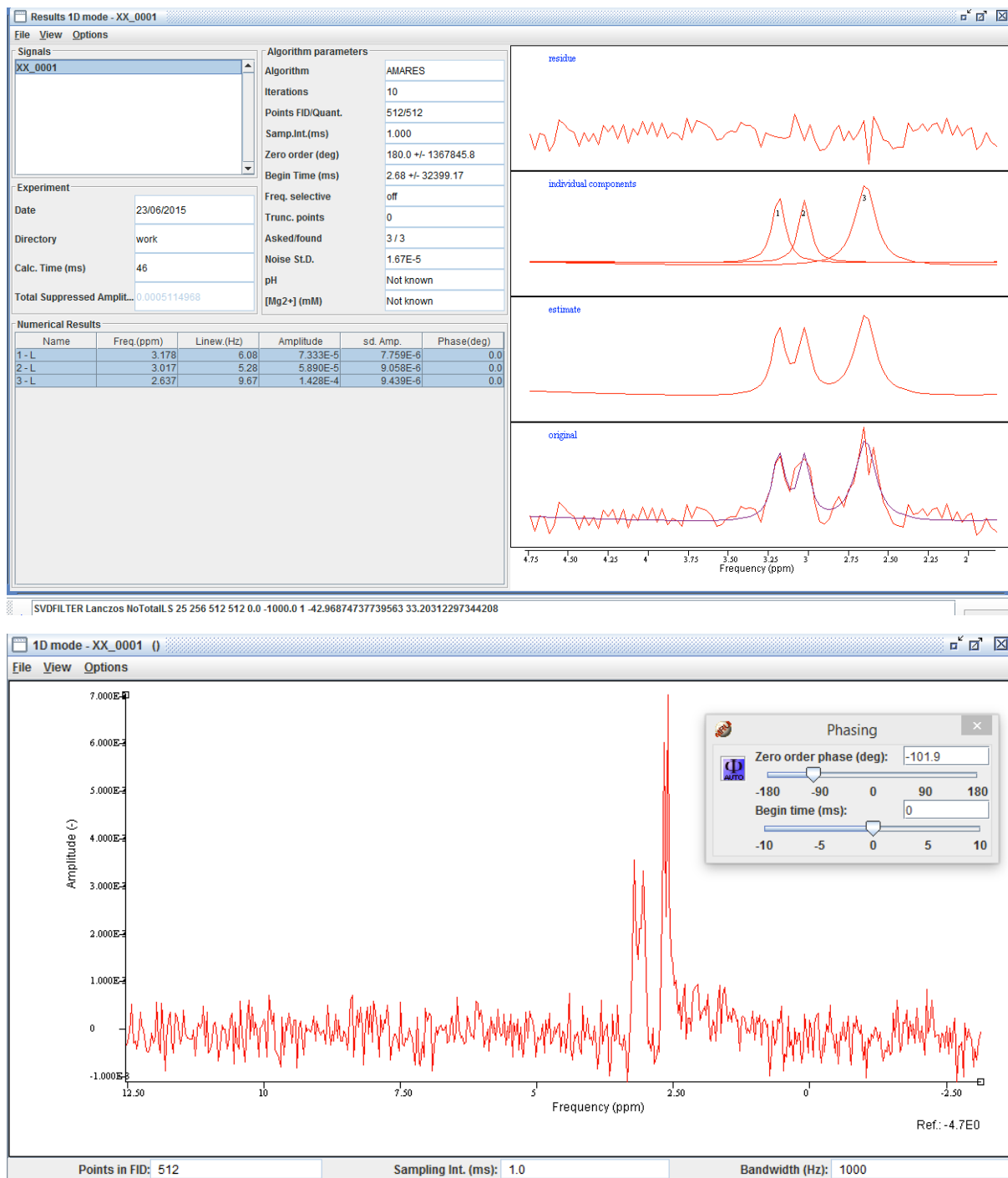


Fig. 9 - Examples of MRS patient data elaboration using jMRUI software. Top panel: data fitting. Bottom panel: spectrum after pre-processing. Citrate peaks and Choline and Creatine peaks are clearly visible.

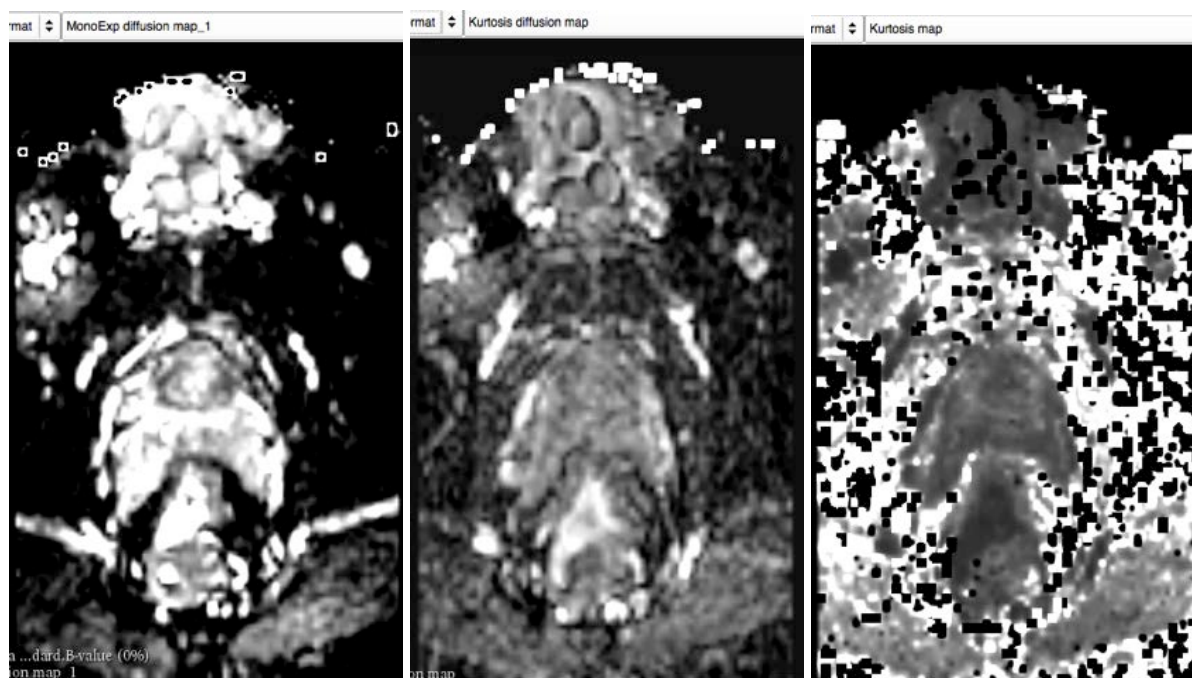


Fig. 10 - Examples of data elaboration using 3D Slicer DWmodeling module. Results coming from two diffusion models are shown. Left: Diffusion map using a mono-exponential model. Center: Diffusion map using the Kurtosis model. Right: map of the Kurtosis term in the Kurtosis-model.

4.4 Segmentation

In our implementation we utilize the habitats concept to identify suspicious lesions. The approach is based on combination of all informations coming from mpMRI and clinical data. ROIs were then manually outlined on both T2w images, diffusion and DCE maps following all the criteria discussed above. In Fig. 11 and Fig. 12 we want to show the ability of 3D Slicer to define different ROIs, exploring images characteristics and allowing to perform radiomic studies. Instead in Fig. 13 and Fig. 14 we show some ROIs, manually drawn on tumor habitat by clinical radiologist. These ROIs have been drawn in T2w, DWI and ADC images.

On these ROIs we will extract some radiomic features underlying the difference between healthy and tumor tissue.

As well describer in this report in different parts, manual segmentation is a critical step in the radiomic workflow, At the same time some efforts are underway for automation of this process, which impacts the entire downstream process. Great care must be used keeping in mind that prostate is a unique organ with distinct zonal morphology. At the moment of writing this report we are working on automatic segmentation in collaboration with other research groups (see Appendix 1).

In the case of patient undertaking a radiotherapy-therapeutic path, one of the possibility is to import the RT-structures coming from the segmented-CT for radiotherapy treatment planning and follow-up. This step requires the co-registration on CT and MRI images, a difficult but possible task today.

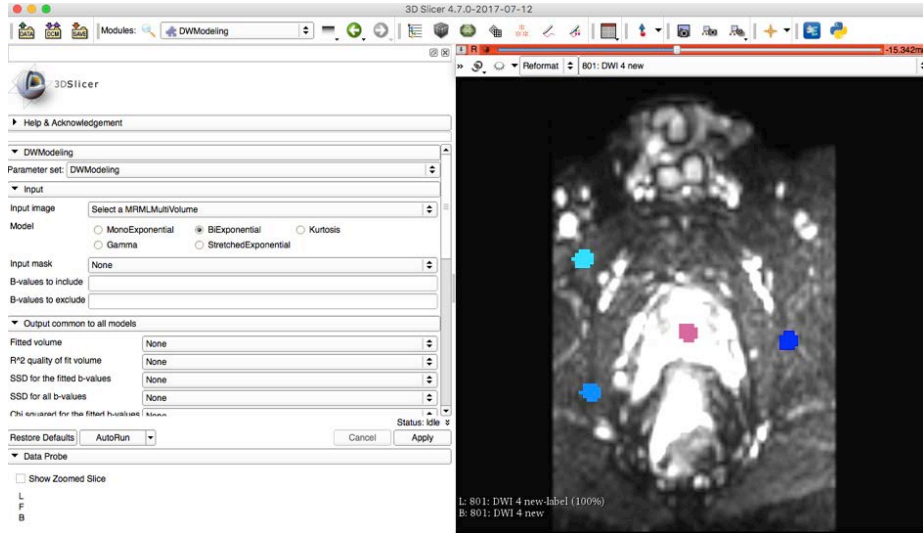


Fig. 11 - Example of ROIs definition using 3D Slicer Editor Module. In this case we selected a DWI image.

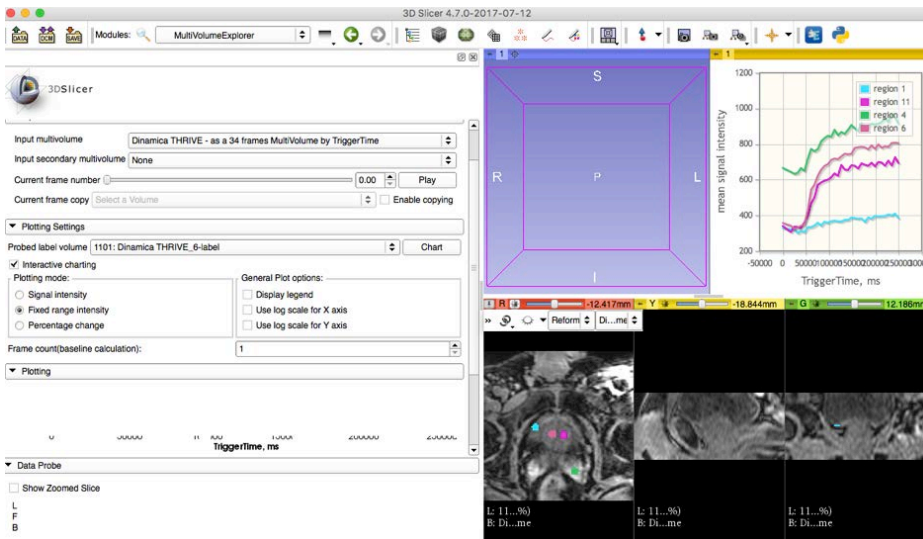


Fig. 12 - 3D Slicer example of data visualization using some ROIs defined on DCE data. In this case the ROIs were drawn only in one acquisition plane.

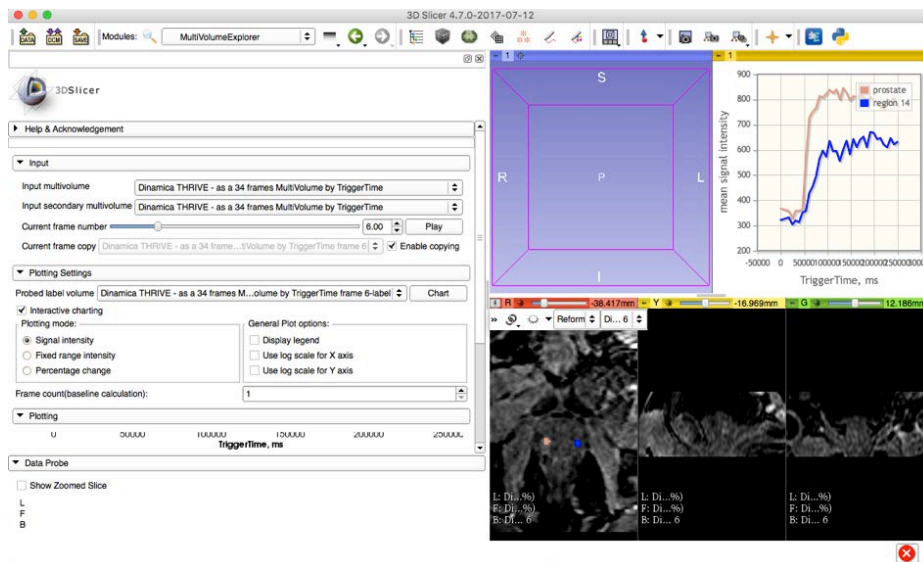


Fig. 13 - DCE data visualization using 3D Slicer. Two ROIs were segmented by radiologist inside the tumor and in the symmetrical part (blue line).

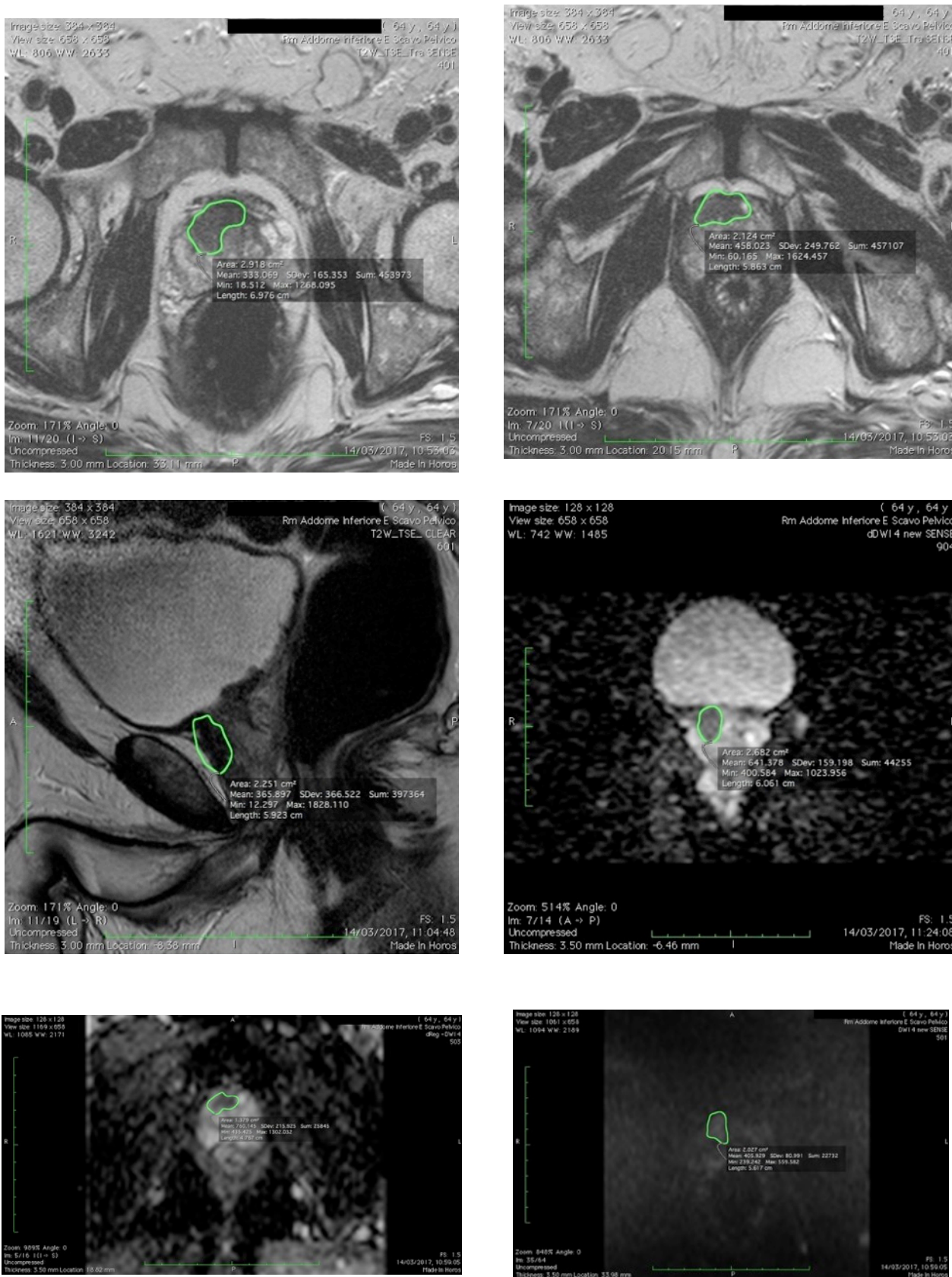


Fig. 14 - Example of Prostate Cancer images manually segmented by radiologist. Top panel: T2w; Middle panel: T2w (left), DWI (right); Bottom panel: ADC (left), DWI (right). ROIs on T2w images were drawn in different acquisition planes.

4.5 Radiomic features extraction

Radiomic features can then be extracted on the outlined ROIs on T2w, diffusion and DCE maps. In our work we decided to use the software 3D slicer, which allows the extraction of these features using the module Radiomics. In Tab. 2 (Appendix 2) we report radiomic results from two ROIs segmented on ADC map by clinical radiologist (Fig. 15).

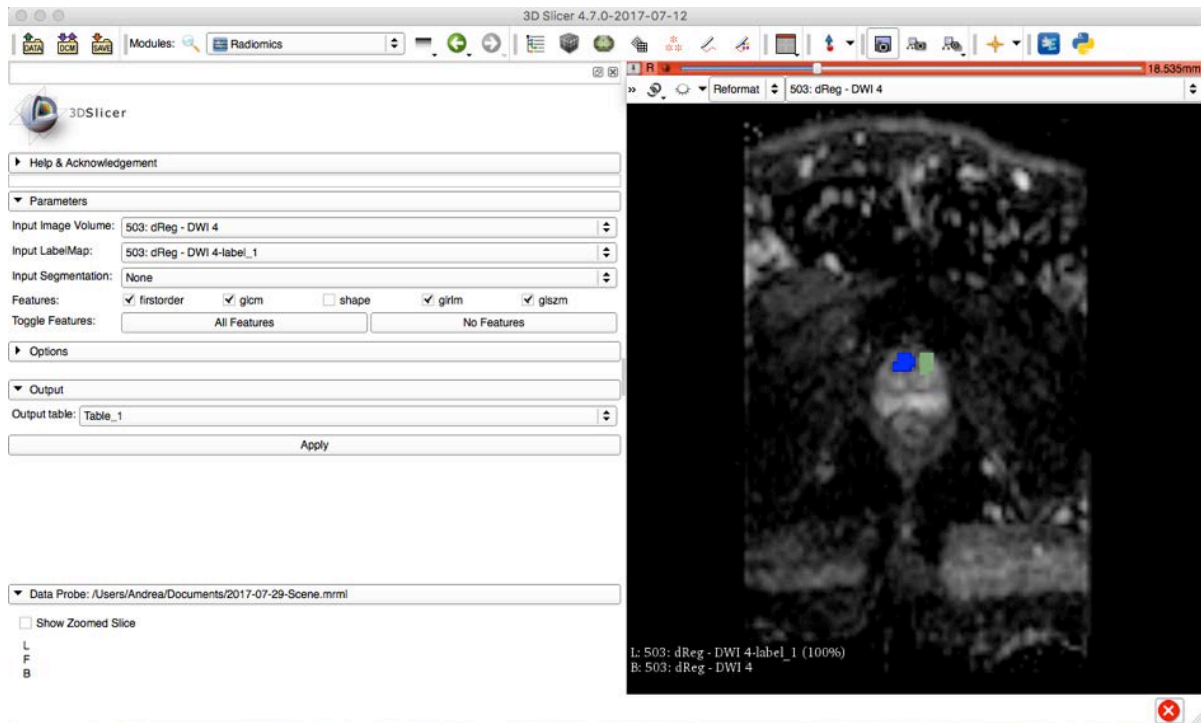


Fig. 15 - Patient ROIs definition on ADC map using 3D Slicer for radiomic analysis. Tumor (blue) vs. healthy tissue (green). ROIs were defined by radiologist using all the mpMRI informations.

An example of histograms generation in two ROIs using a home-made software developed in MATLAB is shown in Fig. 16. The difference in intensity distribution is clearly visible.

In Fig. 17 another example of image elaboration using MATLAB software. In this case we have elaborated a T2w image extracting histogram from the tumor region and evaluating entropy in the image.

Some examples of other results are reported in Appendix 2.

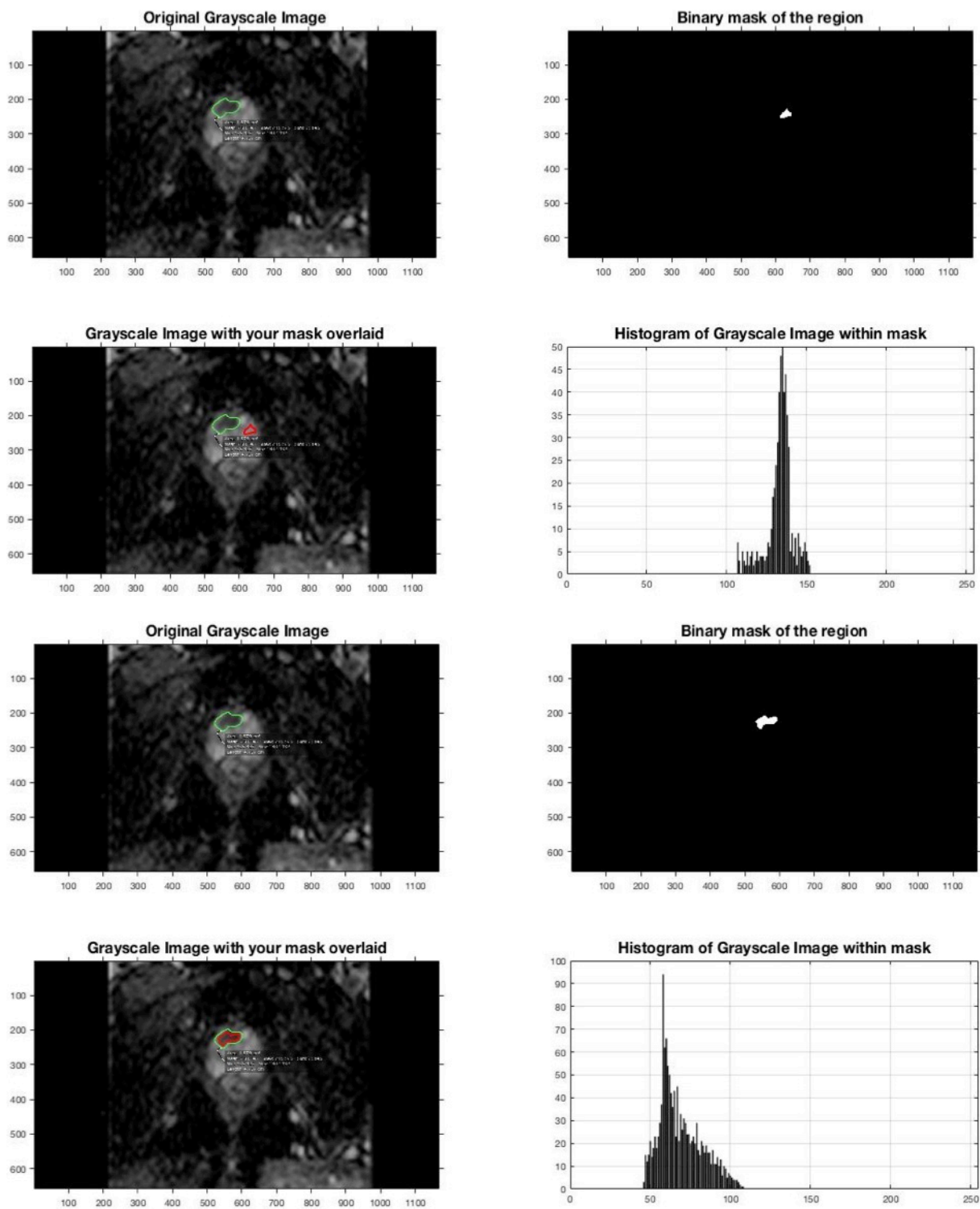


Fig. 16 - Histograms of two ROIs defined by radiologist. Top panel: healthy tissue. Bottom Panel: tumor. This data elaboration has been performed using a home-made software developed in MATLAB.

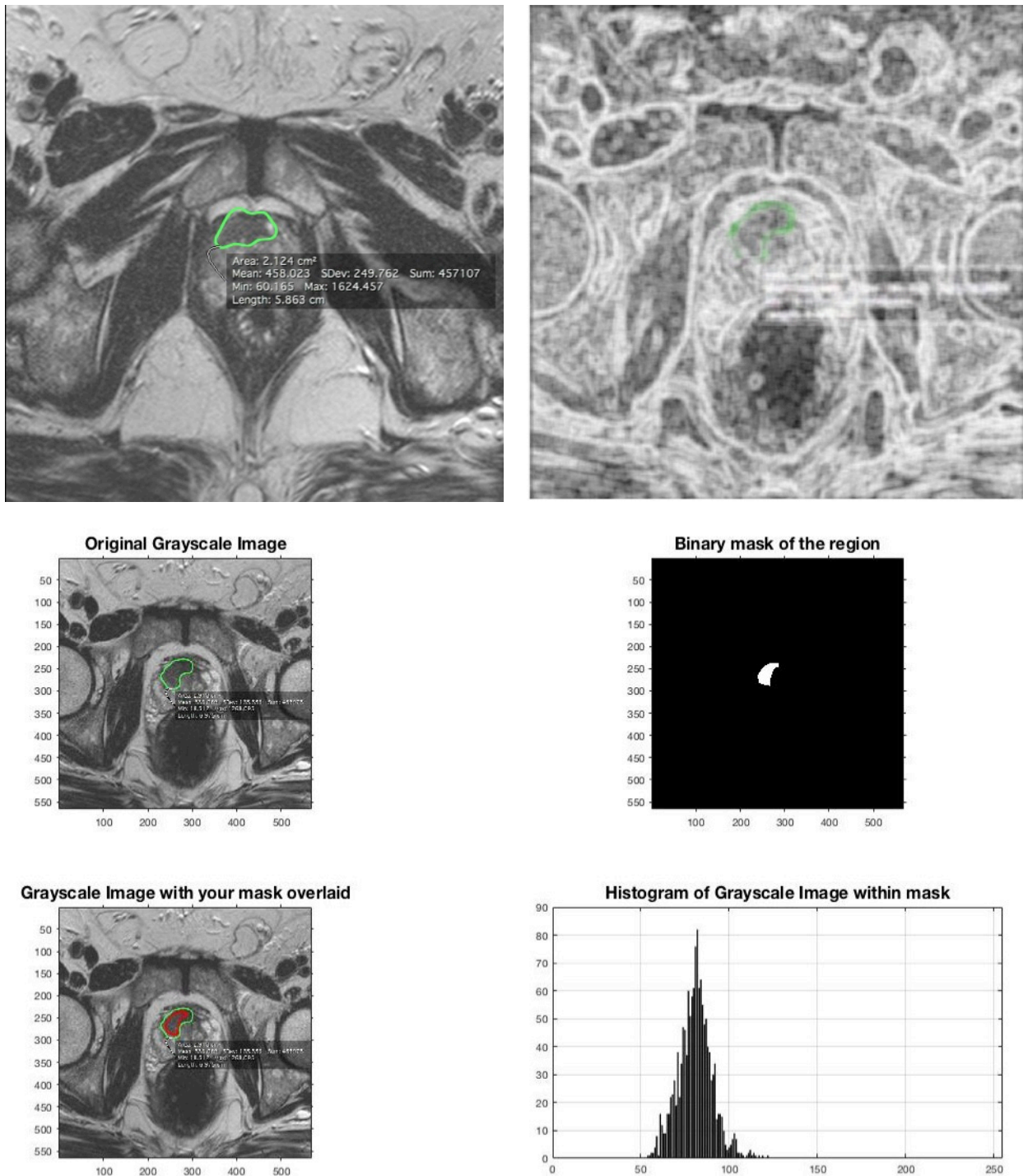


Fig. 17 - Example of T2w image elaboration using MATLAB software. Top panel left: original T2w image with the tumor segmented by radiologist; Top panel right: entropyfilt of the T2w. Bottom: histogram of the tumor ROI.

5. A critical review on the promise and challenges of Radiomics

Radiomics is a new emerging research field with great potential and promises so far envisioned. In this part of the report we will analyze Radiomics limitations, some possible paths for improvement on each step in the workflow, discussing some possibilities for evolution in research and clinics. This part of the report follows very strictly the fundamental review in Ref. [20].

5.1 Repeatability, Reproducibility and Robustness

Repeatability is a measure of precision under identical or near- identical conditions and acquisition parameters, and is evaluated by “test-retest” analysis, a comparison of the results from images acquired within a short time on the same patient. In a study on a dataset consisting of 31 sets of test-retest CT scans that were acquired approximately 15 min apart has been shown that the majority of the radiomic features are repeatable when acquired under the same imaging settings and semiautomatic segmentation [20].

Reproducibility or robustness, in contrast, is measured when measuring system or parameters differ. The major sources for variability of radiomic features are the imaging scanners, the parameters of acquisition and reconstruction of the image, and delineation of ROIs. A good review can be found in Ref. [20, 80].

In the case of radiomic features extracted from MRI images, results depend on the field of view, field strength and slice thickness. Results of the DCE depend on the contrast agent dose, method of administration, and the pulse sequence used. The radiomic features extracted from DWI depend on acquisition parameters and conditions as k-space trajectory, gradient strengths and b-values. The repeatability of MR-based radiomic features still need a deep investigation.

Segmentation represents one of the most critical steps in the radiomic workflow, because many extracted features may depend on the segmented region, and tumors may have indistinct or complex margins: this may potentially lead to inconsistency and lack of reproducibility of results. Manual delineation by an expert radiologist is considered the “gold standard”, though it is prone to high inter-observer variability and represents a time-consuming task. It was shown that the semiautomatic segmentation algorithm implemented in the 3D-Slicer open source platform, produce contours of lung tumor on CT which were more reproducible than manually drawn regions and yield radiomic features with significantly higher reproducibility compared to those extracted from the manual segmentations. Recently available fully automatic segmentation tools for brain cancer from MRI are as accurate as manual segmentation by medical experts. Some references can be found in [20].

5.2 Sample size and statistical power: Big Data and Radiomics

In this era of Big Data it should be possible to have a good patients database, however this crucial step for the radiomic workflow is very hard to build [53, 133, 149]. Some strategies for building good dataset are reported in [53, 71, 80, 92].

Given the large number of imaging features extracted in Radiomics studies, a small dataset reduces its power and increases the risk of overfitting the data [20, 67]. Then radiomic studies involving small numbers of subjects with respect to the number of radiomic features should be avoided.

Moreover most radiomics studies do not report sufficient validations in independent cohorts, thereby limiting generalizability to additional patient populations, imaging by different scanner types, etc.

Image data sharing across sites can be a solution to build large data sets for Radiomics and could serve as high-quality datasets to be used for external validation [80, 104, 105, 107 - 109]. Various online repositories of imaging datasets are already available as the “The Cancer Imaging Archive” (TCIA) hosted by the National Cancer Institute, and the “Lung Image Database Consortium”, the Reference Image Database to Evaluate Response to therapy in lung cancer [20].

In Fig. 18 we reported a general scheme of precision medicine applied to PCa. Sources of data are shown along with new emerging technologies for their elaboration and interpretation.

The problem of Big Data in medicine and their expected impact is a more general problem. In Ref. [134, 135, 136] the potential impact of big data analysis to improve health, prevent and detect disease at an earlier stage, and personalize interventions is shown.

5.3 Standardization and benchmarking

Usually images used in radiomic studies have been acquired from different institutions, which probably follows different acquisition protocols or simply use scanners from different vendors. These differences might be the source of some problems. Acquisition and reconstruction protocols should be standardized in order to limit data variability, especially in view of multicenter studies that are expected to create the most robust models [62, 63, 80]. The radiomic workflow should be follow precise recommendations in order to increase quality of radiomic studies [20, 80, 93 - 102].

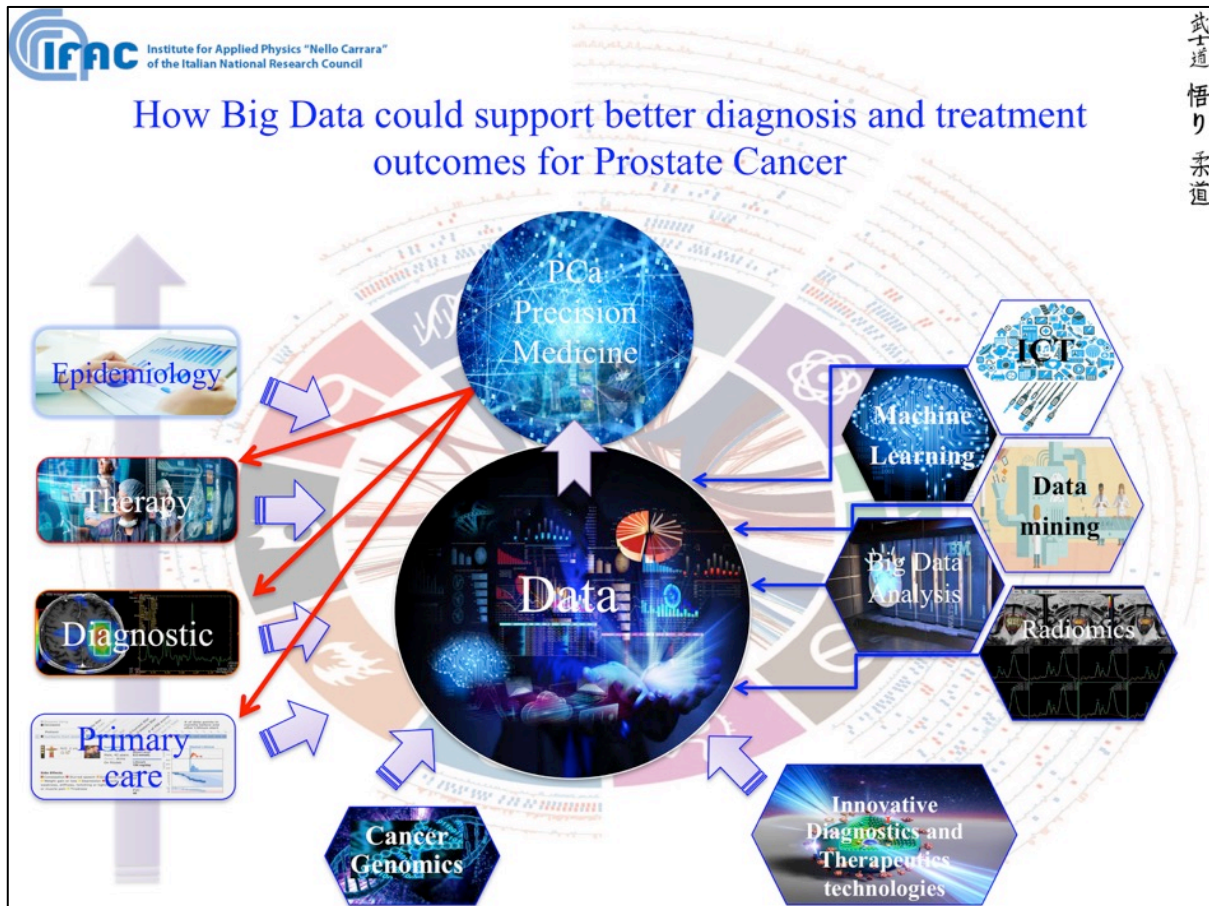


Fig. 18 - General scheme of Big Data analysis aimed to PCa Precision Medicine. All the sources of data are included along with the new technologies for their elaboration.

5.4 Standardization and benchmarking

These should cover for example the discretization method and the bin, the segmentation method (manual, semiautomatic or automatic), the definitions of various radiomic features, and indications on which features are most stable. The more reliable and efficient machine learning algorithms should also be indicated in order to identify stable and reproducible features in the high dimensional feature space created by Radiomics [20, 132].

Furthermore there is need for benchmarks with using test objects with known physical properties values of radiomic features, e.g. phantoms have been proposed with known features. The mathematical steps, as feature extraction and calculation should be tested using open-source verified formulae and codes. Publicly available database with cohorts of patients, images and clinical data should be used by research groups for benchmarking of the radiomic workflow. Finally, standards for publishing methods, results, and their uncertainty should be recommended, as well as ways to improve the peer review e.g. insist on at least one “statistical reviewer” with knowledge of machine-learning methodologies [20, 132, 149 - 154].

For future prospective studies, it should be strongly recommended to adopt acquisition and reconstruction standards, as proposed by, for instance, the Quantitative Imaging Biomarker Alliance, Quantitative Imaging Network, American Association of Physicists in Medicine and European Association of Nuclear Medicine. Nonetheless, standardization can be challenging with the introduction of new, state-of-the-art imaging equipment (e.g. photoacoustic imaging) in different institutes. At the same time the use of the enormous amount of retrospective data available can be very hard due a lack of standardization in the acquisition protocols [20].

5.5 Limitations and pitfalls

The principal criticism to Radiomics is that the link between the imaged properties of tumors and tumor biology is not straightforward. Most radiomic studies have shown statistical correlation between radiomic

features and genetic footprint or prognosis, but correlation does not imply causation [21]. Establishing this link is necessary for tailoring the treatment to the individual patient based on the properties of tumors coming from imaging [22].

For example some MRI studies have shown that intensity histogram-based radiomic features can be potentially useful for predicting cancer response to treatment [47, 55 – 59, 62, 63, 64, 79]. In pre-clinical model has been observed that mice with sarcomas treated with combinations of MK1775, a cell cycle checkpoint inhibitor, and gemcitabine showed a substantial change in the apparent diffusion coefficient (ADC) histogram, skewness, kurtosis, entropy, and average ADC shortly after treatment compared to the untreated control group [60]. In human patients with head-and-neck cancer, tumors that responded poorly to chemo-radiotherapy demonstrated a significantly greater increase in average ADC and higher values in kurtosis and skewness on mid-treatment DWI than tumors with a better therapeutic response [58]. The skewness of K-trans was found to be a promising predictor of progression free survival and overall survival of patients with stage IV head-and-neck cancer [57]. The findings of these aforementioned studies may support the notion that therapy induced changes in tumor microenvironment and composition can be potentially described by changes in the intensity-histogram shape [47].

For CT imaging, [31, 47, 79] assessed the prognostic values of 440 shape- and intensity-based and textural features. They identified features that were predictive of patients' survival on a dataset consisting of more than 420 lung cancer patients. The prognostic value of these features was then validated on three independent datasets, including one lung cancer (225 patients) and two head-and-neck cancer (231 patients) cohorts. Their results confirmed the potential use of radiomic features in outcome prediction and describing intra-tumoral heterogeneity, furthermore showing that prognostic ability may be transferred from one disease type to another (i.e. from lung to head-and-neck cancer). In study [61] has been noted that not all radiomic features that significantly predicted lung cancer patients' survival also predicted survival in head-and-neck cancer patients and vice-versa. Their results thus suggested that some radiomic features could be cancer-specific [61].

5.6 Future directions in the Radiomics research field

Radiomics research field has grown in the last years thanks to some intrinsic characteristics for example the possibility of extending the number of features potentially holding prognostic and/or predictive values without a significant burden. Indeed the Radiomics platform will be able to automatically select the features and analyze the possible correlation [20, 80].

Another important aspect is the possibility to combine hybrid imaging modalities in order to have a more deeper understanding of tumor habitat. 3D informations, as for example dose distribution delivered in radiotherapy calculated on pre-treatment CT, can be integrated in the radiomic analysis. Informations can be added from other -omics data, generating pan-omics type models for detecting tumors boundaries, modeling response, and deciphering the underlying molecular biology [20, 80].

At the same time machine learning and the produced prediction models in Radiomics must improve their performances, exploring new approaches coming from other research fields.

In the research area, Radiomics is expected to spread where new signatures could be identified by means of data mining and correlation with endpoints. Thanks to Radiomics, we expect that all theranostic approaches can be revised, exploring its potential not only in oncology and cardiovascular diseases but e.g. in the case of neurodegenerative [156 - 162], orphan pathologies and as a research tool in the drug development. This last possibility should be investigated with great care, because the possibility of quickly assessing if the drug has reached the target and if it has produced the expected effect by means of non-invasive imaging will speed up the development of many, innovative personalized drugs, decreasing their development costs and then the burden for healthcare systems. An interesting work about the prediction of longevity using feature engineering and deep learning methods in a radiomics framework has been presented [132]. In this work authors showed proof-of-concept experiments to demonstrate how routinely acquired cross-sectional CT imaging may be used to predict patient longevity as a proxy for overall individual health and disease status using computer image analysis techniques. This work demonstrates that radiomics techniques can be used to extract biomarkers relevant to one of the most widely used outcomes in epidemiological and clinical research – mortality, and that deep learning with convolutional neural networks can be usefully applied to radiomics research [132].

Thanks to the possibility in optimizing the end-to-end diagnosis-treatment-follow-up chain, Radiomics will increasingly affect the clinical practice [20, 80]. In particular, the possibility of decreasing toxic treatments in case of minimal improvements as well as boosting the treatment in case of high likelihood of failure/recurrence is a way to pave the road of personalized medicine. Imaging is at present used in oncology for guiding and in some instances for adapting therapies. However we must remember that clinical trials are still needed to further validate the importance and additive role of Radiomics in clinical practice.

Costs in the health care system can be reduced by the use of Radiomics approach. As a matter of fact,

Radiomics is relatively cost-effective given that images are already available for most patients. Furthermore, Radiomics can reduce the need for biopsy and providing early identification of patients who do not respond to chemotherapy, it has also the advantage of avoiding unnecessary treatment with its risk of toxicity [20].

Approaches that look into longitudinal variations in radiomic features would be useful, as for example in delta-radiomics, the analysis of the percentage change of radiomic features assessed in repeated scans during the course of chemo and radio-treatment [20, 26, 27]. Indeed we know that radiotherapy induces changes in textural features in the tumor during the treatment, which are related to prognosis [20, 25]. Mid treatment information from PET/MRI or even daily Cone Beam CT images, currently acquired for alignment setup, could be applied [27] for adapting radiotherapy in order to boost radioresistant tumors or tumor subvolumes (e.g. hypoxic). Also organs at risk could benefit by Radiomics-adapted radiotherapy, as early changes of textural features in some organs during the treatment were found to be related to the appearance of side effects [20, 65].

Radiomics in the study of other diseases

Radiomics is showing its potential in cancer disease, however as stated above, its applications are spreading in different field of clinical research [138, 139]. In study [138] texture analysis has been applied to Dopamine transporter (DAT) SPECT imaging for diagnostic purposes in suspected Parkinsonian syndromes. In particular image analysis included registration of SPECT images onto corresponding MRI images, automatic ROIs extraction on the MRI images, followed by computation of Haralick texture features. 141 subjects were analyzed from the Parkinson's Progressive Marker Initiative (PPMI) database, including 85 PD and 56 healthy controls (HC) (baseline scans with accompanying 3 T MRI images). These results demonstrated the ability to capture valuable information using advanced texture metrics from striatal DAT SPECT, enabling significant correlations of striatal DAT binding with clinical, motor and cognitive outcomes, and suggesting that textural features hold potential as biomarkers of PD severity and progression.

In Ref. [140] a work using multi-scale image textures to investigate links between neuroanatomical regions and clinical variables (age, gender, autism) in MRI was proposed, while in [141] an exploratory study was set to investigate whether a quantitative image analysis of the labyrinth in conventional MRI scans using a radiomics approach showed differences between patients with Ménière's disease and the control group.

Radiomic features based on texture have also been used to identify subtle differences between brain tissues in control subjects and those of Alzheimer's patients, related to cognitive impairment severity [142, 143, 144, 145, 157, 161, 162]. In [160] an example of radiomic analysis on Parkinson disease is shown, while examples of application to multiple sclerosis texture analysis are reported in [156, 158]. In [161] an important study that correlates genetic data with imaging analysis is reported.

6. Conclusions

Concluding we can say that in this era of Big Data, in medical research fields too, a new field of clinical data science called "Radiomics" is emerging, allowing the integration of multiple data sources with the aim of personalized medicine [71, 80].

The aim of this report was to give to the reader a review about Radiomics, focusing on the application to Prostate Cancer using multiparametric Magnetic Resonance Imaging, and illustrating some preliminary results obtained in our study.

Our results come from the radiomic analysis of a suitable retrospective database, built using mpMRI images acquired in the framework of the project IRINA between IFAC-CNR and the Department of Radiology of USL Toscana Centro, Santa Maria Nuova Hospital.

While Radiomics will allow better characterization of patients and their diseases through new applications of genomics and improved methods of phenotyping, it will also add to the challenges of data management and interpretation [71].

7. Acknowledgments

This work has been developed in the framework of the project IRINA - "Imaging Molecolare di risonanza magnetica della biodistribuzione di nanoparticelle e vettori cellulari per applicazioni teranostiche" thanks to financial support by "Ente Cassa di Risparmio di Firenze" [Rif. Pratica n. 2015.0926, Sede Legale: via Bufalini 6, 50122 Firenze, www.entecarifirenze.it].

Radiomics is an emerging interdisciplinary research field, inevitably involving different people with different skills. I would like to thank to Sonia Centi, Lucia Cavigli, Paolo Matteini, Francesco Baldini from IFAC-CNR for fruitful discussions about nanomedicine, photoacoustic imaging and applications of mpMRI to nanomedicine. A special thanks to Alessandra Flori, Luca Menichetti and Daniele De Marchi from IFC-CNR and Fondazione Gabriele Monasterio for discussions, mpMRI data acquisition and elaboration; Franco Cosi and

Andrea Donati from IFAC-CNR for the realization of phantoms suitable for test of repeatability, reproducibility and robustness in mpMRI; Roberto Incalcaterra, Laura Guerrini, Angela Konze and Giacomo Belli from Santa Maria Nuova Hospital and Azienda Ospedaliera Universitaria Careggi respectively for helping in the mpMRI acquisitions from patients and phantoms. A thanks to Chiara Romei from Cisanello Hospital (Azienda Ospedaliero Universitaria Pisana) for fruitful discussions about mpMRI of lung diseases, and to Simona Perboni, Maria Simona Pino, Paolo Bastiani, Simona Fondelli and Matteo Consalvo from the Oncological, Radiotherapy and Diagnostic departments of USL Toscana Centro (Santa Maria Annunziata Hospital) for discussion on the clinical aspect of data acquisition and statistical elaboration. About discussions on Statistical Analysis and Data mining, i would like to thank Francesco Stingo and Anna Gottard from the Statistical Department "G. Parenti" of the University of Florence. For 3D Slicer support in data segmentation i want to say thank you to Maria Francesca Spadea and Francesco Zaffino from the Imagenglab, University Magna Graecia of Catanzaro. Thanks to Matteo Benelli from Sandro Pitigliani Department of Medical Oncology (Hospital of Prato, Istituto Toscano Tumori, Italy) for introducing me to the amazing field of genomics. For the ethical aspects of this work and for support i want to say thank you to Monica Toraldo di Francia, actually at the Stanford University (Breyer Center for Overseas Studies in Florence), and to Antonio Ciccarone and Salvatore De Masi from A.O.U. Meyer in Florence.

Appendix 1. First steps in automatic prostate segmentation

Thanks to the collaboration with Maria Francesca Spadea and Paolo Zaffino from ImagEngLab (<http://www.imagenglab.com/newsite/>), University of Magna Grecia (Italy), we are moving toward automatic segmentation of prostate in MRI images. In the first steps we are using CT images from patient undergoing a radiotherapy treatment, extracting the structures defined by radiotherapists (RT-structures), projecting in the MRI images dataset of the patient (T2, DWI, ecc.), then verifying how the algorithms are able to perform this alignment (Fig. 19). This is just the first step in the workflow to automatic segment the entire prostate without a priori knowledge (RT-structures).

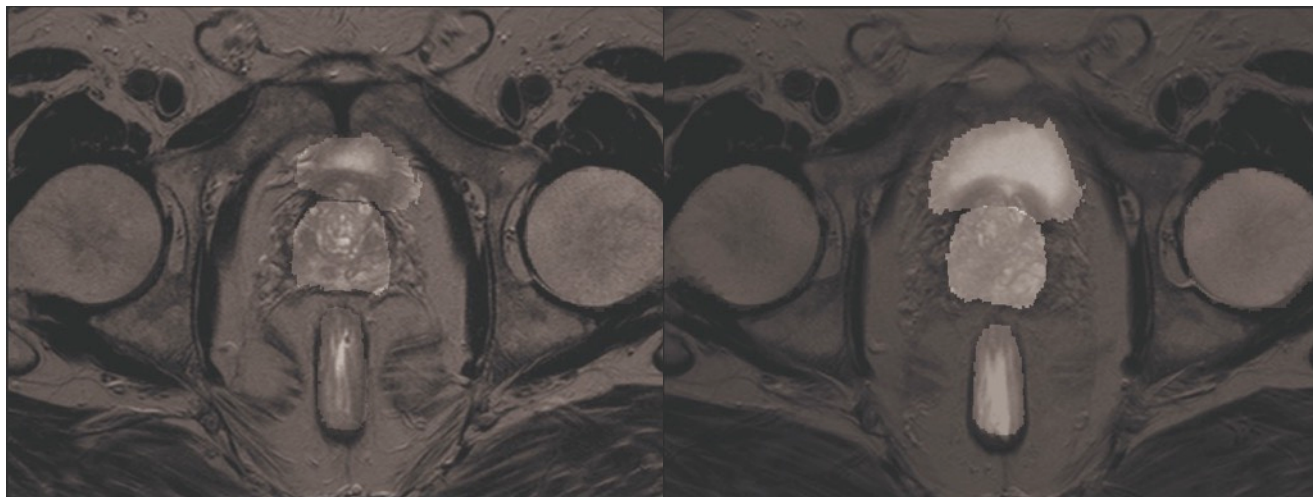


Fig. 19 - Examples of CT structures projected on MRI T2 image. In this example prostate, bladder, rectum and the head of the femur have been segmented. The two images show different T2-MRI slices. [Results obtained in collaboration with Maria Francesca Spadea and Paolo Zaffino from ImagEngLab, University of Magna Grecia (Italy)]

Appendix 2. Two examples of ADC and DCE data radiomic analysis.

Tab. 2: Radiomic results of the two ROIs defined by radiologist on ADC map. See Fig. 15.

| Label | Input image type | Feature Class | Feature Name | Tumor Value | Healthy tissue |
|--------------------------------------|------------------|---------------|-----------------------|--|--|
| 503: dReg - DWI 4-label_1_label_3 06 | general | info | BoundingBox | (59, 57, 4, 5, 4, 1) | (65, 57, 4, 3, 5, 1) |
| 503: dReg - DWI 4-label_1_label_3 06 | general | info | GeneralSettings | {'distances': [1], 'additionalInfo': True, 'enableCEExtensions': True, 'force2D': False, 'interpolator': 'sitkBSpline', 'resampledPixelSpacing': None, 'label': 1, 'normalizeScale': 1, 'normalize': False, 'force2Ddimension': 0, 'removeOutliers': None, 'minimumROISize': None, 'binWidth': 25, 'minimumROIDimensions': 1, 'symmetricalGLCM': True, 'padDistance': 5} | {'distances': [1], 'additionalInfo': True, 'enableCEExtensions': True, 'force2D': False, 'interpolator': 'sitkBSpline', 'resampledPixelSpacing': None, 'label': 1, 'normalizeScale': 1, 'normalize': False, 'force2Ddimension': 0, 'removeOutliers': None, 'minimumROISize': None, 'binWidth': 25, 'minimumROIDimensions': 1, 'symmetricalGLCM': True, 'padDistance': 5} |
| 503: dReg - DWI 4-label_1_label_3 06 | general | info | ImageHash | 00969d79fad99623de54fae9956aa004dd93ee5b | 00969d79fad99623de54fae9956aa004dd93ee5b |
| 503: dReg - DWI 4-label_1_label_3 06 | general | info | ImageSpacing | (2,23684215545654, 2,236842155456541, 3,849999911263533) | (2,23684215545654, 2,236842155456541, 3,849999911263533) |
| 503: dReg - DWI 4-label_1_label_3 06 | general | info | InputImages | {'Original': {}} | {'Original': {}} |
| 503: dReg - DWI 4-label_1_label_3 06 | general | info | MaskHash | 467cbf633815f75506fbbb319a5c725a49be6333 | 0c4707a86617da7bacb767a2c099e0126e3012a2 |
| 503: dReg - DWI 4-label_1_label_3 06 | general | info | Version | 1,2,0,post13+gcb9c73b | 1,2,0,post13+gcb9c73b |
| 503: dReg - DWI 4-label_1_label_3 06 | general | info | VolumeNum | 1 | 1 |
| 503: dReg - DWI 4-label_1_label_3 06 | general | info | VoxelNum | 16 | 14 |
| 503: dReg - DWI 4-label_1_label_3 06 | original | first order | InterquartileRange | 86,5811234689 | 162,6876547 |
| 503: dReg - DWI 4-label_1_label_3 06 | original | first order | Skewness | 0,57620660364 | 0,125877817 |
| 503: dReg - DWI 4-label_1_label_3 06 | original | first order | Uniformity | 0,1484375 | 0,112244898 |
| 503: dReg - DWI 4-label_1_label_3 06 | original | first order | MeanAbsoluteDeviation | 60,5230891324 | 134,3702669 |

| | | | | | |
|--------------------------------------|----------|-------------|-----------------------------|----------------|-------------|
| 503: dReg - DWI 4-label_1_label_3 06 | original | first order | Energy | 5112336,35641 | 16013903,38 |
| 503: dReg - DWI 4-label_1_label_3 06 | original | first order | RobustMeanAbsoluteDeviation | 34,3407518812 | 76,53081848 |
| 503: dReg - DWI 4-label_1_label_3 06 | original | first order | Median | 554,490441573 | 1033,139532 |
| 503: dReg - DWI 4-label_1_label_3 06 | original | first order | TotalEnergy | 98480629,6942 | 308481128,6 |
| 503: dReg - DWI 4-label_1_label_3 06 | original | first order | Maximum | 734,01699774 | 1370,447921 |
| 503: dReg - DWI 4-label_1_label_3 06 | original | first order | RootMeanSquared | 565,261905912 | 1069,509346 |
| 503: dReg - DWI 4-label_1_label_3 06 | original | first order | 90Percentile | 662,418518914 | 1286,279931 |
| 503: dReg - DWI 4-label_1_label_3 06 | original | first order | Minimum | 435,424823081 | 770,6117758 |
| 503: dReg - DWI 4-label_1_label_3 06 | original | first order | Entropy | 2,95281953111 | 3,324862958 |
| 503: dReg - DWI 4-label_1_label_3 06 | original | first order | StandardDeviation | 78,6687595439 | 167,6612689 |
| 503: dReg - DWI 4-label_1_label_3 06 | original | first order | Range | 298,592174659 | 599,8361448 |
| 503: dReg - DWI 4-label_1_label_3 06 | original | first order | Variance | 6188,77372817 | 28110,30109 |
| 503: dReg - DWI 4-label_1_label_3 06 | original | first order | 10Percentile | 470,42852384 | 839,7706028 |
| 503: dReg - DWI 4-label_1_label_3 06 | original | first order | Kurtosis | 2,9167693155 | 2,4450027 |
| 503: dReg - DWI 4-label_1_label_3 06 | original | first order | Mean | 559,760885153 | 1056,285918 |
| 503: dReg - DWI 4-label_1_label_3 06 | original | glcm | SumVariance | 19,3743979568 | 93,76417447 |
| 503: dReg - DWI 4-label_1_label_3 06 | original | glcm | Homogeneity1 | 0,318818091631 | 0,232219347 |
| 503: dReg - DWI 4-label_1_label_3 06 | original | glcm | Homogeneity2 | 0,219789180164 | 0,154447428 |

| | | | | | |
|--|----------|------|--------------------|------------------|-------------|
| 503: dReg - DWI 4- label_1_label_3 06 | original | glcm | ClusterShade | 25,9380597591 | 76,27606873 |
| 503: dReg - DWI 4- label_1_label_3 06 | original | glcm | MaximumProbability | 0,106755050505 | 0,085723304 |
| 503: dReg - DWI 4- label_1_label_3 06 | original | glcm | Idmn | 0,911751705086 | 0,905370448 |
| 503: dReg - DWI 4- label_1_label_3 06 | original | glcm | Contrast | 18,7837121212 | 75,01194986 |
| 503: dReg - DWI 4- label_1_label_3 06 | original | glcm | DifferenceEntropy | 2,57923574753 | 2,756183658 |
| 503: dReg - DWI 4- label_1_label_3 06 | original | glcm | InverseVariance | 0,236623762505 | 0,178071753 |
| 503: dReg - DWI 4- label_1_label_3 06 | original | glcm | Dissimilarity | 3,53320707071 | 7,038194444 |
| 503: dReg - DWI 4- label_1_label_3 06 | original | glcm | SumAverage | 10,8382575758 | 27,0436057 |
| 503: dReg - DWI 4- label_1_label_3 06 | original | glcm | DifferenceVariance | 5,86713798337 | 24,9297257 |
| 503: dReg - DWI 4- label_1_label_3 06 | original | glcm | Idn | 0,803410888766 | 0,79907102 |
| 503: dReg - DWI 4- label_1_label_3 06 | original | glcm | Idm | 0,219789180164 | 0,154447428 |
| 503: dReg - DWI 4- label_1_label_3 06 | original | glcm | Correlation | 0,00644540612082 | 0,09072918 |
| 503: dReg - DWI 4- label_1_label_3 06 | original | glcm | Autocorrelation | 29,5578282828 | 187,9004329 |
| 503: dReg - DWI 4- label_1_label_3 06 | original | glcm | SumEntropy | 2,9342592549 | 2,864138203 |
| 503: dReg - DWI 4- label_1_label_3 06 | original | glcm | AverageIntensity | 5,41912878788 | 13,52180285 |
| 503: dReg - DWI 4- label_1_label_3 06 | original | glcm | Energy | 0,0616049063871 | 0,065627101 |
| 503: dReg - DWI 4- label_1_label_3 06 | original | glcm | SumSquares | 9,53952751951 | 42,19403108 |
| 503: dReg - DWI 4- label_1_label_3 06 | original | glcm | ClusterProminence | 891,849772108 | 25534,26337 |

| | | | | | |
|--------------------------------------|----------|-------|----------------------------------|-----------------|--------------|
| 503: dReg - DWI 4-label_1_label_3 06 | original | glcm | Entropy | 4,11593599106 | 3,992700613 |
| 503: dReg - DWI 4-label_1_label_3 06 | original | glcm | Imc2 | 0,982344167465 | 0,996646149 |
| 503: dReg - DWI 4-label_1_label_3 06 | original | glcm | Imc1 | -0,580811790128 | -0,780314991 |
| 503: dReg - DWI 4-label_1_label_3 06 | original | glcm | DifferenceAverage | 3,53320707071 | 7,038194444 |
| 503: dReg - DWI 4-label_1_label_3 06 | original | glcm | Id | 0,318818091631 | 0,232219347 |
| 503: dReg - DWI 4-label_1_label_3 06 | original | glcm | ClusterTendency | 19,3743979568 | 93,76417447 |
| 503: dReg - DWI 4-label_1_label_3 06 | original | glrlm | ShortRunLowGrayLevelEmphasis | 0,133197362055 | 0,098089102 |
| 503: dReg - DWI 4-label_1_label_3 06 | original | glrlm | GrayLevelVariance | 10,3920659722 | 46,69713803 |
| 503: dReg - DWI 4-label_1_label_3 06 | original | glrlm | LowGrayLevelRunEmphasis | 0,146825834277 | 0,098331268 |
| 503: dReg - DWI 4-label_1_label_3 06 | original | glrlm | GrayLevelNonUniformityNormalized | 0,147109375 | 0,109376887 |
| 503: dReg - DWI 4-label_1_label_3 06 | original | glrlm | RunVariance | 0,0466666666667 | 0,035502959 |
| 503: dReg - DWI 4-label_1_label_3 06 | original | glrlm | GrayLevelNonUniformity | 2,24375 | 1,478021978 |
| 503: dReg - DWI 4-label_1_label_3 06 | original | glrlm | LongRunEmphasis | 1,15 | 1,115384615 |
| 503: dReg - DWI 4-label_1_label_3 06 | original | glrlm | ShortRunHighGrayLevelEmphasis | 45,5729166667 | 204,6634615 |
| 503: dReg - DWI 4-label_1_label_3 06 | original | glrlm | RunLengthNonUniformity | 13,85 | 12,57692308 |
| 503: dReg - DWI 4-label_1_label_3 06 | original | glrlm | ShortRunEmphasis | 0,9625 | 0,971153846 |
| 503: dReg - DWI 4-label_1_label_3 06 | original | glrlm | LongRunHighGrayLevelEmphasis | 48,8854166667 | 226,7307692 |
| 503: dReg - DWI 4-label_1_label_3 06 | original | glrlm | RunPercentage | 0,953125 | 0,964285714 |

| | | | | | |
|--------------------------------------|----------|-------|----------------------------------|----------------|-------------|
| 503: dReg - DWI 4-label_1_label_3 06 | original | glrlm | LongRunLowGrayLevelEmphasis | 0,201339723166 | 0,099299929 |
| 503: dReg - DWI 4-label_1_label_3 06 | original | glrlm | RunEntropy | 3,04320991275 | 3,382749655 |
| 503: dReg - DWI 4-label_1_label_3 06 | original | glrlm | HighGrayLevelRunEmphasis | 46,2354166667 | 209,0769231 |
| 503: dReg - DWI 4-label_1_label_3 06 | original | glrlm | RunLengthNonUniformityNormalized | 0,906666666667 | 0,928994083 |
| 503: dReg - DWI 4-label_1_label_3 06 | original | glszm | GrayLevelVariance | 10,3905325444 | 51,30555556 |
| 503: dReg - DWI 4-label_1_label_3 06 | original | glszm | SmallAreaHighGrayLevelEmphasis | 48,0961538462 | 196,875 |
| 503: dReg - DWI 4-label_1_label_3 06 | original | glszm | GrayLevelNonUniformityNormalized | 0,136094674556 | 0,097222222 |
| 503: dReg - DWI 4-label_1_label_3 06 | original | glszm | SizeZoneNonUniformityNormalized | 0,644970414201 | 0,722222222 |
| 503: dReg - DWI 4-label_1_label_3 06 | original | glszm | SizeZoneNonUniformity | 8,38461538462 | 8,666666667 |
| 503: dReg - DWI 4-label_1_label_3 06 | original | glszm | GrayLevelNonUniformity | 1,76923076923 | 1,166666667 |
| 503: dReg - DWI 4-label_1_label_3 06 | original | glszm | LargeAreaEmphasis | 1,69230769231 | 1,5 |
| 503: dReg - DWI 4-label_1_label_3 06 | original | glszm | ZoneVariance | 0,177514792899 | 0,138888889 |
| 503: dReg - DWI 4-label_1_label_3 06 | original | glszm | ZonePercentage | 0,8125 | 0,857142857 |
| 503: dReg - DWI 4-label_1_label_3 06 | original | glszm | LargeAreaLowGrayLevelEmphasis | 0,361138272712 | 0,113632034 |
| 503: dReg - DWI 4-label_1_label_3 06 | original | glszm | LargeAreaHighGrayLevelEmphasis | 63,3846153846 | 292,5 |
| 503: dReg - DWI 4-label_1_label_3 06 | original | glszm | HighGrayLevelZoneEmphasis | 51,1538461538 | 216 |
| 503: dReg - DWI 4-label_1_label_3 06 | original | glszm | SmallAreaEmphasis | 0,826923076923 | 0,875 |
| 503: dReg - DWI 4-label_1_label_3 06 | original | glszm | LowGrayLevelZoneEmphasis | 0,109535708609 | 0,109434503 |

| | | | | | |
|--------------------------------------|----------|-------|-------------------------------|-----------------|-------------|
| 503: dReg - DWI 4-label_1_label_3 06 | original | glszm | ZoneEntropy | 3,39274741045 | 3,584962501 |
| 503: dReg - DWI 4-label_1_label_3 06 | original | glszm | SmallAreaLowGrayLevelEmphasis | 0,0466350675834 | 0,10838512 |

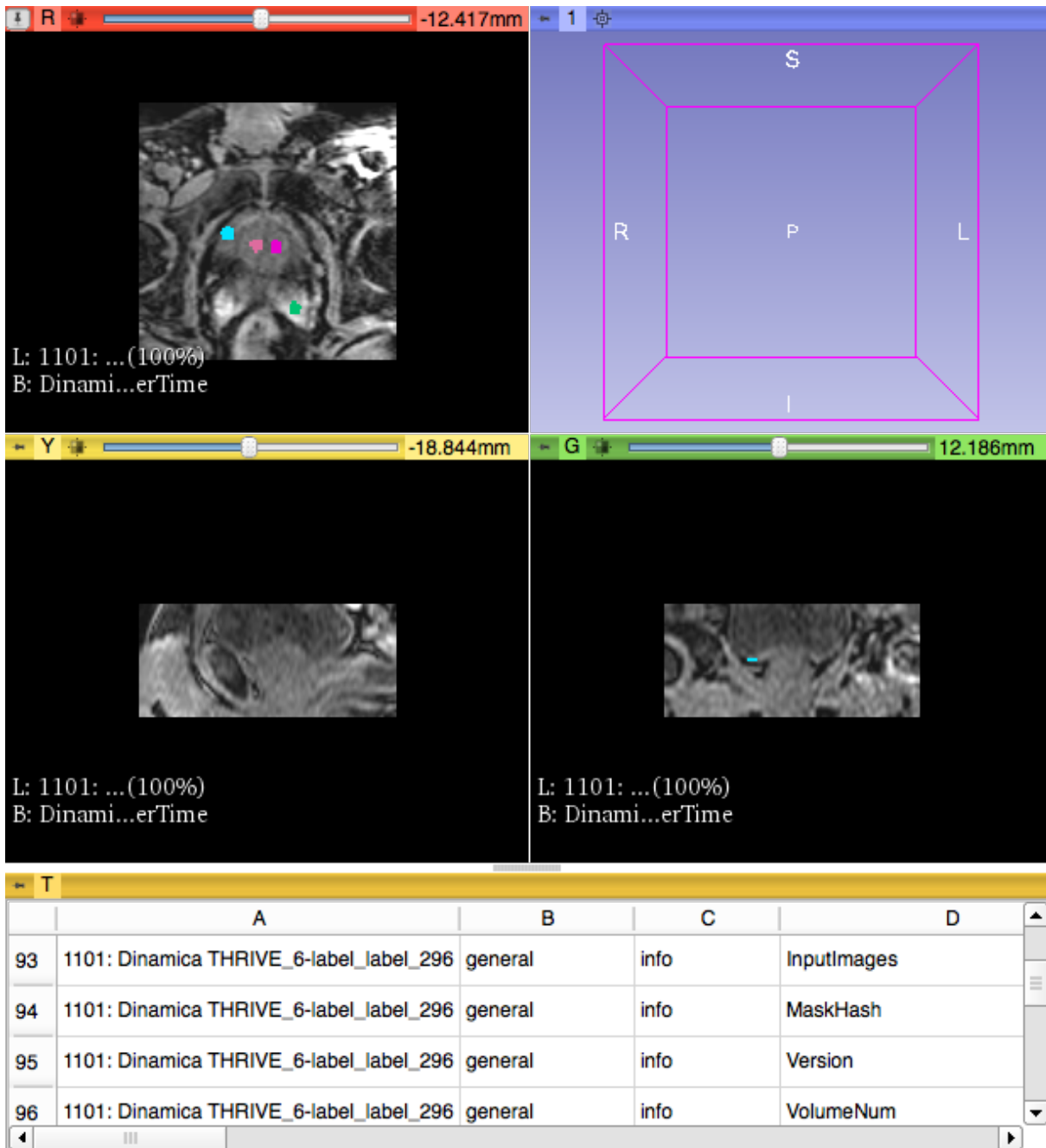


Fig. 20 - Example of 3D Slicer radiomic results for a DCE image. Images show the selected ROIs and the table (exported entirely below) with the results.

In Tab. 3 are reported some features (87) extracted from the DCE image shown above (Fig. 20).

Tab. 3: examples of 87 radiomic features extracted from the DCE image shown above (Fig. 20). 4 ROIs have been selected.

| | | | | Region 1 | Region 2 | Region 3 | Region 4 |
|---|------------------|---------------|-----------------|---|---|---|---|
| Label | Input image type | Feature Class | Feature Name | Value | | | |
| 1101: Dina mica THRI VE_6-label_1abel_303 | general | info | BoundingBox | (49, 51, 20, 4, 5, 1) | (56, 74, 20, 5, 5, 1) | (41, 51, 20, 5, 5, 1) | (30, 46, 20, 5, 5, 1) |
| 1101: Dina mica THRI VE_6-label_1abel_303 | general | info | GeneralSettings | {'distances': [1], 'additionalInfo': True, 'enableCExtensions': True, 'force2D': False, 'interpolator': 'sitkBSpline', 'resampledPixelSpacing': None, 'label': 1, 'normalizeScale': 1, 'normalize': False, 'force2Ddimension': 0, 'removeOutliers': None, 'minimumROISize': None, 'binWidth': 25, 'minimumROIDimensions': 1, 'symmetricalGLCM': True, 'padDistance': 5} | {'distances': [1], 'additionalInfo': True, 'enableCExtensions': True, 'force2D': False, 'interpolator': 'sitkBSpline', 'resampledPixelSpacing': None, 'label': 1, 'normalizeScale': 1, 'normalize': False, 'force2Ddimension': 0, 'removeOutliers': None, 'minimumROISize': None, 'binWidth': 25, 'minimumROIDimensions': 1, 'symmetricalGLCM': True, 'padDistance': 5} | {'distances': [1], 'additionalInfo': True, 'enableCExtensions': True, 'force2D': False, 'interpolator': 'sitkBSpline', 'resampledPixelSpacing': None, 'label': 1, 'normalizeScale': 1, 'normalize': False, 'force2Ddimension': 0, 'removeOutliers': None, 'minimumROISize': None, 'binWidth': 25, 'minimumROIDimensions': 1, 'symmetricalGLCM': True, 'padDistance': 5} | {'distances': [1], 'additionalInfo': True, 'enableCExtensions': True, 'force2D': False, 'interpolator': 'sitkBSpline', 'resampledPixelSpacing': None, 'label': 1, 'normalizeScale': 1, 'normalize': False, 'force2Ddimension': 0, 'removeOutliers': None, 'minimumROISize': None, 'binWidth': 25, 'minimumROIDimensions': 1, 'symmetricalGLCM': True, 'padDistance': 5} |
| 1101: Dina mica THRI VE_6-label_1abel_303 | general | info | Image Hash | 346484657c1f15944b6d105a56e70bfd025313a8 | 346484657c1f15944b6d105a56e70bfd025313a8 | 346484657c1f15944b6d105a56e70bfd025313a8 | 346484657c1f15944b6d105a56e70bfd025313a8 |
| 1101: Dina mica THRI VE_6-label_1abel_303 | general | info | Image Spacing | (1,8750000000000002, 1,8749999999999998, 1,9999972581863399) | (1,8750000000000002, 1,8749999999999998, 1,9999972581863399) | (1,8750000000000002, 1,8749999999999998, 1,9999972581863399) | (1,8750000000000002, 1,8749999999999998, 1,9999972581863399) |
| 1101: Dina mica THRI VE_6-label_1abel_303 | general | info | InputImages | {'Original': {}} | {'Original': {}} | {'Original': {}} | {'Original': {}} |
| 1101: Dina mica THRI VE_6-label_1abel_303 | general | info | Mask Hash | a880afa280c501e7765b73f5481e784c5b3d6407 | 528188333dcf84018448a7266db9070f14df9be1 | 8c02ee635d4de9a1d54a0901ddf455fd76db7764 | 19e8f43dc51b3769d182e7d7b2b51ff0b7e0d42b |

| 1101: Dinamica THRIVE_6-label_label_303 | general | info | Version | 1,2,0,post13+gcb9c73b | 1,2,0,post13+gcb9c73b | 1,2,0,post13+gcb9c73b | 1,2,0,post13+gcb9c73b |
|---|----------|------------|-----------------------------|-----------------------|-----------------------|-----------------------|-----------------------|
| 1101: Dinamica THRIVE_6-label_label_303 | general | info | VolumeNum | 1 | 1 | 1 | 1 |
| 1101: Dinamica THRIVE_6-label_label_303 | general | info | VoxelNum | 18 | 19 | 19 | 19 |
| 1101: Dinamica THRIVE_6-label_label_303 | original | firstorder | InterquartileRange | 27,971059 | 75,080211 | 44,16483 | 42,692669 |
| 1101: Dinamica THRIVE_6-label_label_303 | original | firstorder | Skewness | 0,477929325 | 0,117941287 | -0,266901321 | -1,09023363 |
| 1101: Dinamica THRIVE_6-label_label_303 | original | firstorder | Uniformity | 0,265432099 | 0,191135734 | 0,274238227 | 0,185595568 |
| 1101: Dinamica THRIVE_6-label_label_303 | original | firstorder | MeanAbsoluteDeviation | 25,48110768 | 54,71055949 | 24,4354258 | 35,65810466 |
| 1101: Dinamica THRIVE_6-label_label_303 | original | firstorder | Energy | 2097463,633 | 8529894,075 | 2439196,876 | 2095877,2 |
| 1101: Dinamica THRIVE_6-label_label_303 | original | firstorder | RobustMeanAbsoluteDeviation | 16,64523371 | 36,03850128 | 20,66119383 | 21,0944314 |
| 1101: Dinamica THRIVE_6-label_label_303 | original | firstorder | Median | 334,180547 | 680,138382 | 365,095928 | 332,708386 |
| 1101: Dinamica THRIVE_6-label_label_303 | original | firstorder | TotalEnergy | 14747770,95 | 59975735,5 | 17150579,52 | 14736616,36 |
| 1101: Dinamica THRIVE_6-label_label_303 | original | firstorder | Maximum | 421,038046 | 830,298804 | 397,48347 | 409,260758 |
| 1101: Dinamica THRIVE_6-label_label_303 | original | firstorder | RootMeanSquared | 341,3586931 | 670,0311884 | 358,2998506 | 332,1284786 |
| 1101: Dinamica THRIVE_6-label_label_303 | original | firstorder | 90Percentile | 377,1676482 | 732,5473136 | 397,48347 | 372,7511652 |
| 1101: Dinamica THRIVE_6-label_label_303 | original | firstorder | Minimum | 276,766268 | 529,97796 | 297,376522 | 191,38093 |
| 1101: Dinamica THRIVE_6-label_label_303 | original | firstorder | Entropy | 2,169035422 | 2,792586226 | 2,004285909 | 2,6703397 |
| 1101: Dinamica THRIVE_6-label_label_303 | original | firstorder | StandardDeviation | 33,1828397 | 70,17163406 | 28,14469395 | 48,79629212 |
| 1101: Dinamica THRIVE_6-label_label_303 | original | firstorder | Range | 144,271778 | 300,320844 | 100,106948 | 217,879828 |
| 1101: Dinamica THRIVE_6-label_label_303 | original | firstorder | Variance | 1101,10085 | 4924,058226 | 792,1237974 | 2381,078124 |
| 1101: Dinamica THRIVE_6-label_label_303 | original | firstorder | 10Percentile | 300,320844 | 569,4318748 | 325,6420132 | 273,821946 |
| 1101: Dinamica THRIVE_6-label_label_303 | original | firstorder | Kurtosis | 3,373453962 | 3,066541125 | 2,158731525 | 4,255558918 |
| 1101: Dinamica THRIVE_6-label_label_303 | original | firstorder | Mean | 339,7420441 | 666,3465579 | 357,1927479 | 328,5243495 |
| 1101: Dinamica THRIVE_6-label_label_303 | original | glcm | SumVariance | 3,202170956 | 14,91425737 | 2,794182256 | 6,733808107 |

| | | | | | | | |
|---|----------|------|--------------------|--------------|--------------|--------------|--------------|
| 1101: Dinamica THRIVE_6-label_label_303 | original | glcm | Homogeneity1 | 0,645591908 | 0,478443878 | 0,584077381 | 0,463612528 |
| 1101: Dinamica THRIVE_6-label_label_303 | original | glcm | Homogeneity2 | 0,609453782 | 0,407655547 | 0,55327381 | 0,390300429 |
| 1101: Dinamica THRIVE_6-label_label_303 | original | glcm | ClusterShade | 2,025876676 | 5,607932459 | -2,850840386 | -19,91736432 |
| 1101: Dinamica THRIVE_6-label_label_303 | original | glcm | MaximumProbability | 0,247627373 | 0,175595238 | 0,171130952 | 0,136904762 |
| 1101: Dinamica THRIVE_6-label_label_303 | original | glcm | Idmn | 0,95704667 | 0,962109509 | 0,943749814 | 0,948715538 |
| 1101: Dinamica THRIVE_6-label_label_303 | original | glcm | Contrast | 1,796953047 | 7,220238095 | 1,62202381 | 5,955357143 |
| 1101: Dinamica THRIVE_6-label_label_303 | original | glcm | DifferenceEntropy | 1,511652283 | 2,361802854 | 1,439460167 | 2,151272621 |
| 1101: Dinamica THRIVE_6-label_label_303 | original | glcm | InverseVariance | 0,402453449 | 0,337476025 | 0,574983466 | 0,374370866 |
| 1101: Dinamica THRIVE_6-label_label_303 | original | glcm | Dissimilarity | 0,945054945 | 2,011904762 | 1,014880952 | 1,907738095 |
| 1101: Dinamica THRIVE_6-label_label_303 | original | glcm | SumAverage | 6,656093906 | 12,55357143 | 7,413690476 | 13,9672619 |
| 1101: Dinamica THRIVE_6-label_label_303 | original | glcm | DifferenceVariance | 0,8837329 | 3,020975057 | 0,577770692 | 2,229981576 |
| 1101: Dinamica THRIVE_6-label_label_303 | original | glcm | Idn | 0,878960028 | 0,877331463 | 0,844618056 | 0,852672501 |
| 1101: Dinamica THRIVE_6-label_label_303 | original | glcm | Idm | 0,609453782 | 0,407655547 | 0,55327381 | 0,390300429 |
| 1101: Dinamica THRIVE_6-label_label_303 | original | glcm | Correlation | 0,277063767 | 0,355570357 | 0,262850596 | 0,073098981 |
| 1101: Dinamica THRIVE_6-label_label_303 | original | glcm | Autocorrelation | 11,43494006 | 41,37202381 | 14,03869048 | 48,97619048 |
| 1101: Dinamica THRIVE_6-label_label_303 | original | glcm | SumEntropy | 2,332883181 | 2,91380101 | 2,364188611 | 2,681658153 |
| 1101: Dinamica THRIVE_6-label_label_303 | original | glcm | AverageIntensity | 3,328046953 | 6,276785714 | 3,706845238 | 6,983630952 |
| 1101: Dinamica THRIVE_6-label_label_303 | original | glcm | Energy | 0,125152414 | 0,079294218 | 0,106646825 | 0,066663124 |
| 1101: Dinamica THRIVE_6-label_label_303 | original | glcm | SumSquares | 1,249781001 | 5,533623866 | 1,104051516 | 3,172291312 |
| 1101: Dinamica THRIVE_6-label_label_303 | original | glcm | ClusterProminence | 25,47518381 | 685,8977251 | 20,56560886 | 227,0939774 |
| 1101: Dinamica THRIVE_6-label_label_303 | original | glcm | Entropy | 3,384031629 | 3,951090668 | 3,448286932 | 4,097944426 |
| 1101: Dinamica THRIVE_6-label_label_303 | original | glcm | Imc2 | 0,901184521 | 0,956435924 | 0,761634898 | 0,928180242 |
| 1101: Dinamica THRIVE_6-label_label_303 | original | glcm | Imc1 | -0,410359772 | -0,479122947 | -0,240546181 | -0,427250569 |
| 1101: Dinamica THRIVE_6-label_label_303 | original | glcm | DifferenceAverage | 0,945054945 | 2,011904762 | 1,014880952 | 1,907738095 |

| | | | | | | | |
|---|----------|-------|----------------------------------|-------------|-------------|-------------|-------------|
| 1101: Dinamica THRIVE_6-label_label_303 | original | glcm | Id | 0,645591908 | 0,478443878 | 0,584077381 | 0,463612528 |
| 1101: Dinamica THRIVE_6-label_label_303 | original | glcm | ClusterTendency | 3,202170956 | 14,91425737 | 2,794182256 | 6,733808107 |
| 1101: Dinamica THRIVE_6-label_label_303 | original | glrlm | ShortRunLowGrayLevelEmphasis | 0,158175879 | 0,111156477 | 0,130540216 | 0,081322008 |
| 1101: Dinamica THRIVE_6-label_label_303 | original | glrlm | GrayLevelVariance | 1,675974277 | 8,839533938 | 1,278288567 | 4,154195502 |
| 1101: Dinamica THRIVE_6-label_label_303 | original | glrlm | LowGrayLevelRunEmphasis | 0,182757123 | 0,114141614 | 0,142585841 | 0,082936244 |
| 1101: Dinamica THRIVE_6-label_label_303 | original | glrlm | GrayLevelNonUniformityNormalized | 0,2239119 | 0,155536963 | 0,264323202 | 0,171638462 |
| 1101: Dinamica THRIVE_6-label_label_303 | original | glrlm | RunVariance | 0,339432939 | 0,201623039 | 0,189880875 | 0,145352373 |
| 1101: Dinamica THRIVE_6-label_label_303 | original | glrlm | GrayLevelNonUniformity | 2,973076923 | 2,529779412 | 4,174145299 | 2,876838235 |
| 1101: Dinamica THRIVE_6-label_label_303 | original | glrlm | LongRunEmphases | 2,220512821 | 1,579840686 | 1,707532051 | 1,434742647 |
| 1101: Dinamica THRIVE_6-label_label_303 | original | glrlm | ShortRunHighGrayLevelEmphasis | 9,805288462 | 41,25833674 | 12,34922543 | 41,89922896 |
| 1101: Dinamica THRIVE_6-label_label_303 | original | glrlm | RunLengthNonUniformity | 7,425 | 12,41164216 | 11,14797009 | 13,29595588 |
| 1101: Dinamica THRIVE_6-label_label_303 | original | glrlm | ShortRunEmphasis | 0,760754986 | 0,889898216 | 0,844484509 | 0,907654208 |
| 1101: Dinamica THRIVE_6-label_label_303 | original | glrlm | LongRunHighGrayLevelEmphasis | 25,55608974 | 71,63192402 | 24,97542735 | 71,96599265 |
| 1101: Dinamica THRIVE_6-label_label_303 | original | glrlm | RunPercentage | 0,736111111 | 0,855263158 | 0,828947368 | 0,881578947 |
| 1101: Dinamica THRIVE_6-label_label_303 | original | glrlm | LongRunLowGrayLevelEmphasis | 0,310363515 | 0,128927744 | 0,200265017 | 0,090727055 |
| 1101: Dinamica THRIVE_6-label_label_303 | original | glrlm | RunEntropy | 2,974652159 | 3,235547862 | 2,662868065 | 3,016363978 |
| 1101: Dinamica THRIVE_6-label_label_303 | original | glrlm | HighGrayLevelRunEmphasis | 12,48108974 | 45,96660539 | 14,72061966 | 47,27205882 |
| 1101: Dinamica THRIVE_6-label_label_303 | original | glrlm | RunLengthNonUniformityNormalized | 0,553814103 | 0,759798905 | 0,691244167 | 0,792340236 |
| 1101: Dinamica THRIVE_6-label_label_303 | original | glszm | GrayLevelVariance | 2,484375 | 12,36363636 | 1,734375 | 5,354166667 |
| 1101: Dinamica THRIVE_6-label_label_303 | original | glszm | SmallAreaHighGrayLevelEmphasis | 10,52295918 | 41,20454545 | 6,376875 | 35,49666667 |
| 1101: Dinamica THRIVE_6-label_label_303 | original | glszm | GrayLevelNonUniformityNormalized | 0,1875 | 0,123966942 | 0,21875 | 0,152777778 |
| 1101: Dinamica THRIVE_6-label_label_303 | original | glszm | SizeZoneNonUniformityNormalized | 0,4375 | 0,570247934 | 0,34375 | 0,708333333 |
| 1101: Dinamica THRIVE_6-label_label_303 | original | glszm | SizeZoneNonUniformity | 3,5 | 6,272727273 | 2,75 | 8,5 |
| 1101: Dinamica THRIVE_6-label_label_303 | original | glszm | GrayLevelNonUniformity | 1,5 | 1,363636364 | 1,75 | 1,833333333 |

| | | | | | | | |
|---|----------|-------|--------------------------------|--------------|-------------|-------------|-------------|
| 1101: Dinamica THRIVE_6-label_label_303 | original | glszm | LargeAreaEmphasis | 9,25 | 5,909090909 | 8,125 | 4,25 |
| 1101: Dinamica THRIVE_6-label_label_303 | original | glszm | ZoneVariance | 4,1875 | 2,925619835 | 2,484375 | 1,743055556 |
| 1101: Dinamica THRIVE_6-label_label_303 | original | glszm | ZonePercentage | 0,4444444444 | 0,578947368 | 0,421052632 | 0,631578947 |
| 1101: Dinamica THRIVE_6-label_label_303 | original | glszm | LargeAreaLowGrayLevelEmphasis | 1,103090278 | 0,271358631 | 0,722152778 | 0,168667341 |
| 1101: Dinamica THRIVE_6-label_label_303 | original | glszm | LargeAreaHighGrayLevelEmphasis | 99,375 | 273,3636364 | 128,25 | 222,4166667 |
| 1101: Dinamica THRIVE_6-label_label_303 | original | glszm | HighGrayLevelZoneEmphasis | 13,875 | 48,36363636 | 13,125 | 44,41666667 |
| 1101: Dinamica THRIVE_6-label_label_303 | original | glszm | SmallAreaEmphasis | 0,66661352 | 0,77458256 | 0,551875 | 0,841875 |
| 1101: Dinamica THRIVE_6-label_label_303 | original | glszm | LowGrayLevelZoneEmphasis | 0,225486111 | 0,154350282 | 0,209652778 | 0,108319765 |
| 1101: Dinamica THRIVE_6-label_label_303 | original | glszm | ZoneEntropy | 3 | 3,095795255 | 3 | 3,022055209 |
| 1101: Dinamica THRIVE_6-label_label_303 | original | glszm | SmallAreaLowGrayLevelEmphasis | 0,18111895 | 0,145544221 | 0,174027778 | 0,105466408 |

Appendix 3. MpMRI phantoms for repeatability, reproducibility and robustness

Some examples of mpMRI phantoms developed at IFAC-CNR are shown Fig. 21.

These phantoms are used for quality assurance, repeatability, reproducibility and robustness test and retest. The same phantoms can be used for test of characteristics of nanoparticles as theranostics agents and for characterization of solutions, gels (Fig. 22, Fig. 23), etc.

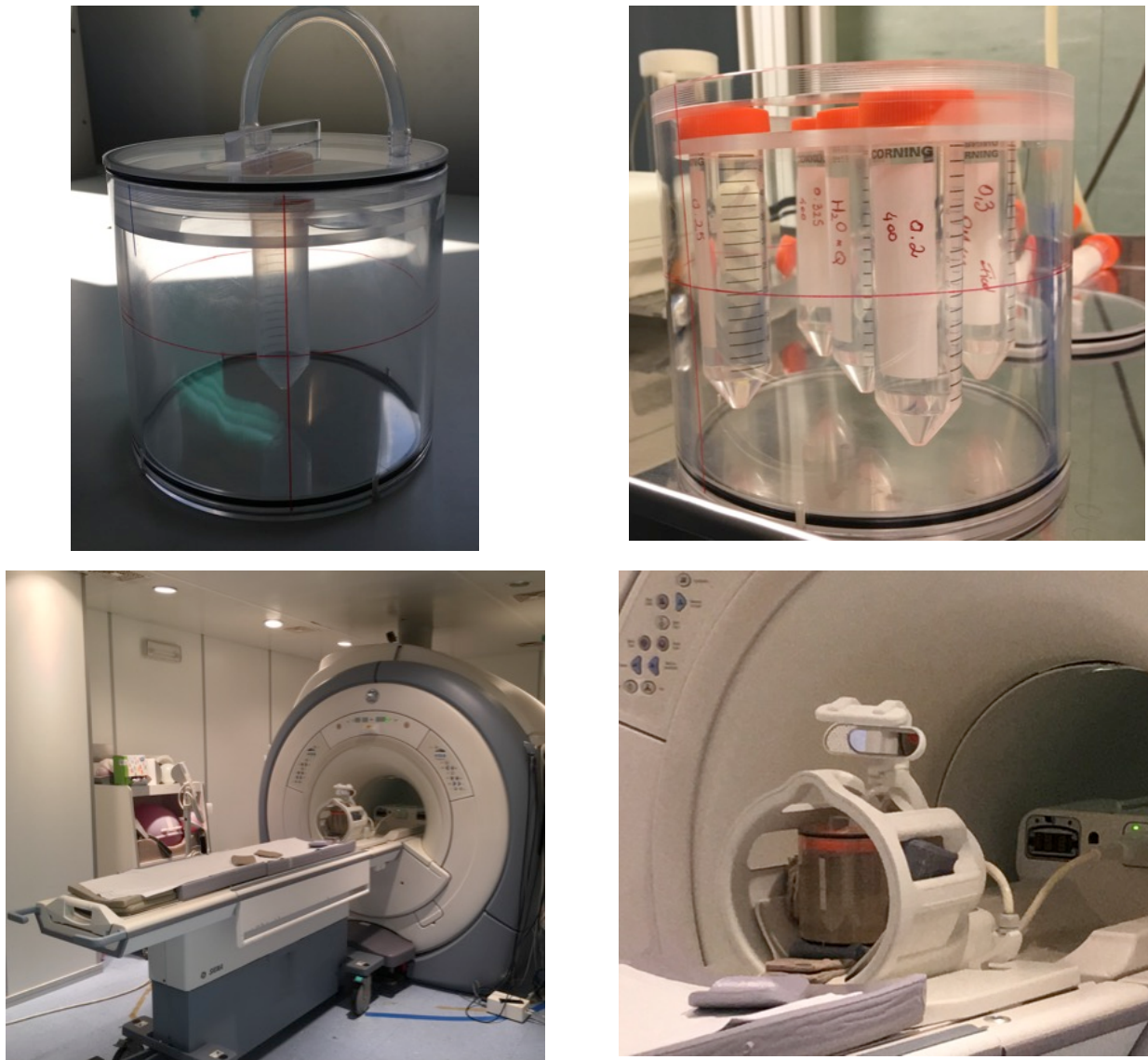


Fig. 21 - Examples of phantoms for multiparametric MRI studies. Top panel: phantom developed at IFAC-CNR for the study of nanoparticles in mpMRI. This kind of phantom is suitable for repeatability, reproducibility and robustness test. In the bottom panel the same phantom is shown during a mpMRI images acquisition using a head-coil at the 3T GE scanner of IFAC-CNR.

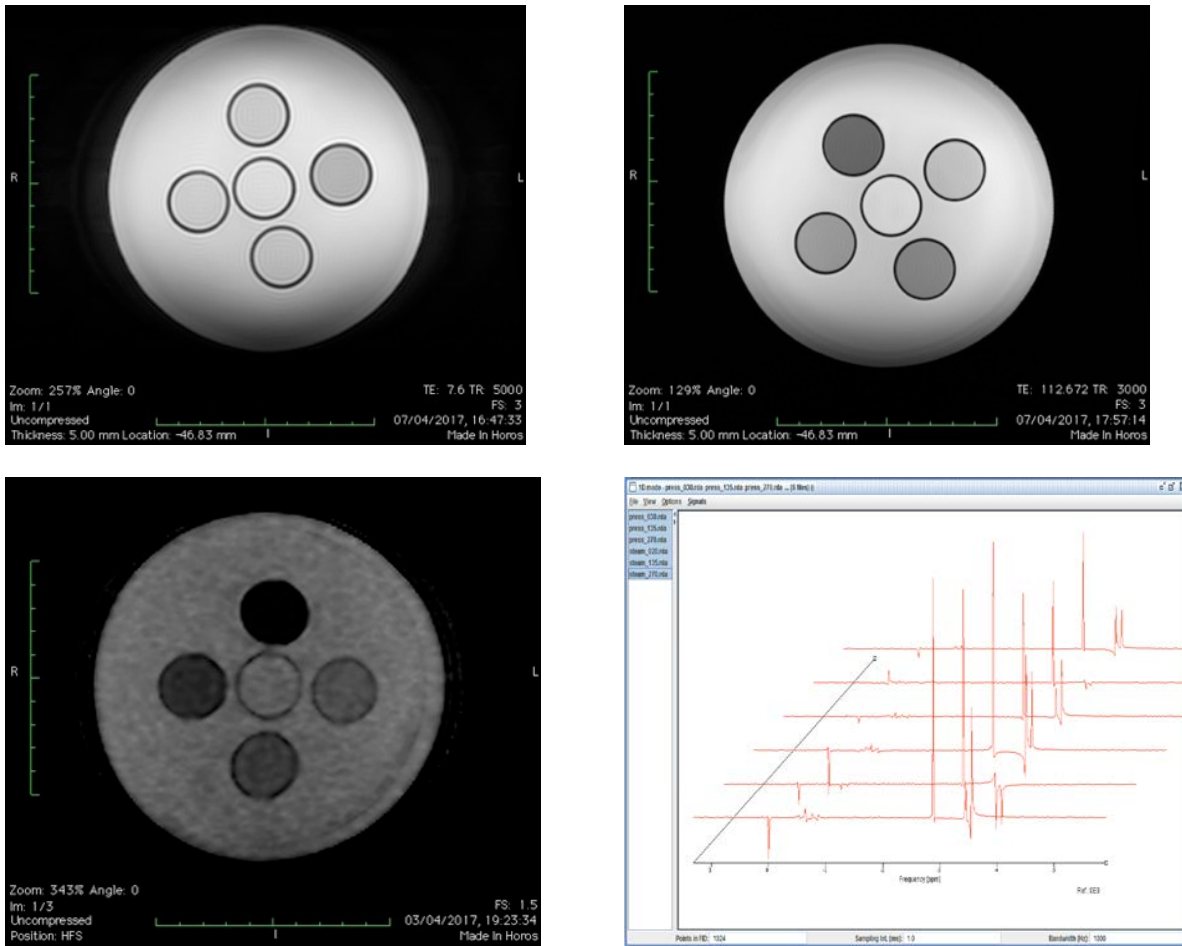


Fig. 22 - Examples of mpMRI acquisitions using the phantoms developed at IFAC-CNR. Top left: T1 map; Top right: T2w map; Bottom-left: DWI; Bottom-right: Spectroscopy. The first 3 images have been displayed using the software Horos (Horos Project, DICOM image viewing and measuring. <http://www.horosproject.org/>). The last image, corresponding to an example of magnetic resonance spectroscopy has been created using the software jMRUI.

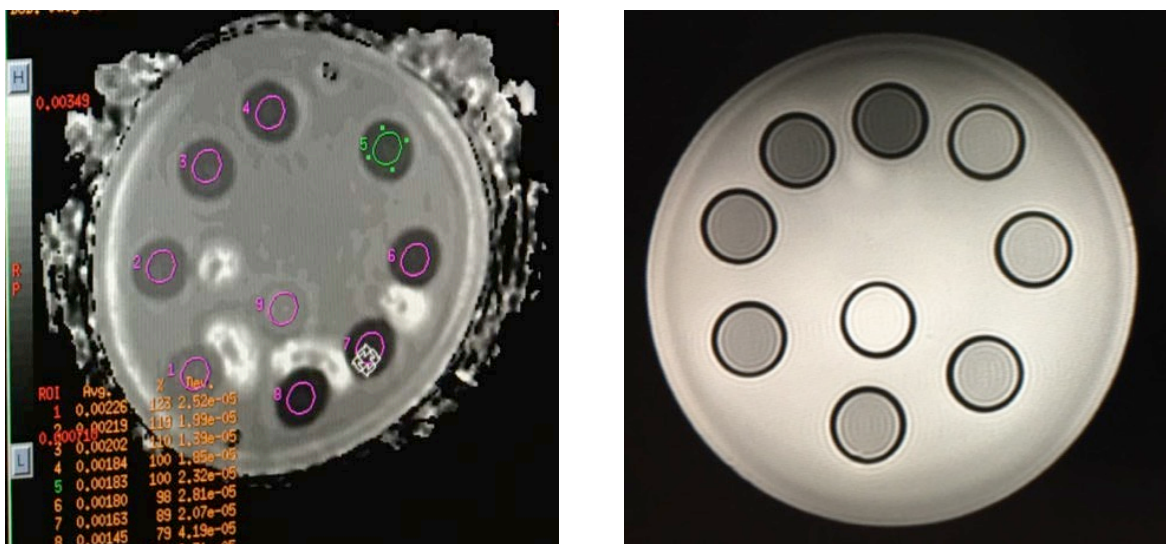


Fig. 23 - Examples of phantom data acquisition using mpMRI, scanner 3T GE at IFC-CNR. This phantom holds 9 test tubes with a gel inside at different concentrations. Left panel: ADC. Right panel: T2w. Visualization and elaboration of these images were performed using the GE software. The left ADC image shows some distortions typical of diffusion acquisition with scanner at 3T. 9 ROIs were selected on this image to evaluate the ADC inside the test tubes.

Appendix 4. Radiomics applications in ultrasound and photoacoustic imaging

Ultrasound imaging modality is largely spread as a diagnostic tool, then arise the question if Radiomics approach can be used in this context too.

To date no integrated analysis testing the repeatability and stability of ultrasound radiomic features for applications in oncology has been published [22].

However quantitative features retrieved from ultrasound images have been shown to be useful to discriminate among normal, malignant and benign tissues [110]. In Ref. [111] has been evaluated whether acoustical, textural and shape features were able to differentiate malignant melanoma from benign melanocytic tumors. Similar accuracies were observed when using quantitative (textural) features to identify malignant thyroid nodules [112, 113] or breast tumors [114, 115, 146].

In Ref. [123] texture analysis (first order statistics, GLCM and fractal dimension) was performed on breast ultrasound in a cohort of 80 patients [67, 123]. The authors were able to identify malignant lesions with a sensitivity of 100% and specificity of 80% (78% for fibroadenoma, 73% for cysts and 91% for fibrocystic nodules). Numerous studies have since used texture analysis to differentiate between benign and malignant breast lesions using ultrasound [123 - 127].

However in Ref. [116] a high inter-observer variability was revealed in quantitative ultrasound features of the Achilles tendons.

Our interest is mainly in the study of melanoma and sentinel lymph node [117 - 122], and we are developing and testing an integrated clinical platform of ultrasound and photoacoustic imaging. Images obtained will be analyzed using Radiomics approach, with in addition the possibility to study patterns coming from the injection of ultrasound and/or photoacoustical contrast agents.

Appendix 5. MpMRI phantoms for the IRINA project

The IRINA project (“Imaging molecolare di risonanza magnetica della biodistribuzione di nanoparticelle e vettori cellulari per applicazioni teranostiche” – Biodistribution of nanoparticles and cellular vehicles using biomolecular magnetic resonance imaging for theranostics applications) is aimed to the use of nanoparticles as a new theranostics agents.

In this context we use the potentiality of multiparametric magnetic resonance imaging to visualize the nanoparticles biodistribution inside the body.

As a preliminary test we have developed a phantom aimed to characterizes the behavior of different kinds of nanoparticles in mpMRI (parameters as T1, T2, ADC, etc. can be evaluated) (Fig. 24).

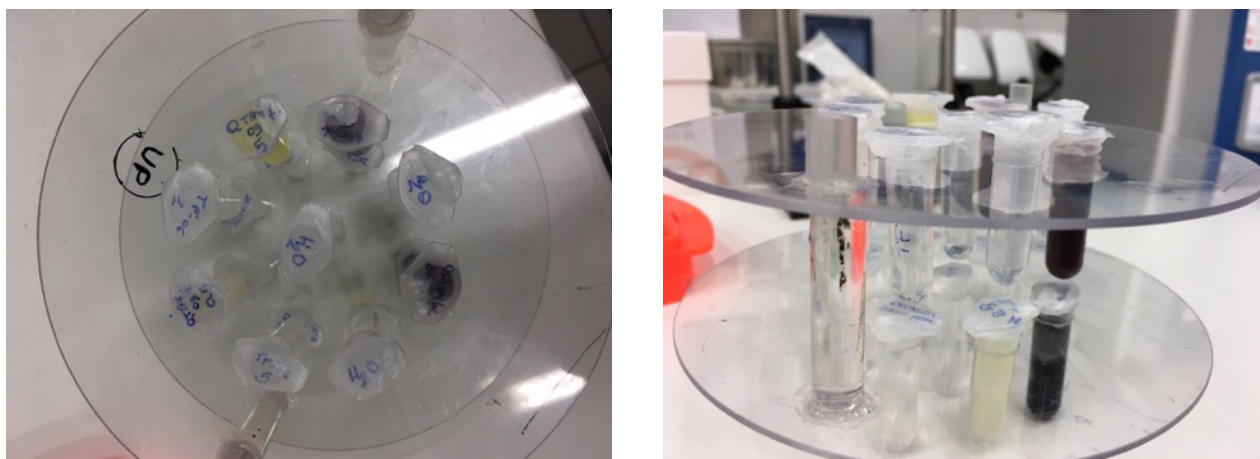


Fig. 24 - Examples of phantom developed at IFAC-CNR in the framework of IRINA project. This phantom holds 18 test tubes with a different types of nanoparticles all made and developed at IFAC-CNR. In this example we have 3 types: made of PMMA with a fluorescein tag, just PMMA, and made of gold (darker in the pictures above). Some water tubes have been inserted in order to check the measurements errors.

References

- [1]. Barucci, A., Carpi, R., Ciccarone, A., Esposito, M., Olmastroni, M., Zatelli, G., Magnetic Resonance Spectroscopy - Data Analysis for Clinical Applications, IFAC ebook series, ISBN 978-88-906859-9-6, data pubblicazione: 2016
- [2]. Barucci, A., Carpi, R., Esposito, M., Olmastroni, M., Zatelli, G., Diffusion-Weighted MR imaging: Clinical applications of kurtosis analysis to prostate cancer, IFAC-TSRR vol. 8 (2016) 67-78, ISSN 2035-5831;
- [3]. <https://www.slicer.org>
- [4]. Fedorov A., Beichel R., Kalpathy-Cramer J., Finet J., Fillion-Robin J-C., Pujol S., Bauer C., Jennings D., Fennessy F.M., Sonka M., Buatti J., Aylward S.R., Miller J.V., Pieper S., Kikinis R. 3D Slicer as an Image Computing Platform for the Quantitative Imaging Network. *Magn Reson Imaging*. 2012 Nov;30(9):1323-41. PMID: 22770690. PMCID: PMC3466397.
- [5]. Toivonen J, Merisaari H, Pesola M, Taimen P, Boström PJ, Pahikkala T, et al. Mathematical models for diffusion-weighted imaging of prostate cancer using b values up to 2000 s/mm²: Correlation with Gleason score and repeatability of region of interest analysis. *Magn Reson Med*. 2014; <http://onlinelibrary.wiley.com/doi/10.1002/mrm.25482/abstract>
- [6]. Kobus T., Fedorov A., Tempany C.M., Mulkern R.V., Dunne R., Maier S.E. Bi-exponential Diffusion Analysis in Normal Prostate and Prostate Cancer: Transition Zone and Peripheral Zone Considerations. *Proc. of ISMRM 2015*. <http://www.spl.harvard.edu/abstracts/item/view/168>
- [7]. Oshio K, Shinmoto H, Mulkern RV. Interpretation of diffusion MR imaging data using a gamma distribution model. *Magn Reson Med Sci*. 2014;13: 191–195. doi:10.2463/mrms.2014-0016
- [8]. Bennett KM, Schmainda KM, Bennett RT, Rowe DB, Lu H, Hyde JS. Characterization of continuously distributed cortical water diffusion rates with a stretched-exponential model. *Magn Reson Med*. 2003;50: 727–734. doi:10.1002/mrm.10581
- [9]. The Minitab Blog: Regression Analysis: How Do I Interpret R-squared and Assess the Goodness-of-Fit? <http://blog.minitab.com/blog/adventures-in-statistics/regression-analysis-how-do-i-interpret-r-squared-and-assess-the-goodness-of-fit>
- [10]. Knopp MV, Giesel FL, Marcos H et al: Dynamic contrast-enhanced magnetic resonance imaging in oncology. *Top Magn Reson Imaging*, 2001; 12:301-308.
- [11]. Rijpkema M, Kaanders JHAM, Joosten FBM et al: Method for quantitative mapping of dynamic MRI contrast agent uptake in human tumors. *J Magn Reson Imaging* 2001; 14:457-463.
- [12]. de Bazelaire, C.M., et al., MR imaging relaxation times of abdominal and pelvic tissues measured in vivo at 3.0 T: preliminary results. *Radiology*, 2004. 230(3): p. 652-9.
- [13]. Pintaske J, Martirosian P, Graf H, Erb G, Lodemann K-P, Claussen CD, Schick F. Relaxivity of Gadopentetate Dimeglumine (Magnevist), Gadobutrol (Gadovist), and Gadobenate Dimeglumine (MultiHance) in human blood plasma at 0.2, 1.5, and 3 Tesla. *Investigative radiology*. 2006 March;41(3):213–21.
- [14]. Parker GJ, Roberts C, Macdonald A, Buonaccorsi GA, Cheung S, Buckley DL, Jackson A, Watson Y, Davies K, Jayson GC. Experimentally-derived functional form for a population-averaged high-temporal-resolution arterial input function for dynamic contrast-enhanced MRI. *Magnetic Resonance in Medicine*, 2006 Nov; 56(5):993-1000.
- [15]. Huang, W., Li, X., Chen, Y., Li, X., Chang, M.-C., Oborski, M. J., ... Kalpathy-Cramer, J. (2014). Variations of dynamic contrast-enhanced magnetic resonance imaging in evaluation of breast cancer therapy response: a multicenter data analysis challenge. *Translational Oncology*, 7(1), 153–66. doi:10.1593/tlo.13838 <http://dx.doi.org/10.1593/tlo.13838>
- [16]. Tofts, P. S., Brix, G., Buckley, D. L., Evelhoch, J. L., Henderson, E., Knopp, M. V., ... Weisskoff, R. M. (1999). Estimating kinetic parameters from Contrast-Enhanced T₁-Weighted MRI of a Diffusible Tracer : Standardized Quantities and Symbols. *J Magn Reson Imaging*, 10(3), 223–232.
- [17]. Stoyanova, R., Pollack, A., Takhar, M., Lynne, C., Parra, N., Lam, L. L. C., ... Ishkanian, A. (2016). Association of multiparametric MRI quantitative imaging features with prostate cancer gene expression in MRI-targeted prostate biopsies. *Oncotarget*, 7(33), 53362–53376. <http://doi.org/10.18632/oncotarget.10523>

- [18]. Stoyanova R, Takhar M, Tschudi Y, Ford JC, Solórzano G, Erho N, Balagurunathan Y, Punnen S, Davicioni E, Gillies RJ, Pollack A. Prostate cancer radiomics and the promise of radiogenomics. *Transl Cancer Res* 2016;5(4):432-447. doi: 10.21037/tcr.2016.06.20
- [19]. <http://www.jmru.eu/welcome-to-the-new-mrui-website/>
- [20]. Michele Avanzo, Joseph Stancanello, Issam El Naqa, Beyond imaging: The promise of radiomics, *Physica Medica*, Volume 38, June 2017, Pages 122-139, ISSN 1120-1797, <https://doi.org/10.1016/j.ejmp.2017.05.071>.
- [21]. Napel S, Giger M. Special section guest editorial: radiomics and imaging genomics: quantitative imaging for precision medicine. *J Med Imaging (Bellingham)* 2015; 2:041001.
- [22]. Larue RT, Defraene G, De Ruysscher D, Lambin P, van Elmpt W. Quantitative radiomics studies for tissue characterization: a review of technology and methodological procedures. *Br J Radiol* 2017; 90:20160665.
- [23]. El Naqa I. Biomedical informatics and panomics for evidence-based radiation therapy. *Wiley Interdiscip Rev Data Mining Knowledge Discov* 2014; 4:327–40.
- [24]. Oberije C, Nalbantov G, Dekker A, Boersma L, Borger J, Reymen B, et al. A prospective study comparing the predictions of doctors versus models for treatment outcome of lung cancer patients: a step toward individualized care and shared decision making. *Radiother Oncol* 2014; 112:37–43.
- [25]. Cunliffe A, Armato 3rd SG, Castillo R, Pham N, Guerrero T, Al-Hallaq HA. Lung texture in serial thoracic computed tomography scans: correlation of radiomics-based features with radiation therapy dose and radiation pneumonitis development. *Int J Radiat Oncol Biol Phys* 2015; 91:1048–56.
- [26]. Carvalho S, Leijenaar RTH, Troost EGC, van Elmpt W, Muratet J, Denis F. Early variation of FDG-PET radiomics features in NSCLC is related to overall survival – the “delta radiomics” concept. *Radiother Oncol* 2016; 118:S20–1.
- [27]. van Timmeren JE, Leijenaar RTH, van Elmpt W, Lambin P. Can we replace high quality simulation CT by simple kVcone-beam CT images to extract an externally validated radiomics signature? *Radiother Oncol* 2016; 118:S107.
- [28]. Wibmer A, Hricak H, Gondo T, Matsumoto K, Veeraraghavan H, Fehr D, et al. Haralick texture analysis of prostate MRI: utility for differentiating non-cancerous prostate from prostate cancer and differentiating prostate cancers with different Gleason scores. *Eur Radiol* 2015; 25: 2840–50. doi: <https://doi.org/10.1007/s00330-015-3701-8>
- [29]. Gnep K, Fargeas A, Gutierrez-Carvajal RE, Commandeur F, Mathieu R, Ospina JD, et al. Haralick textural features on T2-weighted MRI are associated with biochemical recurrence following radiotherapy for peripheral zone prostate cancer. *J Magn Reson Imaging* 2017; 45; 103–17. doi: <https://doi.org/10.1002/jmri.25335>.
- [30]. Coroller TP, Grossmann P, Hou Y, Rios Velazquez E, Leijenaar RT, Hermann G, et al. CT-based radiomic signature predicts distant metastasis in lung adenocarcinoma. *Radiother Oncol* 2015; 114: 345–50. doi: <https://doi.org/10.1016/j.radonc.2015.02.015>
- [31]. Aerts HJ, Velazquez ER, Leijenaar RT, Parmar C, Grossmann P, Carvalho S, et al. Decoding tumour phenotype by noninvasive imaging using a quantitative radiomics approach. *Nat Commun* 2014; 5: 4006. doi: <https://doi.org/10.1038/ncomms5006>
- [32]. van Velden FH, Cheebsumon P, Yaqub M, Smit EF, Hoekstra OS, Lammertsma AA, et al. Evaluation of a cumulative SUV-volume histogram method for parameterizing heterogeneous intratumoural FDG uptake in non-small cell lung cancer PET studies. *Eur J Nucl Med Mol Imaging* 2011; 38: 1636–47. doi: <https://doi.org/10.1007/s00259-011-1845-6>
- [33]. Haralick RM, Shanmugam K, Dinstein I. Textural features for image classification. *IEEE Trans Syst Man Cyb* 1973; 3: 610–21. doi: <https://doi.org/10.1109/tsmc.1973.4309314>
- [34]. Amadasun M, King R. Textural features corresponding to textural properties. *IEEE Trans Syst Man Cyb* 1989; 19: 1264–74. doi: <https://doi.org/10.1109/21.44046>
- [35]. Sun C, Wee WG. Neighboring gray level dependence matrix for texture classification. *Comput Vision Graph* 1982; 23: 341–52. doi: [https://doi.org/10.1016/0734-189x\(83\)90032-4](https://doi.org/10.1016/0734-189x(83)90032-4)
- [36]. Galloway MM. Texture analysis using gray level run lengths. *Comput Vision Graph* 1975; 4: 172–9. doi: [https://doi.org/10.1016/s0146-664x\(75\)80008-6](https://doi.org/10.1016/s0146-664x(75)80008-6)
- [37]. Tixier F, Le Rest CC, Hatt M, Albarghach N, Pradier O, Metges JP, et al. Intratumor heterogeneity characterized by textural features on baseline 18F-FDG PET images predicts response to concomitant

- radioche- motherapy in esophageal cancer. *J Nucl Med* 2011; 52: 369–78. doi: <https://doi.org/10.2967/jnumed.110.082404>
- [38]. Vallieres M, Freeman CR, Skamene SR, El Naqa I. A radiomics model from joint FDG- PET and MRI texture features for the prediction of lung metastases in soft-tissue sarcomas of the extremities. *Phys Med Biol* 2015; 60: 5471–96. doi: <https://doi.org/10.1088/0031-9155/60/14/5471>
- [39]. Ganeshan B, Goh V, Mandeville HC, Ng QS, Hoskin PJ, Miles KA. Non-small cell lung cancer: histopathologic correlates for texture parameters at CT. *Radiology* 2013; 266: 326–36. doi: <https://doi.org/10.1148/radiol.12112428>
- [40]. Ng F, Kozarski R, Ganeshan B, Goh V. Assessment of tumor heterogeneity by CT texture analysis: can the largest cross- sectional area be used as an alternative to whole tumor analysis? *Eur J Radiol* 2013; 82: 342–8. doi: <https://doi.org/10.1016/j.ejrad.2012.10.023>
- [41]. Fave X, Cook M, Frederick A, Zhang L, Yang J, Fried D, et al. Preliminary investigation into sources of uncertainty in quantitative imaging features. *Comput Med Imaging Graph* 2015; 44: 54–61. doi: <https://doi.org/10.1016/j.compmedimag.2015.04.006>
- [42]. Kumar V, Gu Y, Basu S, Berglund A, Eschrich SA, Schabath MB, et al. Radiomics: the process and the challenges. *Magn Reson Imaging* 2012; 30: 1234–48. doi: <https://doi.org/10.1016/j.mri.2012.06.010>
- [43]. Zhang L, Fried DV, Fave XJ, Hunter LA, Yang J, Court LE. IBEX: an open infrastructure software platform to facilitate collaborative work in radiomics. *Med Phys* 2015; 42: 1341–53. doi: <https://doi.org/10.1118/1.4908210>
- [44]. Ganeshan B, Miles KA. Quantifying tumour heterogeneity with CT. *Cancer Imaging* 2013; 13: 140–9. doi: <https://doi.org/10.1102/1470-7330.2013.0015>
- [45]. Panth KM, Leijenaar RT, Carvalho S, Lieuwes NG, Yaromina A, Dubois L, et al. Is there a causal relationship between genetic changes and radiomics-based image features? An in vivo preclinical experiment with doxycy- cline inducible GADD34 tumor cells. *Radio- ther Oncol* 2015; 116: 462–6. doi: <https://doi.org/10.1016/j.radonc.2015.06.013>
- [46]. Segal E, Sirlin CB, Ooi C, Adler AS, Gollub J, Chen X, et al. Decoding global gene expression programs in liver cancer by noninvasive imaging. *Nat Biotechnol* 2007; 25: 675–80. doi: <https://doi.org/10.1038/nbt1306>
- [47]. Stephen S F Yip and Hugo J W L Aerts, Applications and limitations of radiomics, *Phys. Med. Biol.* 61 (2016) R150–166, doi:10.1088/0031-9155/61/13/R150
- [48]. Ueno, Y., Tamada, T., Bist, V., Reinhold, C., Miyake, H., Tanaka, U., Kitajima, K., Sugimura, K. and Takahashi, S. (2016), Multiparametric magnetic resonance imaging: Current role in prostate cancer management. *Int. J. Urol.*, 23: 550–557. doi:10.1111/iju.13119
- [49]. Dominietto M., Rudin M., Could magnetic resonance provide in vivo histology?, *Front. Genet.*, 13 January 2014 | <https://doi.org/10.3389/fgene.2013.00298>
- [50]. Hegde, J. V., Mulkern, R. V., Panych, L. P., Fennessy, F. M., Fedorov, A., Maier, S. E. and Tempany, C. M.C. (2013), Multiparametric MRI of prostate cancer: An update on state-of-the-art techniques and their performance in detecting and localizing prostate cancer. *J. Magn. Reson. Imaging*, 37: 1035–1054. doi:10.1002/jmri.23860
- [51]. Xenia Fave et al., Delta-radiomics features for the prediction of patient outcomes in non-small cell lung cancer, *Scientific Reports* 7, Article number: 588 (2017), doi:10.1038/s41598-017-00665-z
- [52]. Chintan Parmar, Patrick Grossmann, Johan Bussink, Philippe Lambin & Hugo J. W. L. Aerts, Machine Learning methods for Quantitative Radiomic Biomarkers, *Scientific Reports* | 5:13087 | doi: 10.1038/srep13087 1
- [53]. Laurence E. Court and Xenia Fave and Dennis Mackin and Joonsang Lee and Jinzhong Yang and Lifei Zhang, Computational resources for radiomics, *Translational Cancer Research*, vol. 5(4), 2016, doi: 10.21037/tcr.2016.06.17
- [54]. Chalkidou A, O'Doherty MJ, Marsden PK. False Discovery Rates in PET and CT Studies with Texture Features: A Systematic Review. *PLoS One* 2015;10:e0124165., <http://dx.doi.org/10.1371/journal.pone.0124165>
- [55]. Johansen R, Jensen L R, Rydland J, Goa P E, Kvistad K A, Bathen T F, Axelson D E, Lundgren S and Gribbestad I S, 2009, Predicting survival and early clinical response to primary chemotherapy for patients with locally advanced breast cancer using DCE-MRI *J. Magn. Reson. Imaging* 29 1300–7
- [56]. Hye Jin Baek, Ho Sung Kim, Namkug Kim, Young Jun Choi, and Young Joong Kim, Percent Change of

Perfusion Skewness and Kurtosis: A Potential Imaging Biomarker for Early Treatment Response in Patients with Newly Diagnosed Glioblastomas, *Radiology* 2012 264:3, 834-843

- [57]. Shukla-Dave A et al 2012 Dynamic contrast-enhanced magnetic resonance imaging as a predictor of outcome in head-and-neck squamous cell carcinoma patients with nodal metastases *Int. J. Radiat. Oncol. Biol. Phys.* 82 1837–44
- [58]. King A D, Chow K-K, Yu K-H, Mo F K F, Yeung D K W, Yuan J, Bhatia K S, Vlantis A C and Ahuja A T 2013 Head and neck squamous cell carcinoma: diagnostic performance of diffusion-weighted MR imaging for the prediction of treatment response *Radiology* 266 531–8
- [59]. Peng S-L, Chen C-F, Liu H-L, Lui C-C, Huang Y-J, Lee T-H, Chang C-C and Wang F-N 2013 Analysis of parametric histogram from dynamic contrast-enhanced MRI: application in evaluating brain tumor response to radiotherapy *NMR Biomed.* 26 443–50
- [60]. Foroutan P, Krehling J M, Morse D L, Grove O, Lloyd M C, Reed D, Raghavan M, Altiok S, Martinez G V and Gillies R J 2013 Diffusion MRI and novel texture analysis in osteosarcoma xenotransplants predicts response to anti-checkpoint therapy *PLoS One* 8 e82875
- [61]. Parmar C, Leijenaar R T H, Grossmann P, Rios Velazquez E, Bussink J, Rietveld D, Rietbergen M M, Haibe-Kains B, Lambin P and Aerts H J W L 2015b Radiomic feature clusters and prognostic signatures specific for lung and head & neck cancer *Sci. Rep.* 5 11044
- [62]. Dong X, Xing L, Wu P, Fu Z, Wan H, Li D, Yin Y, Sun X and Yu J 2013 Three-dimensional positron emission tomography image texture analysis of esophageal squamous cell carcinoma: relationship between tumor 18F- fluorodeoxyglucose uptake heterogeneity, maximum standardized uptake value, and tumor stage *Nucl. Med. Commun.* 34 40–6
- [63]. Mu W, Chen Z, Liang Y, Shen W, Yang F, Dai R, Wu N and Tian J 2015 Staging of cervical cancer based on tumor heterogeneity characterized by texture features on 18 F-FDG PET images *Phys. Med. Biol.* 60 5123
- [64]. Ganeshan B, Abaleke S, Young R C D, Chatwin C R and Miles K A 2010 Texture analysis of non-small cell lung cancer on unenhanced computed tomography: initial evidence for a relationship with tumour glucose metabolism and stage *Cancer Imaging* 10 137–43
- [65]. Belli ML, Scalco E, Sanguineti G, Fiorino C, Broggi S, Dinapoli N, et al. Early changes of parotid density and volume predict modifications at the end of therapy and intensity of acute xerostomia. *Strahlenther Onkol* 2014;190:1001–7.
- [66]. Incoronato, M.; Aiello, M.; Infante, T.; Cavaliere, C.; Grimaldi, A.M.; Mirabelli, P.; Monti, S.; Salvatore, M. Radiogenomic Analysis of Oncological Data: A Technical Survey. *Int. J. Mol. Sci.* 2017, 18, 805.
- [67]. Parekh, V., & Jacobs, M. A. (2016). Radiomics: a new application from established techniques. *Expert Review of Precision Medicine and Drug Development*, 1(2), 207–226. <http://doi.org/10.1080/23808993.2016.1164013>
- [68]. Zhang, B.; Chang, K.; Ramkissoon, S.; Tanguturi, S.; Bi, W.L.; Reardon, D.A.; Ligon, K.L.; Alexander, B.M.; Wen, P.Y.; Huang, R.Y. Multimodal MRI features predict isocitrate dehydrogenase genotype in high-grade gliomas. *Neuro. Oncol.* 2017, 19, 109–117.
- [69]. Zhu, Y.T.; Li, H.; Guo, W.T.; Drukker, K.; Lan, L.; Giger, M.L.; Ji, Y. Deciphering genomic underpinnings of quantitative MRI-based radiomic phenotypes of invasive breast carcinoma. *Sci. Rep.* 2015, 5.
- [70]. Friedman, J.H. On bias, variance, 0/1—Loss, and the curse-of-dimensionality. *Data Min. Know. Discov.* 1997, 1, 55–77.
- [71]. Balagurunathan, Y.; Kumar, V.; Gu, Y.H.; Kim, J.; Wang, H.; Liu, Y.; Goldgof, D.B.; Hall, L.O.; Korn, R.; Zhao, B.S.; et al. Test-retest reproducibility analysis of lung CT image features. *J. Digit. Imaging* 2014, 27, 805–823.
- [72]. Kuo, M.D.; Gollub, J.; Sirlin, C.B.; Ooi, C.; Chen, X. Radiogenomic analysis to identify imaging phenotypes associated with drug response gene expression programs in hepatocellular carcinoma. *J. Vasc. Interv. Radiol.* 2007, 18, 821–831.
- [73]. Wu, W.M.; Parmar, C.; Grossmann, P.; Quackenbush, J.; Lambin, P.; Bussink, J.; Mak, R.; Aerts, H. Exploratory study to identify radiomics classifiers for lung cancer histology. *Front. Oncol.* 2016, 6.
- [74]. Guo, W.T.; Li, H.; Zhu, Y.T.; Lan, L.; Yang, S.J.; Drukker, K.; Morris, E.; Burnside, E.; Whitman, G.; Giger, M.L.; et al. Prediction of clinical phenotypes in invasive breast carcinomas from the integration of radiomics and genomics data. *J. Med. Imaging* 2015, 2.
- [75]. Wu, T.T.; Chen, Y.F.; Hastie, T.; Sobel, E.; Lange, K. Genome-wide association analysis by lasso penalized logistic regression. *Bioinformatics* 2009, 25, 714–721.
- [76]. Jamshidi, N.; Jonasch, E.; Zapala, M.; Korn, R.L.; Aganovic, L.; Zhao, H.J.; Sitaram, R.T.; Tibshirani, R.J.;

- Banerjee, S.; Brooks, JD.; et al. The radiogenomic risk score: Construction of a prognostic quantitative, noninvasive image-based molecular assay for renal cell carcinoma. *Radiology* 2015, 277, 114–123.
- [77]. Leung, M.K.K.; Delong, A.; Alipanahi, B.; Frey, B.J., Machine learning in genomic medicine: A review of computational problems and data sets. *Proc. IEEE* 2016, 104, 176–197.
- [78]. Deng, L.; Yu, D. (2014), "Deep Learning: Methods and Applications", *Foundations and Trends® in Signal Processing*: Vol. 7: No. 3–4, pp 197-387. <http://dx.doi.org/10.1561/20000000039>
- [79]. Lee, Geewon et al., Radiomics and its emerging role in lung cancer research, imaging biomarkers and clinical management: State of the art, *European Journal of Radiology*, Volume 86, 297 - 307
- [80]. Gillies, Robert J.; Kinahan, Paul E.; Hricak, Hedvig (2015-11-18). "Radiomics: Images Are More than Pictures, They Are Data". *Radiology*. 278 (2): 563–577. doi:10.1148/radiol.2015151169.
- [81]. Weinreb JC, Barentsz JO, Choyke PL, Cornud F, Haider MA, Macura KJ, Margolis D, Schnall MD, Shtern F, Tempny CM, Thoeny HC, Verma S. Weinreb JC. PI-RADS Prostate Imaging-Reporting and Data System:2015,Version 2. *Eur Urol* 2016;69(1):16-40
- [82]. Bomers JG, Barentsz JO. Standardization of multiparametric prostate MR imaging using PI-RADS. *BioMed Res Int* 2014;2014: 431680.
- [83]. Burnside ES, Sickles EA, Bassett LW, et al. The ACR BI-RADS experience: learning from history. *J Am Coll Radiol* 2009;6(12): 851–860.
- [84]. Kazerooni EA, Armstrong MR, Amorosa JK, et al. ACR CT accreditation program and the lung cancer screening program designation. *J Am Coll Radiol* 2015;12(1):38–42.
- [85]. Davnall F, Yip CS, Ljungqvist G, et al. Assessment of tumor heterogeneity: an emerging imaging tool for clinical practice? *Insights Imaging* 2012; 3(6):573–589.
- [86]. O'Connor JP, Rose CJ, Waterton JC, Carano RA, Parker GJ, Jackson A. Imaging intratumor heterogeneity: role in therapy response, resistance, and clinical outcome. *Clin Cancer Res* 2015;21(2):249–257.
- [87]. Rose CJ, Mills SJ, O'Connor JP, et al. Quantifying spatial heterogeneity in dynamic contrast-enhanced MRI parameter maps. *Magn Reson Med* 2009;62(2):488–499.
- [88]. Larkin TJ, Canuto HC, Kettunen MI, et al. Analysis of image heterogeneity using 2D Minkowski functionals detects tumor responses to treatment. *Magn Reson Med* 2014; 71(1):402–410.
- [89]. Pickup L, Talwar A, Stalin S, et al. Lung nodule classification using learnt texture features on a single patient population [abstr]. In: *Radiological Society of North America Scientific Assembly and Annual Meeting Program*. Oak Brook, Ill: Radiological Society of North America, 2015; SSM06.
- [90]. Schabath MB, Massion PP, Thompson ZJ, Eschrich SA, Balagurunathan Y, Goldof D, et al. (2016) Differences in Patient Outcomes of Prevalence, Interval, and Screen-Detected Lung Cancers in the CT Arm of the National Lung Screening Trial. *PLoS ONE* 11(8): e0159880. <https://doi.org/10.1371/journal.pone.0159880>
- [91]. Duc Fehr, Harini Veeraraghavan, Andreas Wibmer, Tatsuo Gondo, Kazuhiro Matsumoto, Herbert Alberto Vargas, Evis Sala, Hedvig Hricak, and Joseph O. Deasy, Automatic classification of prostate cancer Gleason scores from multiparametric magnetic resonance images *PNAS* 2015 112 (46) E6265-E6273; published ahead of print November 2, 2015, doi:10.1073/pnas.1505935112
- [92]. Vignati A, Mazzetti S, Giannini V, et al. Texture features on T2-weighted magnetic resonance imaging: new potential biomarkers for prostate cancer aggressiveness. *Phys Med Biol* 2015;60(7):2685–2701.
- [93]. Committee on the Review of Omics-Based Tests for Predicting Patient Outcomes in Clinical Trials, Board on Health Care Services, Board on Health Sciences Policy, Institute of Medicine. *Evolution of Translational Omics: Lessons Learned and the Path Forward*. Micheel CM, Nass SJ, Omenn GS, eds. Washington, DC: National Academies Press.
- [94]. Simon RM, Paik S, Hayes DF. Use of archived specimens in evaluation of prognostic and predictive biomarkers. *J Natl Cancer Inst* 2009;101(21):1446–1452.
- [95]. Hayes DF, Bast RC, Desch CE, et al. Tumor marker utility grading system: a framework to evaluate clinical utility of tumor markers. *J Natl Cancer Inst* 1996;88(20):1456–1466.
- [96]. Chalmers I, Glasziou P. Avoidable waste in the production and reporting of research evidence. *Lancet* 2009;374(9683):86–89.
- [97]. Simera I, Moher D, Hirst A, Hoey J, Schulz KF, Altman DG. Transparent and accurate reporting increases

- reliability, utility, and impact of your research: reporting guide- lines and the EQUATOR Network. *BMC Med* 2010;8:24.
- [98]. Prinz F, Schlange T, Asadullah K. Believe it or not: how much can we rely on published data on potential drug targets? *Nat Rev Drug Discov* 2011;10(9):712.
- [99]. Begley CG, Ellis LM. Drug development: Raise standards for preclinical cancer re- search. *Nature* 2012;483(7391):531–533.
- [100]. Journals unite for reproducibility. *Nature* 2014;515(7525):7.
- [101]. McNutt M. Journals unite for reproducibility. *Science* 2014;346(6210):679.
- [102]. Landis SC, Amara SG, Asadullah K, et al. A call for transparent reporting to optimize the predictive value of preclinical research. *Nature* 2012;490(7419):187–191.
- [103]. Drawing Causal Inference from Big Data. Arthur M. Sackler Colloquia of the National Academy of Sciences. <https://www.youtube.com/playlist?list=PLGjm1x3XQeK0NgFOX2Z7Wt-P5RU5Zv0Hv>. Published April 2, 2015. Accessed May 5, 2015.
- [104]. Nelson B. Data sharing: empty archives. *Nature* 2009;461(7261):160–163.
- [105]. Devidas M, London WB, Anderson JR. The use of central laboratories and remote electronic data capture to risk-adjust therapy for pediatric acute lymphoblastic leukemia and neuroblastoma. *Semin Oncol* 2010;37(1):53– 59.
- [106]. Heilbrun ME. Evaluating RadLex and real world radiology reporting: are we there yet? *Acad. Radiol.* 2013;20(11):1327–1328.
- [107]. Kahn CE Jr. Annotation of figures from the biomedical imaging literature: a comparative analysis of RadLex and other standardized vocabularies. *Acad. Radiol.* 2014;21(3):384– 392.
- [108]. Mabotuwana T, Lee MC, Cohen-Solal EV, Chang P. Mapping institution-specific study descriptions to RadLex Playbook entries. *J Digit Imaging* 2014;27(3):321–330.
- [109]. Clark K, Vendt B, Smith K, et al. The Cancer Imaging Archive (TCIA): maintaining and operating a public information repository. *J Digit Imaging* 2013;26(6):1045–1057.
- [110]. Sudarshan VK, Mookiah MR, Acharya UR, Chandran V, Molinari F, Fujita H, et al. Application of wavelet techniques for cancer diagnosis using ultrasound images: a review. *Comput Biol Med* 2016; 69: 97–111. doi: <https://doi.org/10.1016/j.compbimed.2015.12.006>
- [111]. Andrėkutė K, Linkeviciutė G, Raišutis R, Valiukevicienė S, Makštienė J. Automatic differential diagnosis of melanocytic skin tumors using ultrasound data. *Ultrasound Med Biol* 2016; 42: 2834–43. doi: <https://doi.org/10.1016/j.ultrasmedbio.2016.07.026>
- [112]. Wu MH, Chen CN, Chen KY, Ho MC, Tai HC, Wang YH, et al. Quantitative analysis of echogenicity for patients with thyroid nodules. *Sci Rep* 2016; 6: 35632. doi: <https://doi.org/10.1038/srep35632>
- [113]. Song G, Xue F, Zhang C. A model using texture features to differentiate the nature of thyroid nodules on sonography. *J Ultrasound Med* 2015; 34: 1753–60. doi: <https://doi.org/10.7863/ultra.15.14.10045>
- [114]. Moon WK, Huang YS, Lo CM, Huang CS, Bae MS, Kim WH, et al. Computer-aided diagnosis for distinguishing between triple-negative breast cancer and fibroadenomas based on ultrasound texture features. *Med Phys* 2015; 42: 3024–35. doi: <https://doi.org/10.1118/1.4921123>
- [115]. Ardakani AA, Gharbali A, Mohammadi A. Classification of breast tumors using sonographic texture analysis. *J Ultrasound Med* 2015; 34: 225–31. doi: <https://doi.org/10.7863/ultra.34.2.225>
- [116]. Nadeau MJ, Desrochers A, Lamontagne M, Lariviere C, Gagnon DH. Quantitative ultrasound imaging of Achilles tendon integrity in symptomatic and asymptomatic individuals: reliability and minimal detectable change. *J Foot Ankle Res* 2016; 9: 30. doi: <https://doi.org/10.1186/s13047-016-0164-3>
- [117]. I. Stoffels et al., Metastatic status of sentinel lymph nodes in melanoma determined noninvasively with multispectral optoacoustic imaging, *SCIENCE TRANSLATIONAL MEDICINE* 09 DEC 2015 : 317RA199
- [118]. I. Stoffels, S. Morscher, I. Helfrich, U. Hillen, J. Lehy, N. C. Burton, T. C. P. Sardella, J. Claussen, T. D. Poeppel, H. S. Bachmann, A. Roesch, K. Griewank, D. Schadendorf, M. Gunzer, J. Klode , Erratum for

the Research Article: “Metastatic status of sentinel lymph nodes in melanoma determined noninvasively with multispectral optoacoustic imaging”, *SCIENCE TRANSLATIONAL MEDICINE* 23 DEC 2015 : 319ER8

- [119]. Lacey R. McNally, Megan Mezera, Desiree E. Morgan, Peter J. Frederick, Eddy S. Yang, Isam-Eldin Eltoum and William E. Grizzle, Current and Emerging Clinical Applications of Multispectral Optoacoustic Tomography (MSOT) in Oncology, *Clin Cancer Res* May 20 2016 DOI: 10.1158/1078-0432.CCR-16-0573
- [120]. Leong, S. P. L., Kothapalli, S.-R., & Gambhir, S. S. (2016). Can multispectral optoacoustic tomography replace sentinel lymph biopsy in melanoma? *Annals of Translational Medicine*, 4(24), 517. <http://doi.org/10.21037/atm.2016.12.31>
- [121]. Diederik Grootendorst, PhD thesis, “Detection of lymph node metastases by photoacoustic imaging”, discussion on 17 April 2013. Thesis supervisors Prof. Theo Ruers and Prof. Wiendelt Steenbergen. Assistant supervisor is Dr Srirang Manohar, University of Twente.
- [122]. Alejandro Garcie-Urde et al., Dual-Modality Photoacoustic and Ultrasound Imaging System for Non invasive Sentinel Lymph Node Detection in Patients with Breast Cancer, *Scientific Reports* 5, Article number: 15748 (2015), doi:10.1038/srep15748
- [123]. Garra BS, Krasner BH, Horii SC, Ascher S, Mun SK, Zeman RK. Improving the distinction between benign and malignant breast lesions: the value of sonographic texture analysis. *Ultrasonic Imaging*. 1993; 15(4):267–285.
- [124]. Sivaramakrishna R, Powell KA, Lieber ML, Chilcote WA, Shekhar R. Texture analysis of lesions in breast ultrasound images. *Computerized medical imaging and graphics*. 2002; 26(5):303–307.
- [125]. Singh BK, Verma K, Thoke A. Adaptive Gradient Descent Backpropagation for Classification of Breast Tumors in Ultrasound Imaging. *Procedia Computer Science*. 2015; 46:1601–1609.
- [126]. Chen D-R, Chang R-F, Kuo W-J, Chen M-C, Huang Y-L. Diagnosis of breast tumors with sonographic texture analysis using wavelet transform and neural networks. *Ultrasound in medicine & biology*. 2002; 28(10):1301–1310.
- [127]. Chen D-R, Chang R-F, Huang Y-L, Chou Y-H, Tiu C-M, Tsai P-P. Texture analysis of breast tumors on sonograms. *Seminars in Ultrasound, CT and MRI*. 2000; 21(4):308–316.
- [128]. C Bartolozzi, C Selli, M Olmastroni, I Menchi, and G Di Candio, Rhabdomyosarcoma of the prostate: MR findings, *American Journal of Roentgenology* 1988 150:6, 1333-1334
- [129]. Esposito, M. et al., PD-0145: Diffusional kurtosis as a biomarker of prostate cancer response to radiation therapy, *Radiotherapy and Oncology* , Volume 115 , S69 - S70
- [130]. Menchi I., Resi F., Innocenti P., Carpi R., (2006) Prostata. In: *Radiologia geriatrica*. Springer, Milano, DOI: https://doi.org/10.1007/88-470-0486-1_47, Springer, Milano, Print ISBN978-88-470-0485-6, Online ISBN978-88-470-0486-3
- [131]. <https://www.rsna.org/QIBA/>, web site checked at August 2017
- [132]. Oakden-Rayner L, Carneiro G, Bessen T, Nascimento JC, Bradley AP, Palmer LJ. Precision Radiology: Predicting longevity using feature engineering and deep learning methods in a radiomics framework. *Scientific Reports*. 2017;7:1648. doi:10.1038/s41598-017-01931-w.
- [133]. Drukker, K. (2016), TU-B-207B-00: Challenges in Radiomics and Big Data. *Med. Phys.*, 43: 3742. doi:10.1118/1.4957461
- [134]. Daniel Richard Leff, Guang-Zhong Yang. Big Data for Precision Medicine[J]. *Engineering*, 2015, 1(3): 277 -279 .
- [135]. The power of big data must be harnessed for medical progress, *Nature*. 2016, Nov. 24; 539(7630):467-468. doi: 10.1038/539467b.
- [136]. Hripcsak G, Duke JD, Shah NH, et al. Observational Health Data Sciences and Informatics (OHDSI): Opportunities for Observational Researchers. *Studies in health technology and informatics*. 2015;216:574-578.
- [137]. Gaudreau et al. The Present and Future of Biomarkers in Prostate Cancer: Proteomics, Genomics, and immunology advancements. *Biomarkers in Cancer* 2016;8(s2) 15–33 doi:10.4137/BiC.s31802.

- [138]. Rahmim A, Salimpour Y, Jain S, et al. Application of texture analysis to DAT SPECT imaging: Relationship to clinical assessments. *NeuroImage : Clinical*. 2016;12:e1-e9. doi:10.1016/j.nicl.2016.02.012.
- [139]. Peng Huang, Nikolay Shenkov, Sima Fotouhi, Esmaeil Davoodi-Bojd, Lijun Lu, Zoltan Mari, Hamid Soltanian-Zadeh, Vesna Sossi, and Arman Rahmim, *Neurosciences Track - New Approaches to Image Parkinson Syndrome: Radiomics Analysis of Longitudinal DaTscan Images for Improved Progression Tracking in Parkinson's Disease*, *J Nucl Med* 2017 58:412
- [140]. Ahmad Chaddad, Christian Desrosiers & Matthew Toews, Multi-scale radiomic analysis of sub-cortical regions in MRI related to autism, gender and age, *Scientific Reports* 7, Article number: 45639 (2017), doi:10.1038/srep45639
- [141]. Van den Burg EL, van Hoof M, Postma AA, et al. An Exploratory Study to Detect Ménière's Disease in Conventional MRI Scans Using Radiomics. *Frontiers in Neurology*. 2016;7:190. doi:10.3389/fneur.2016.00190.
- [142]. Zhang, J., Yu, C., Jiang, G., Liu, W. & Tong, L. 3D texture analysis on MRI images of Alzheimer's disease. *Brain Imaging Behav.* 6, 61–69 (2011).
- [143]. Maani, R., Yang, Y. H. & Kalra, S. Voxel-Based Texture Analysis of the Brain. *PLoS ONE* 10 (2015).
- [144]. Chaddad, A., Desrosiers, C. & Toews, M. Local discriminative characterization of MRI for Alzheimer's disease. In 1–5, doi: 10.1109/ISBI.2016.7493197 (IEEE, 2016).
- [145]. Teipel, Stefan et al., Multimodal imaging in Alzheimer's disease: validity and usefulness for early detection, *The Lancet Neurology* , Volume 14 , Issue 10 , 1037 - 1053
- [146]. P. Prasanna, P.Tiwari, A.Madabhushi, Co-occurrence of Local Anisotropic Gradient Orientations (CoLIAGe): A new radiomics descriptor, *Nature Scientific Reports*, 2016, 6:37241 | DOI: 10.1038/srep37241
- [147]. Wang, Jing et al. "Machine learning-based analysis of MR radiomics can help to improve the diagnostic performance of PI-RADS v2 in clinically relevant prostate cancer." *European Radiology* (2017): 1-9.
- [148]. Patrick Grossmann, Olya Stringfield, Nehme El-Hachem, Marilyn M Bui, Emmanuel Rios Velazquez, Chintan Parmar, Ralph TH Leijenaar, Benjamin Haibe-Kains, Philippe Lambin, Robert Gillies, Hugo JWL Aerts. Defining the biological basis of radiomic phenotypes in lung cancer. *eLife*, 2017; 6 DOI: 10.7554/eLife.23421
- [149]. Ziad Obermeyer, and Ezekiel J. Emanuel, M.D., Predicting the Future — Big Data, Machine Learning, and Clinical Medicine, *N Engl J Med* 2016; 375:1216-1219 September 29, 2016 DOI: 10.1056/NEJMp1606181
- [150]. Mullainathan S, Spiess J. Machine learning: an applied econometric approach. *J Econ Perspect* (in press).
- [151]. Halevy A, Norvig P, Pereira F. The unreasonable effectiveness of data. *IEEE Intell Syst* 2009; 24(2): 8-12.
- [152]. Kleinberg J, Ludwig J, Mullainathan S, Obermeyer Z. Prediction policy problems. *Am Econ Rev* 2015; 105: 491-5.
- [153]. Bouton CE, Shaikhouni A, Annetta NV, et al. Restoring cortical control of functional movement in a human with quadriplegia. *Nature* 2016; 533: 247-50.
- [154]. Gilbert FJ, Astley SM, Gillan MGC, et al. Single reading with computer-aided detection for screening mammography. *N Engl J Med* 2008; 359: 1675-84.
- [155]. *Imaging Biomarkers. Development and Clinical Integration*, Editors: Luis Martí-Bonmatí, Angel Alberich-Bayarri, ISBN: 978-3-319-43502-2 (Print), 978-3-319-43504-6 (Online), 2017, DOI 10.1007/978-3-319-43504-6, Publisher: Springer International Publishing
- [156]. Zhang, Jing et al., Texture analysis of multiple sclerosis: a comparative study, *Magnetic Resonance Imaging* , Volume 26 , Issue 8 , 1160 - 1166
- [157]. Jack CR, Barnes J, Bernstein MA, et al. Magnetic Resonance Imaging in ADNI. *Alzheimer's &*

dementia : the journal of the Alzheimer's Association. 2015;11(7):740-756.
doi:10.1016/j.jalz.2015.05.002.

- [158]. Michoux N, Guillet A, Rommel D, Mazzamuto G, Sindic C, Duprez T (2015) Texture Analysis of T2-Weighted MR Images to Assess Acute Inflammation in Brain MS Lesions. PLoS ONE 10 (12): e0145497. doi:10.1371/journal.pone.0145497
- [159]. Sikiö, M. (2016). Textural Features in Medical Magnetic Resonance Image Analysis of the Brain and Thigh Muscles. (Tampere University of Technology. Publication; Vol. 1418). Tampere University of Technology.
- [160]. Sikiö, M. et al.,MR image texture in Parkinson's disease: a longitudinal study, Acta Radiologica 2015, Vol. 56 (1) 97 –104, DOI: 10.1177/0284185113519775 .
- [161]. Andrew J. Saykin, Li Shen, Xiaohui Yao, Sungeun Kim, Kwangsik Nho, Shannon L. Risacher, Vijay K. Ramanan, Tatiana M. Foroud, Kelley M. Faber, Nadeem Sarwar, Leanne M. Munsie, Xiaolan Hu, Holly D. Soares, Steven G. Potkin, Paul M. Thompson, John S.K. Kauwe, Rima Kaddurah-Daouk, Robert C. Green, Arthur W. Toga, Michael W. Weiner, Genetic studies of quantitative MCI and AD phenotypes in ADNI: Progress, opportunities, and plans, Alzheimer's & Dementia, Volume 11, Issue 7, 2015, Pages 792-814, ISSN 1552-5260, <http://dx.doi.org/10.1016/j.jalz.2015.05.009>.
- [162]. Andrew J. Saykin, Li Shen, Tatiana M. Foroud, Steven G. Potkin, Shanker Swaminathan, Sungeun Kim, Shannon L. Risacher, Kwangsik Nho, Matthew J. Huentelman, David W. Craig, Paul M. Thompson, Jason L. Stein, Jason H. Moore, Lindsay A. Farrer, Robert C. Green, Lars Bertram, Clifford R. Jack, Michael W. Weiner, Alzheimer's Disease Neuroimaging Initiative biomarkers as quantitative phenotypes: Genetics core aims, progress, and plans, Alzheimer's & Dementia, Volume 6, Issue 3, 2010, Pages 265-273, ISSN 1552-5260, <http://dx.doi.org/10.1016/j.jalz.2010.03.013>.